The Dissertation Committee for Amanda Kristin Vaughn Certifies that this is the approved version of the following Dissertation:

Mitochondrial Formate Production and its Impact on Embryonic Cranial Tissue Development in the Mouse

Committee:

Dean Appling, Supervisor

Karen Browning

Livia Schiavinato Eberlin

Richard Finnell

Steven Gross

Mitochondrial Formate Production and its Impact on Embryonic Cranial Tissue Development in the Mouse

by

Amanda Kristin Vaughn

Dissertation

Presented to the Faculty of the Graduate School of

The University of Texas at Austin

in Partial Fulfillment

of the Requirements

for the Degree of

Doctor of Philosophy

The University of Texas at Austin

August 2019

Dedication

This work is affectionately dedicated to my partner Travis, for being unconditionally supportive of me during my time spent working on my Ph.D., regardless of my mood (which wasn't always pleasant, to say the least). I also want to dedicate the seven years I've spent in graduate school to my parents Susan and Rick, and sister Elissa, for always believing in me and encouraging me to pursue my dreams of becoming both a doctor and an artist, which hasn't changed since I was first forming sentences. Lastly, although they will never read this dissertation, my two cats Charlie Chaplin and Nori deserve a special dedication, for keeping my spirits high throughout the stresses of graduate school.

Epigraph

"Still, what I want in my life
is to be willing
to be dazzled—
to cast aside the weight of facts

and maybe even
to float a little
above this difficult world.
I want to believe I am looking

into the white fire of a great mystery.
I want to believe that the imperfections are nothing—
that the light is everything—that it is more than the sum
of each flawed blossom rising and falling. And I do."
— Mary Oliver, *House of Light*

"The beginning of knowledge is the discovery of something we do not understand."

--Frank Herbert

Prologue

Development is both spatially and temporally a sensitive process. Nature has orchestrated growth in a very sophisticated manner, wherein the location of cells determines their fate. One response gives rise to another response, and it all must occur in the correct order at the correct time for development to occur properly. Behind all of these elaborate cell signaling processes lie individual cells, and within each exist thriving metabolic pathways that provide each cell with exactly what it needs to adapt and respond to cellular signals from its neighbors.

The story of any developmental process should be told from the beginning, wherein two cells become one. The haploid egg and haploid sperm come together to form a fully functional diploid zygote, which divides repeatedly until it forms the blastocyst, which encompasses 256 identical cells. It is at this crucial point that cells run out of the resources to continue dividing as they have previously, and they begin to differentiate into three different cell types: endoderm, mesoderm, and ectoderm populations. These three layers begin to expand laterally until they form what is known as the neural plate, which hinges and grows until it fuses into a closed neural tube. This process is what my research focuses on, as this folding and fusion process is invariably important; it is the neural tube that eventually becomes the brain and spinal cord—both of which an organism uses to continue to grow and develop throughout its entire lifetime.

Acknowledgements

I have been surrounded by extremely intelligent and inspiring scientists throughout my graduate career, for which I am eternally grateful. I would like to pay special homage to my mentor, Dr. Dean Appling, for his relentless support during my work in his lab, his patient guidance and advice, and for truly teaching me to think like a scientist. I would be remiss to not graciously thank my committee members: Dr. Karen Browning, for sticking with me throughout all my various meetings and presentations since my first months at the university; Dr. Livia Eberlin, for collaborating on my project and teaching me all about the wonders of mass spectrometry; Dr. Richard Finnell, for being a wise and perceptive mentor, as well as a friend and role model; and Dr. Steven Gross, for continuing to advise me from afar, both at home and abroad. I am also very thankful for the help from Appling lab members of past and present, in particular Dr. Jessica Momb, Dr. Minhye Shin, and Dr. Josh Bryant—it has been an honor to be a part of the folic acid research team with you three. I also would like to extend special appreciation towards Rachel Dehoog for being an excellent collaborative partner for all work done in Chapter 3, as well as Dr. William Shawlot for advising my mouse work and assisting me with the experiments in Chapter 4.3.6. Finally, I would like to thank Caleb Swain and the rest of the Huibregste lab for generously sharing their space and resources for work done in Chapter 4.3.2.

Mitochondrial Formate Production and its Impact on Embryonic Cranial Tissue Development in the Mouse

Amanda Kristin Vaughn, Ph.D.

The University of Texas at Austin, 2019

Supervisor: Dean Appling

Mammalian folate-dependent one-carbon (1C) metabolism provides the building blocks essential during development via amino acid interconversion, universal methyl-donor production, regeneration of redox factors, and *de novo* purine and thymidylate synthesis. Folate supplementation prevents most neural tube defects (NTDs) that occur during the embryonic process of neurulation. The mechanism of how folate functions during neurulation is not well understood, and not all NTDs are preventable by folate supplementation. Mthfd1l is a mitochondrial 1C metabolism enzyme that produces formate, a 1C donor that fuels biosynthesis and the methyl cycle in the cytoplasm. *Mthfdll*-null (*Mthfd1l*$^{-/-}$) mice are embryonic lethal and develop folate-resistant NTDs. These mice also have defects in cranial mesenchyme formation. In this work, the nature of how their mesenchyme is defective is explored. The extracellular matrix (ECM) of *Mthfd1l*$^{-/-}$ embryos was found to be depleted in glycosaminoglycan (GAG) composition, as well as the basement membrane protein Collagen IV. Imaging mass spectrometry (IMS) was used to construct ion maps of the cranial mesenchyme that identified the spatial distribution and abundance of metabolites in *Mthfd1l*$^{-/-}$ embryos compared to wild-type (WT). Purine and thymidylate derivatives, as well as amino acids, were

diminished in the cranial mesenchyme of *Mthfd1l*$^{-/-}$ embryos. Loss of Mthfd1l activity in this region also led to abnormal levels of methionine and dysregulated energy metabolism. These alterations in metabolism suggest possible approaches to preventing NTDs in humans. Finally, we created a mouse lacking both Mthfd1l and Aldh1l2, which is another mitochondrial enzyme associated with formate production. These embryos exhibit a more dramatic birth defect phenotype than *Mthfd1l*$^{-/-}$ embryos. By associating metabolite abundance, gene expression, and tissue development, this study is focused on enhancing our current understanding of how folate-dependent 1C metabolism functions during neurulation.

Table of Contents

List of Tables

List of Figures

CHAPTER 1: INTRODUCTION

1.1 MAMMALIAN NEURAL TUBE CLOSURE

1.1.1 Neurulation

The developing mammalian embryo rapidly undergoes changes while it grows to become an autonomous organism. During the most crucial step of embryogenesis, ectoderm cells have expanded to form a wide neural plate, and must now bend and fuse to create a closed neural tube. This process is called neurulation, and it forms the basis of what ultimately becomes the central nervous system (CNS) of the developing embryo. This morphogenetic process is highly demanding of cellular resources, making biosynthesis a key requirement of neurulation. In turn, the metabolic processes that underlie these dynamic, early steps of development are crucial in driving embryogenesis, and will be reviewed in depth in the Chapter 1.2.

Neurulation begins during gastrulation, the process when dorsal midline ectoderm is induced to become neuroepilthelium, forming the neural plate (Copp, 2005) (refer to Figure 1). First, this layer of specialized ectoderm bends acutely at the midline, forming the median hinge point (MHP) immediately above the notochord, which creates the cross-sectional V-shaped 'neural groove' between two neural folds (McShane et al., 2015). Simultaneously, the neural plate continues to elongate rostrocaudually by rapid cell division and convergent extension. During a second phase, the neural folds each bend at paired dorsolateral hingepoints (DLHPs) to form longitudinal furrows, resulting in a neural plate with a diamond shaped lumen. At this point, the tips of the neural plate are turned inward, and they continue to draw towards the dorsal midline as the entire epithelium exhibits bending, which reduces the existence of specific hinge points and

forms a fused neural tube with a circular-shaped lumen. In experimental explants in cell culture, it was observed that the final stage of neural tube closure is dependent primarily on forces generated intrinsic to the neuroepithelium, unlike earlier stages in neural tube closure that are driven by forces extrinsic to the neuroepithelium (van Straaten et al., 1993). Most substantial of the intrinsic forces that ultimately close the neural tube is cell proliferation, and areas of differing cell density result on either side of the DLHPs—a cell density difference that is proposed to cause the bending and fusion of the neural folds (Juriloff and Harris, 2018). Additional intrinsic mechanisms that are active during the process of neurulation, such as neural crest cell migration, will be explored in Chapter 2.

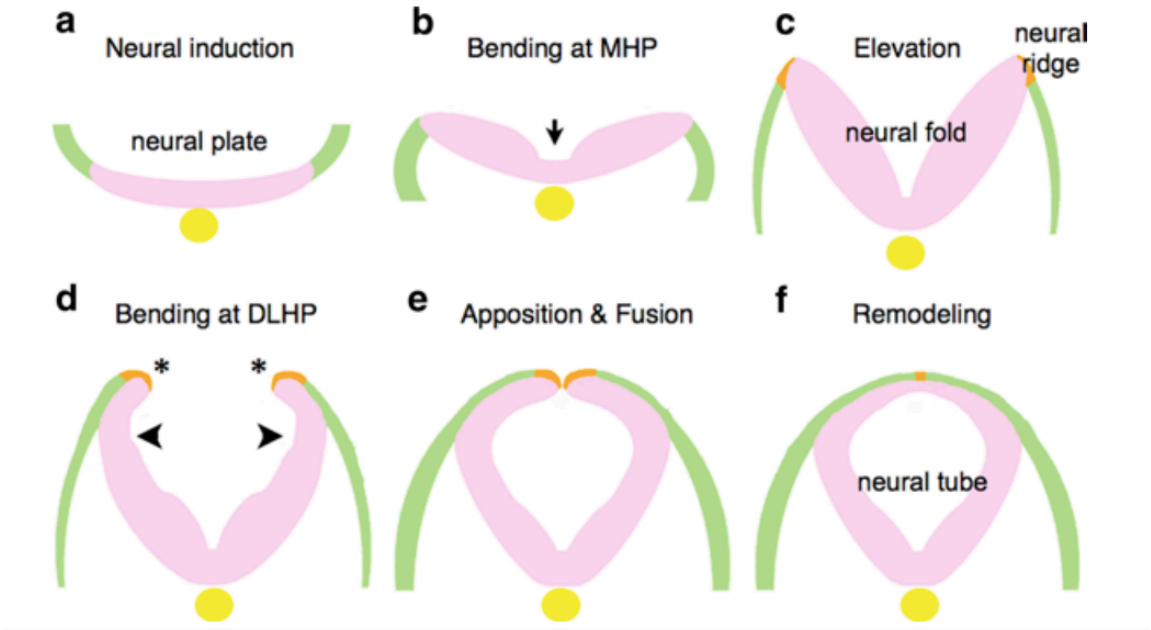

Figure 1.1: **Morphological changes of neural plates to form the neural tube**. "After neural induction (a), the neural plate bends at MHP (b) and is elevated to form the neural fold (c). Subsequently, flipping of the edges (asterisks) and bending at DLHP occur (d), resulting in apposition and fusion of the edges (e). Remodeling takes place to separate neuroectoderm and surface ectoderm (f). Neuroectoderm (neuroepithelum): pink. Non-neural ectoderm (surface ectoderm): green. Boundary region within non-neural ectoderm: orange. Notochord: yellow." (Yamaguchi and Miura, 2013)

1.1.2 Neural Tube Defects

The tightly regulated process of neurulation is complete by embryonic (or post-conception) day 28 in the human, and day 10 in the mouse. This means that by the time most women discover they are pregnant, the neural tube has already closed—or not, in some cases. To allow the neural tube to close completely, a number of genes must cooperate in order for the following developmental mechanisms to take place: programmed cell death, neural crest cell migration, proliferation of neuroepithelium, contraction of apical cytoskeletal microfilaments, and flexing at DLHPs (Blom et al., 2006). If these morphogenetic processes do not occur at precisely the correct moment, the neural tube does not close completely and the embryo will have a neural tube defect (NTD). Although closure of the neural tube is not required for subsequent specialized differentiation of neurons nor the formation of neuronal networks, it is essential for brain development (Copp, 2005). Many NTDs are lethal, including anencephaly, or failure of NTC in the cranial region, and craniorachischisis, or failure of NTC along the entire body axis. More common is failure to close at the caudal region of the neural tube, referred to as spina bifida or meningomyelocele; this NTD is associated with defects in the neural arches and is compatible with post-natal survival, although surgery is generally necessary and still results in significant neurological impairment (Wallingford et al., 2013). Exposure to the amniotic fluid is toxic for cells usually contained within the closed neural tube, and leads to neurodegeneration of the exposed regions in utero (Copp et al., 2013).

The prevalence of NTDs differs across time and geography, but recent analysis concludes that they range from 3.3 to 27.9 per 10,000 births in the Americas alone, with increased instances in poorer countries with malnutrition and lack of preventative healthcare (Zaganjor et al., 2016). The lifetime medical expenses of a patient with spina bifida are high and place an even greater burden on individuals already dealing with

physical and mental handicaps—the total cost of children born with spina bifida is over US$81 million annually in California (Blom et al., 2006).

The complexity of the etiology of NTDs is further complicated by the influence of both environmental and genetic risk factors. Environmentally, maternal nutrition has been shown to play a significant role in NTD epidemiology; of particular importance is a diet rich in folate, a link that has been established since the 1960s (Hibbard and Smithells, 1965).

1.1.3 Folate Supplementation

1.1.3.1 Folate and NTDs

Between the years 1961 and 1963 at the Mill Road Maternity Hospital in Liverpool, Dr. Elizabeth Hibbard, MD assessed the folate levels of bone marrow, serum, and tissue of 1,484 patients, and found that folate-deficient mothers were more likely to have spontaneous abortions or fetal malformations (Hibbard, 1964). He concluded his report advising mothers to seek early prophylactic supplementation with folate in order to avoid birth complications. These findings were further explored the following year by Dr. Richard Smithells, wherein it was documented that a familial occurrence of birth defects suggested they were due to a "genetically determined defect of folate metabolism" (Hibbard and Smithells, 1965). It was not until 1991 that a randomized double-blind study was conducted at 33 different birthing centers in seven different countries, testing the efficacy of folate versus a cocktail of seven other vitamins (A, D, B_1, B_2, B_6, C, and nicotinamide) in preventing birth defects (MRC Vitamin Study Research Group, 1991). This study revealed that a daily dose of 4mg folate was able to prevent up to 72% of NTDs in high risk mothers, whereas the other vitamins showed no such protective effect. Similar results were produced by experiments that examined the effects of a lower dose

of 400 μg folic acid on a larger study population in China between 1993 and 1995, at which point NTDs were occurring at a high rate of 6 per 1000 births (Berry et al., 1999).

1.1.3.2 Mandatory Fortification

The success of folate supplementation in preventing NTDs compelled the CDC to recommend that all women of childbearing age consume 400μg/day of folic acid (Centers for Disease Control and Prevention, 1992). However, by 1998, it was found that only 29% of women consumed the recommended amount of folic acid; that same year, the United States made it compulsory to fortify all flour and enriched grain products with 140μg folic acid/100 g (Centers for Disease Control and Prevention, 1999). Fortification was deemed more effective than vitamin supplementation at increasing the folate levels of both serum and red blood cells of women of childbearing age. The rate of NTDs decreased significantly in the years following fortification; depending on the region, the instance of NTDs was lowered by 31 to 78 % (Eichholzer et al., 2006). Fortification is currently mandatory in 70 countries, including the US, Canada, and Australia, yet it has still not been introduced in the European Union, despite evidence that it is effective at preventing NTDs (Bestwick et al., 2014). The fact that folic acid supplementation has not been successful at preventing 100% of NTDs indicates that some are folate-resistant. An assessment of the instance of NTDs among pregnancies conceived following mandatory fortification showed that there was no significant association of folic acid supplementation and NTDs (Mosley et al., 2009). These findings suggest that mandatory fortification may have ameliorated the instance of folate-sensitive NTDs. The mechanism of how folate is related to birth defects is not well-understood, and motivates further efforts to understand the folate-dependent one-carbon pathway.

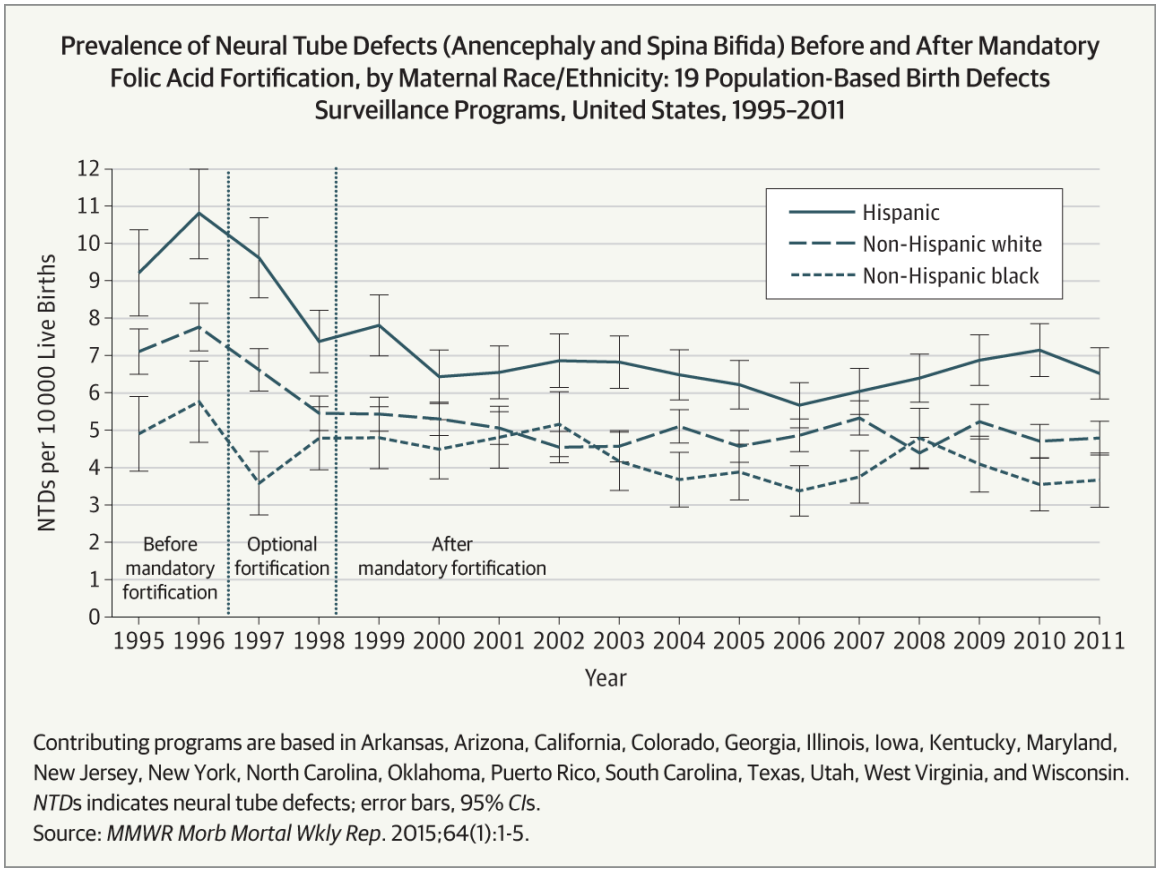

Figure 1.2: **The effectiveness of folate supplementation in the US** (Williams et al., 2015).

1.2 FOLATE-DEPENDENT ONE-CARBON METABOLISM

1.2.1 Folate in Mammalian cells

From four tons of spinach, Esmond Snell and his colleagues first isolated folic acid in 1941 in Welch Hall at the University of Texas at Austin (Mitchell et al., 1941). The name "folic acid" was derived from the Latin term for leaves—*folium*. This vitamin was shown to serve as a growth factor for *Streptococcus lactis*, *Lactobacillus casei*, and *Lactobacillus delbrückii*, and a number of sources from animal liver to mushrooms were shown to be rich sources of this material. The report also concluded that commercially canned greens were "nearly lacking in the substance."

Folic acid and its reduced derivatives form the collective group of coenzymes known as folates, which can carry one-carbon (1C) units at different oxidation states. Folates contain a pteridine ring that is covalently linked at carbon 6 to a para-aminobenzoic acid (PABA) with a poly-γ-glutamate tail (Figure 1.2). Activated carbon species are carried on N5 of the pteridine ring, or at N10, or both. In mammalian cells, tetrahydrofolate (THF) is biologically active form of folate. Dietary folic acid enters the cell via folate receptors (Folr), the reduced folate carrier (RFC), and the proton-coupled folate transporter (PCFT) (Radziejewska and Chmurzynska, 2019), and then it is reduced twice by the enzyme dihydrofolate reductase (DHFR) to THF, at which point it can begin to transfer 1C units. THF acts as a coenzyme in a wide range of different cellular reactions, as it gives cells the ability to readily interconvert 1C units between different oxidation states. The 1C-transfers mediated by THF are essential for a number of cellular processes: vitamin metabolism, nucleic acid biosynthesis, amino acid metabolism, methyl group biogenesis, and mitochondrial protein biosynthesis (Tibbetts and Appling, 2010).

In cellular forms of folate, the PABA moiety is modified by a poly-γ-glutamic tail (Figure 1.2) in a reaction catalyzed by folylpolyglutamate synthetase (FPGS), and the length of this chain varies from one cell type to another; however, most common in eukaryotic cells are the penta- and hexaglutamate forms (Fox and Stover, 2008; Tibbetts and Appling, 2010). This modification serves to retain folate within a cell, and also makes it a more efficient substrate when interacting with folate-dependent enzymes (McBurney and Whitmore, 1974; Shane, 1989; Strong and Schirch, 1989). The interaction of folate cofactors and folate-binding enzymes is further promoted by an excess concentration of enzymes compared to their cofactor targets, which keeps cellular folate localized to specific regions within the cell (Kim et al., 1996).

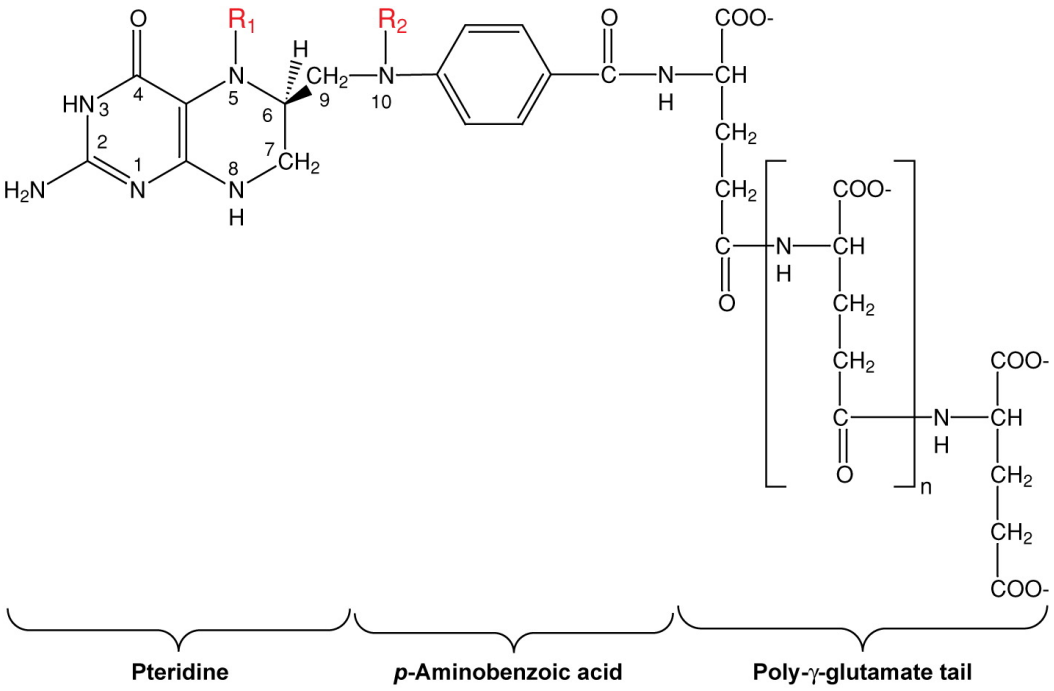

Tibbetts AS, Appling DR. 2010.
Annu. Rev. Nutr. 30:57–81

Figure 1.3: **The structure of tetrahydrofolate (THF), a water soluble B vitamin with three distinct moieties**: a fully reduced pterin ring, a para-aminobenzoyl group, and a poly-γ-glutamate tail. Activated 1C-units are carried on N5 and N10 (R_1 and R_2, respectively) yield 5-methyl-, 5-formyl-, 5,10-methylene-, 5,10-methenyl, and 10-formyl-THF derivatives. (Tibbetts and Appling, 2010)

1.2.2 Compartmentalization of Folate-mediated One-carbon Metabolism

1.2.2.1 Overview of One-carbon Metabolism

Tracing of [^{3}H]-folic acid in rat liver demonstrated that folic acid is present throughout the cell; it is found in the cytoplasm, mitochondria, nucleus, lysosome, and microsomes (Yoon Soon Shin et al., 1976). It is most abundant in the cytosol and mitochondria (Lin et al., 1993), which are active sites of biosynthesis generated by the folate-mediated one-carbon metabolism. Once DHFR converts folate from the diet first into 7,8-dihydrofolate and then 5,6,7,8-tetrahydrofolate (herein referred to as THF), folate is biologically active and can participate in 1C-transfer reactions. In most organisms, the primary source of 1C units transferred to THF is carbon 3 of serine, in a reaction catalyzed by serine hydroxymethyltransferase (SHMT), which generates glycine and 5,10-methyl tetrahydrofolate (Fox and Stover, 2008; Tibbetts and Appling, 2010). Pools of THF are generally maintained in cellular compartments, most significantly the mitochondria, cytoplasm, and nucleus, wherein the extent of polyglutamylation varies by compartment with mostly heptaglutamates residing in the mitochondria and hexaglutamates predominating in the cytosol (Lin et al., 1993). These compartments remain connected by the transfer of the 1C-donors formate, serine, glycine, and less commonly sarcosine and dimethylglycine (Barlowe and Appling, 1988). The flux of 1C-units across mitochondrial membranes assumes a mostly unidirectional flow in the clockwise direction (Figure 1.4) under most conditions. The main thrust of the pathway from the cytoplasm into the mitochondria and back into the cytoplasm is catalyzed by enzymes of the methylene-tetrahydrofolate (MTHFD) gene family. Mitochondrial enzymes MTHFD2, MTHFD2L, and MTHFD1L work together to fully oxidize the 1C

unit bound to THF, whereas the cytoplasmic MTHFD1 catalyzes the three same reactions in the reductive direction.

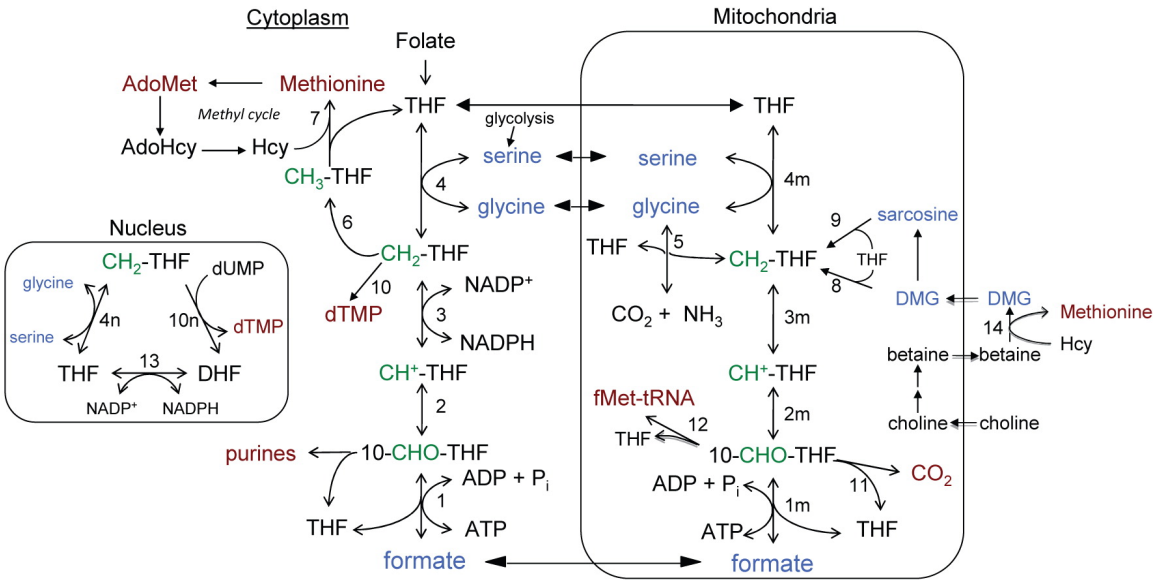

Tibbetts AS, Appling DR. 2010.
Annu. Rev. Nutr. 30:57–81

Figure 1.4: **Compartmentalization of 1C-metabolism in mammalian cells between the mitochondria, cytoplasm, and the nucleus.** Reactions of the pathway are catalyzed by the following enzymes: SHMT2 (4m), MTHFD2/2L (3m and 4m), MTHFD1L (1m), MTHFD1 (1, 2, and 3), SHMT1 (4, 4n), GCS (5), MTHFR (6), MTR (7), DMGDH (8), SDH (9), thymidylate synthase (10, 10n, and 10m), 10-CHO-THF dehydrogenase (ALDH1L2) (11), methionyl-tRNA formyltransferase (12), dihydrofolate (DHF) reductase (13), betaine-homocysteine methyltransferase (14) (Tibbetts and Appling, 2010).

1.2.2.2 Mitochondrial One-carbon Metabolism

Approximately 40% of intercellular folate is found in the mitochondria (Yoon Soon Shin et al., 1976), and although it is not in a state of equilibrium with THF pools in the cytoplasm or nucleus (Lin et al., 1993), it is able to cross the mitochondrial membrane via SLC25A32, a transporter critical for survival in mice (Kim et al., 2018). Early tracing experiments using radiolabeled folic acid in rat liver demonstrated that THF rapidly accumulates in the mitochondria (Cook and Blair, 1979; Zamierowski and Wagner, 1977), a finding that was corroborated much later when SLC25A32 was established as the mitochondrial folate carrier (Titus and Moran, 2000). Within the mitochondria of rat hepatocytes, the predominant forms of folate are THF and 10-formyl-THF. Among the remaining folate species, 11% is in the form of 5-formyl-THF, and less then 7% assumes the form of 5-methyl-THF (Horne et al., 1989).

The net reaction of mitochondrial folate-metabolism is the oxidation of the 3-carbon of serine or the N-methyl carbon of sarcosine to formate and CO_2. Isolated mitochondria from adult rat liver readily produce formate and CO_2 without any additional cofactors, indicating that all enzymes and cofactors required are present within the mitochondria (Barlowe and Appling, 1988). Serine crosses the mitochondrial membrane via SFXN1, which was shown to be essential for purine and glycine synthesis in cells (Kory et al., 2018). Serine then transfers its third carbon onto THF, generating glycine and 5,10-methylene-THF (CH_2-THF), in a reaction catalyzed by SHMT2 (Figure 1.4, reaction 4m). SHMT2 is expressed in ubiquitously in adult and embryonic tissues, and knockdown of SHMT2 causes 1C-units to flow in the reverse, counterclockwise direction in cell lines (Motokawa and Kikuchi, 1971; Ducker et al., 2016). SHMT2 is upregulated in cancer cells, which has driven the hypothesis that glycine is in high demand in rapidly proliferating cell populations (Jain et al., 2012; Lee et al., 2014). Glycine is also an

important 1C donor to THF via the glycine cleavage system (GCS, Figure 1.4, reaction 5), which releases the final carbon in the form of CO_2. The GCS is composed of glycine decarboxylase (GLDC), aminomethyltransferase (AMT), the hydrogen transferring GCS-H protein, and the P-subunit, which catalyzes the PLP-dependent decarboxylation of glycine. Deletion of GLDC or AMT in mice causes NTDs, presumably due to a limited supply of 1C-units from mitochondrial folate metabolism (Pai et al., 2015).

At this point in the pathway, two additional 1C donors may enter the mitochondria: sarcosine and dimethylglycine (DMG), both of which are intermediates in choline oxidation. Choline is a major dietary source of methyl groups by synthesis of S-adenosylmethionine (AdoMet) (Stead et al., 2006). Upon entry to the cell, choline is either immediately phosphorylated to phosphocholine, or irreversibly oxidized to betaine, which can also serve as a methyl donor to homocysteine in the formation of methionine via catalysis by the cytoplasmic betaine hydroxymethyltransferase (BHMT, Figure 1.4, reaction 14) (Zeisel and da Costa, 2009). The other product of the BHMT reaction is DMG, which forms CH_2-THF in the dimethylglyine dehydrogenase reaction (DMGDH, Figure 1.4, reaction 8). Sarcosine is formed either in the DMGDH reaction, or by glycine N-methyltransferase activity in the cytoplasm, and it can serve as a 1C donor in the mitochondria to form CH_2-THF by sarcosine dehydrogenase (SDH, Figure 1.4, reaction 9) (Tibbetts and Appling, 2010). DMGDH catalyzes DMG to sarcosine (mono-methylglycine) and CH_2-THF. SDH generates glycine, and in the presence of THF, CH_2-THF as well, as noted above, but in the absence of THF, the 1C unit is released as formaldehyde (Wittwer and Wagner, 1980). The formaldehyde can be oxidized by mitochondrial aldehyde dehydrogenase (ALDH2) to yield an alternate source of formate (Dorokhov et al., 2015). In folate-depleted rats, the ALDH2 reaction becomes the

primary mode of formate production, with sarcosine and dimethylglycine serving as 1C donors instead of serine (Morrow et al., 2015).

The next two reactions are catalyzed by bifunctional MTHFD2 or MTHFD2L, wherein CH_2-THF is oxidized first to 5,10-methenyl-THF (CH^+-THF) and then hydrolyzed to 10-formyl-THF (10-CHO-THF) (Figure 1.4, reactions 3m and 2m, respectively). Both enzymes exhibit dehydrogenase and cyclohyrolase activity. The redundancy of MTHFD2 and 2L in the mitochondria is currently not well understood. MTHFD2 is expressed in developing tissues and transformed cells in culture, but not adult tissues, whereas MTHFD2L is expressed in both embryonic and adult tissues (Di Pietro et al., 2004; Bolusani et al., 2011). MTHFD2-null mice are embryonically lethal, likely due to a defect in hematopoiesis caused by aberrant mitochondrial folate metabolism (Di Pietro et al., 2002). MTHFD2 has been of interest as a chemotherapeutic target, as tumors show a dramatic increase in MTHFD2 mRNA expression levels (Nilsson et al., 2014). Both MTHFD2 and 2L require NAD+ or NADP+ as a cofactor. Our lab has shown that both enzymes possess dual redox cofactor-specificity, although it was formerly thought that MTHFD2 was strictly NAD+-dependent (Shin et al., 2014, 2017; Mejia and MacKenzie, 1985).

The three fates assumed by the 1C unit of 10-CHO-THF in the mitochondria at this point are to be released as formate, (Figure 1.4, reaction 1m), be oxidized to CO_2 (Figure 1.4, reaction 11), or provide the formyl group for the initiation of mitochondrial protein synthesis (Figure 1.4, reaction 12). In all three cases, free THF is returned to the mitochondrial pool. In the conversion of 10-CHO-THF to formate, the 10-CHO-THF synthetase protein MTHFD1L produces ATP from ADP and P_i, and returns THF to the mitochondrial folate pool (Figure 1.4, reaction 1m); once formate is produced, it rapidly diffuses into the cytoplasm (Barlowe and Appling, 1988; García-Martínez and Appling,

1993). MTHFD1L is expressed in both adult and embryonic tissue (Pike et al., 2010; Prasannan et al., 2003), and in mice, embryos without MTHFD1L expression exhibit neural tube and orofacial defects with 100% penetrance (Momb et al., 2013). In humans, a common deletion/insertion polymorphism exists in *MTHFD1L* that affects splicing efficiency and also causes an increased NTD risk (Minguzzi et al., 2014; Parle-McDermott et al., 2009). In cancer cells, MTHFD1L expression was found to be upregulated, indicating that cancer cells may require mitochondrial formate for proliferation (Selcuklu et al., 2012). MTHFD1L will be further characterized in Chapter 1.3.

Mitochondrial 10-CHO-THF dehydrogenase, encoded by the ALDH1L2 gene, catalyzes the oxidation of 10-CHO-THF to CO_2 and THF in a $NADP^+$ dependent reaction (Figure 1.4, reaction 11). ALDH1L2 is expressed in mitochondria of liver (Barlowe and Appling, 1988), retina, and brain in the rat (Neymeyer and Tephly, 1994). The production of CO_2 is increased in uncoupled mitochondria, and depends on $NADP^+$ and THF in soluble extracts (García-Martínez and Appling, 1993). Additionally, it has been proposed that 1C metabolism plays a role in redox metabolism by contributing to NADPH production via ALDH1L2 activity, based on work done in cancer cell lines (Ducker et al., 2016; Tedeschi et al., 2013). ALDH1L2 will be further characterized in Chapter 1.4.

The final pathway taken by 10-CHO-THF is to formylate the initiator tRNA, Met-$tRNA^{Met}$, which has been observed in bacterial, yeast, chloroplast, and mitochondrial systems (Figure 1.4, reaction 12) (Halbreich and Rabinowitz, 1971; Kozak, 1983). Metazoan mitochondria, unlike bacterial systems, express a single $tRNA^{Met}$ that fulfills the roles of both initiation and elongation, thereby those designated for initiation purposes are formylated by 10-CHO-THF via methionyl-tRNA formyltransferase (MTFMT) (Anderson et al., 1981). Mitochondrial translation initiation factor ($IF2_{mt}$) has

been shown to have a high affinity for fMet-$tRNA_i^{Met}$, which initiates protein translation at the P site of the mitochondria (Spencer and Spremulli, 2004).

Although formylation of Met- $tRNA^{Met}$ has been shown to be nonessential in some systems (Newton et al., 1999; Li et al., 2000; Tibbetts et al., 2003), depletion of cellular formylation activity has also been shown to cause growth defects in *E.coli* (Guillon et al., 1992; Varshney and RajBhandary, 1992; Meinnel et al., 1993), and human mutations in MTFMT have been associated with the neurological disorder Leigh's syndrome, as well as defective mitochondrial protein synthesis (Tucker et al., 2011).

1.2.2.3 Cytoplasmic One-carbon Metabolism

The distribution of folates in the cytosol differs from that of the mitochondria. In the cytoplasm of rat hepatocytes, 45% of THF was in the form of 5-methyl-THF, 30% was assumed by 10-formyl- and 5-formyl-THF, and 25% was found to be free THF (Horne et al., 1989). In the cytoplasm, the same oxidative reactions as in the mitochondria are present, but the cytoplasmic redox state favors a flow in the reductive direction (Figure 1.4, reactions 1-4). These cytoplasmic interconversions of the 1C-unit bound to THF are coupled with several biosynthetic reactions that contribute to purine synthesis, thymidylate production, and AdoMet restoration in the methyl cycle. Metabolic tracer experiments in mouse embryonic fibroblasts have shown that at least 75% of the 1C units that flow into the methyl cycle are mitochondrially derived (Pike et al., 2010).

The flow of 1C units into the cytoplasm commences with formate released from the mitochondria, which reacts with free cytoplasmic THF to form 10-CHO-THF in a reaction catalyzed by the 10-CHO-THF synthetase activity of the trifunctional C_1-THF-synthase (MTHFD1, Figure 1.4, reaction 1). This reaction consumes one ATP, resulting

in no net ATP production from the mitochondrial synthetase reaction. MTHFD1 is essential for life, as mice that do not express C_1-THF-synthase are embryonically lethal; furthermore, heterozygosity has been associated with AdoMet deficiency, altered homocysteine metabolism, and a decrease in uracil misincorporation in nuclear DNA in the liver (MacFarlane et al., 2009). The embryonic lethality of these mice as well as the dysregulated folate metabolism of the heterozygotes emphasize the importance of mitochondrially-derived formate as a 1C donor in purine synthesis, which is explained further in this section.

As in the mitochondria, 10-CHO-THF has several fates in the cytoplasm. One very significant destiny for 10-CHO-THF is to act as a substrate in *de novo* purine synthesis; 10-CHO-THF is used to formylate carbons 8 and 2 of the purine ring by glycinamide ribonucleotide (GAR) and 5-aminoimidazole-4-carboxamide ribonucleotide (AICAR) transformylases, respectively (Figure 1.4) (Wyngaarden, J.B. and Kelley, W.N., 1983). The ten step enzymatic pathway of *de novo* purine biosynthesis is universal, and 10-CHO-THF is essential as a cofactor for the key formylation steps (Barlowe and Appling, 1988; Pasternack et al., 1994; Warren et al., 1996).

Alternately, cytoplasmic 10-CHO-THF dehydrogenase (ALDH1L1) oxidizes 10-CHO-THF to CO_2 and THF. With extremely high expression levels in adult liver, ALDH1L1 accounts for 1.2% of total cellular protein (Cook and Wagner, 1982). ALDH1L1 is downregulated in cancer tissue and has been shown to have suppressive effects on cancer cell growth (Krupenko and Oleinik, 2002), which is consistent with its impact of diminishing nucleotide biosynthesis. Conversely, it has been shown to be upregulated during CNS development (Anthony and Heintz, 2007), thereby suggesting that the regulation of ALDH1L1 requires further analysis.

Finally, 10-CHO-THF may be reduced to CH_2-THF by the cyclohydrolase and dehydrogenase activities of MTHFD1 (Figure 1.4, reactions 2 and 3). CH_2-THF can serve as a 1C donor for thymidylate synthesis (Figure 1.4, reaction 10) or serine synthesis (Figure 1.4, reaction 4). Thymidylate synthase (TYMS, Figure 1.4, reaction 10) forms thymidylate (dTMP) from the reductive methylation of deoxyuridylate (dUMP), through a unusual folate 1C transfer where THF is oxidized to DHF (Santi and Hardy, 1987). DHF is restored the active folate cycle by being reduced back to THF by DHFR. As proliferating cells require rapid DNA synthesis, requiring an ample supply of thymidylate, TYMS is a common chemotherapeutic target (Peters et al., 2002).

Alternatively, CH_2-THF can be reduced to 5-methyl-THF (CH_3-THF) by methylenetetrahydrofolate reductase (MTHFR), irreversibly committing it into the methyl cycle (Figure 1.4, reaction 6). The most reduced 1C-folate unit, CH_3-THF is abundant in the cytoplasm and is produced by MTHFR in a NADPH-dependent manner. Disruptions in MTHFR functioning—such as that which occurs in the common human C677T MTHFR polymorphism—have been associated with NTDs, Alzheimer's disease, schizophrenia, cardiovascular disease, and autism, among others (Yang et al., 2015; El-Hadidy et al., 2014; Román, 2015; Liew and Gupta, 2015; Rai, 2016; Sener et al., 2014). These issues are consistent with the critical need of a steady supply of 1C units to the methyl cycle in order to maintain healthy cellular function.

Next in the methyl cycle, methionine synthase (MTR) consumes CH_3-THF, in a cobalamin (vitamin B12)-dependent fashion, releasing THF into the cytoplasmic folate pool and forming methionine from homocysteine (Figure 1.4, reaction 7). Homocysteine remethylation is particularly important because methionine is adenylated by AdoMet synthetase to form the reactive methyl carrier AdoMet, which is the universal methyl donor for DNA, RNA, proteins, and phospholipids (Cantoni, 1951; Chiang et al., 1996).

Not only does it play an influential role in epigenetics, but AdoMet is considered the second most important cofactor after ATP, and functions in sulfur metabolism as well as the biosynthesis of creatine, polyamine, and phosphotidylcholine (Finkelstein, 1990; Mudd et al., 2007; Su et al., 2016). Methylation by AdoMet releases S-adenosylhomocysteine (AdoHcy) as a byproduct; in adult mammals, the greatest source of SAH and thereby the largest 1C sink is phosphotidylcholine synthesis from phosphoethanolamine (Stead et al., 2006). SAH hydrolase catalyzes the breakdown of SAH into adenosine and homocysteine (Turner et al., 2000), the latter of which can either re-enter the methyl cycle, or synthesize cysteine via the transsulfuration pathway (Mudd et al., 1965).

Finally, CH_2-THF that does not enter the methyl cycle or produce thymidylate transfers its 1C unit to glycine in a reaction catalyzed by cytosolic SHMT1, forming serine and releasing THF back to the cytoplasm. SHMT1 has been shown to compete with MTHFR for CH_2-THF, as AdoMet levels decrease when SHMT1 is overexpressed in mice (MacFarlane et al., 2011). Mice lacking SHMT1 are viable and fertile, indicating that this enzyme does not produce essential 1C units; however, when fed a folate-deficient diet, these mice experience an increase in NTDs compared to WT (MacFarlane et al., 2008). The viability of *shmt1*-null animals is likely due to the fact that the most serine synthesis occurs in the mitochondria (via SHMT2) rather than in the cytoplasm. Additionally, SHMT2 has been shown to produce two transcripts, one of which (SHMT2α) localizes to the nucleus and cytoplasm. SHMT2α is likely responsible for SHMT-dependent thymidylate synthesis that occurred in the absence of SHMT1 in isolated liver nuclei (Anderson and Stover, 2009).

1.2.2.4 Nuclear One-carbon Metabolism

Within the nucleus, there exists a dTMP synthesis cycle catalyzed by TYMS, DHFR, and SHMT1 (Woeller et al., 2007). This cycle involves a unique folate 1C transfer, catalyzed by TYMS, wherein the THF carrier is oxidized to DHF in the transfer of electrons to the 1C unit—thereby reducing it to a methyl group, which is transferred to dUMP to form dTMP (Figure 1.4, reaction 10n). DHF is reduced back to THF and restored to its active state in the folate pool by DHFR (Figure 1.4, reaction 13). Serine serves as the 1C donor via SHMT1 (Figure 1.4, reaction 4n, Anderson and Stover, 2009), which confirms previous studies in MCF-7 cells that established SHMT1 as rate-limiting for dTMP synthesis (Herbig et al., 2002). During S and G2/M phases of the cell cycle, TYMS, DHFR, and SHMT1 are all modified with a small ubiquitin-like modifier (SUMO), which cues them to translocate into the nucleus (Anderson et al., 2007; Woeller et al., 2007). Impaired thymidylate synthesis in the nucleus has been associated with accumulation of uracil in the DNA of mice, indicating that nuclear thymidylate synthesis is essential for maintaining DNA integrity (MacFarlane et al., 2011).

1.3 MITOCHONDRIAL 10-FORMYL-THF SYNTHETASE: MTHFD1L

1.3.1 Enzymatic Characterization

In a healthy cellular environment, the majority of 1C units used in cytoplasmic reactions are derived from formate produced in the mitochondria, catalyzed by MTHFD1L (reviewed in Tibbetts and Appling, 2010). The *MTHFD1L* gene encodes mitochondrial 10-formyl-THF synthetase, hence we refer to this enzyme as MTHFD1L. Although it shares 61% sequence similarity (Figure 1.5) with its trifunctional cytoplasmic counterpart C_1-THF synthetase (MTHFD1), MTHFD1L is monofunctional (Walkup and Appling, 2005). MTHFD1 and MTHFD1L both contain homologous C-terminal synthetase domains of approximately 70 kDa and homologous N-terminal dehydrogenase/cyclohydrolase domains of approximately 30 kDa, linked through a proteolytically sensitive connector region. Due to substitutions in the N-terminus of MTHFD1L, the dehydrogenase/cyclohydrolase domain is catalytically inactive (Christensen et al., 2005).

Our lab enzymatically characterized MTHFD1L, and found it to exist as a homodimer in solution. We first identified *MTHFD1L* in 2003 in human uterine RNA, and it was found to span 236 kilobase pairs on chromosome 6, consisting of 28 exons plus one alternative exon (Prasannan et al., 2003). The gene encodes a protein of 978 amino acids, and is expressed ubiquitously, with greatest abundance in placenta, spleen, thymus, and brain (Prasannan and Appling, 2009; Prasannan et al., 2003). Expression is observed ubiquitously at all stages of mammalian embryogenesis, with highest levels of localized expression in the brain, neural tube, craniofacial structures, limb buds, and tail bud (Pike et al., 2010).

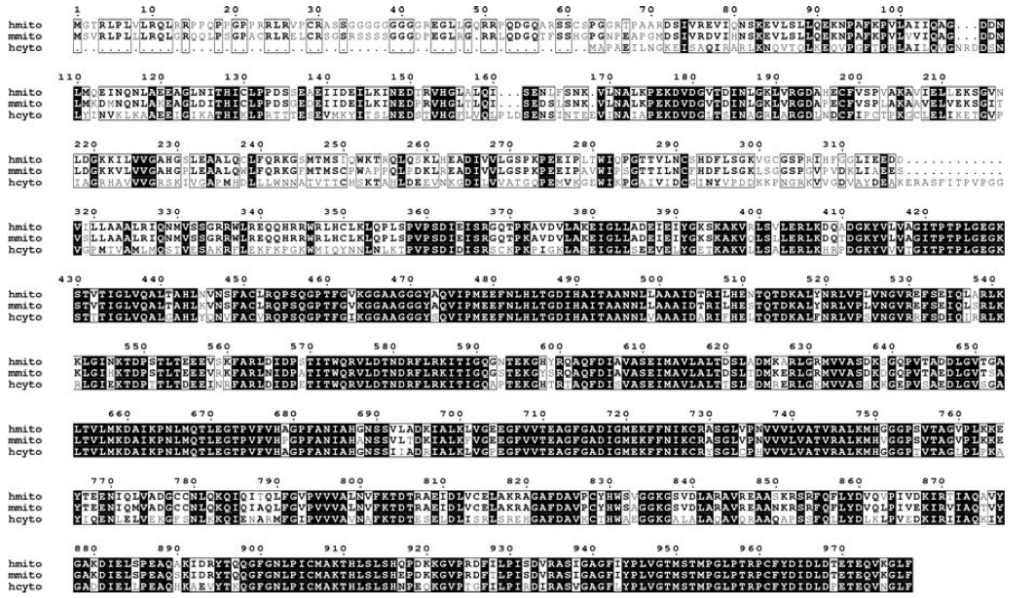

Priya Prasannan et al. J. Biol. Chem. 2003;278:43178-43187

The American Society for Biochemistry and Molecular Biology, Inc.

Figure 1.5 **Alignment of human and mouse mitochondrial MTHFD1L with human cytoplasmic MTHFD1**. *Black boxes* denote identity, and *white boxes* denote conservative substitutions or identities in two of three proteins. The alignment was produced by the INRA server at the Laboratoire de Génétique Cellulaire (prodes.toulouse.inra.fr/multalin/multalin.html) using the MultAlin algorithm, and the output was generated by the ESPript program at the same site. *hmito*, human mitochondrial MTHFD1L; *mmito*, mouse mitochondrial MTHFD1L; *hcyto*, human cytoplasmic MTHFD1 (Prasannan et al., 2003)

1.3.2 Implications in human health

Considering that mitochondrial formate is the 1C source for biosynthetic reactions of the cytoplasm, it is plausible that disruption in the production of this formate via MTHFD1L will have dramatic implications on cellular homeostasis. In separate microarray experiments, *MTHFD1L* was found to be upregulated in both breast and colon adenocarcinomas (Sugiura et al., 2004; Jain et al., 2012). Furthermore, an increase in *MTHFD1L* expression has been associated with metastasis of hepatocellular carcinomas in cancer patients (Lee et al., 2017). Beyond its associations with cancer, several polymorphisms in the human *MTHFD1L* gene have been independently associated with an increased risk of NTDs, coronary heart disease, and Alzheimer's disease.

Strongly correlated with increased NTD risk, the *MTHFD1L* deletion/insertion polymorphism rs3832406 involves a varying number of ATT repeats that influence splicing efficiency (Parle-McDermott et al., 2009). Because the intronic rs3832406 occurs in close proximity to an alternatively spliced exon, it possibly results in a shorter transcript that lacks synthetase activity, as previously reported by Priya Prasannan in our lab (Prasannan et al., 2003). This polymorphism was observed in an Irish population. The link between *Mthfd1l* polymorphisms and NTD risk has been shown to be affected by differences in microRNA regulation (Minguzzi et al., 2014)

In addition to NTDs, *MTHFD1L* has also been associated with coronary artery disease (CAD). In both British and German populations, the intronic SNP rs6922269A>G has been associated with cardiovascular mortality and CAD (Samani et al., 2007; Angelakopoulou et al., 2012; Franceschini et al., 2011; Hubacek et al., 2016; Morgan et al., 2011; Palmer et al., 2014; Saade et al., 2011). Because mitochondrial formate is the source of at least 75% of 1C units that enter the methyl cycle and produce methionine from the methylation of homocysteine, MTHFD1L plays an active role in maintaining a

healthy level of homocysteine in the cell (Pike et al., 2010). Hyperhomocystemia has been shown to lead to endothelial cell damage, altered haemostasis, and a reduction in the flexibility of blood vessels (Ganguly and Alam, 2015), all of which reduce the quality of cardiovascular function. Folate supplementation has also been shown to significantly lower homocysteine concentration and reduce cardiovascular disease in patients (Ward, 2001).

Another polymorphism of *MTHFD1L,* rs11754661, has been implicated in neurological disorders—most predominantly, in Alzheimer's disease, but also autism and schizophrenia (Naj et al., 2010). The association of this SNP with late-onset Alzheimer's, a neurodegenerative disorder with cognitive impairment, was detected in Han Chinese populations, among others (Ren et al., 2011; Ma et al., 2012). As mentioned above, MTHFD1L plays an important role in preventing hyperhomocystemia; excessive homocysteine has been implicated as being neurotoxic by overactivating NMDA receptors that lead to a sustained phosphorylation of ERK-MAP kinase, causing uncontrolled cell death (Poddar and Paul, 2009). This hypothesis has been further supported in studies in humans and mice with elevated homocysteine levels and decreased MTHFD1L expression in the hippocampus (Naj et al., 2010; Hasegawa et al., 2010).

1.3.3 Mouse Models

The *Mthfd1l*-null mouse model was first reported by Jessica Momb of our lab, with an embryonically lethal phenotype and 100% penetrance of NTDs (Momb et al., 2013). Although all nulls have NTDs, these embryos exhibit variable phenotypes, including orofacial defects, craniorachiscisis, wavy neural tube, and exencephaly, with death occurring around embryonic day E12.5 (Figure 1.6). The null embryos are resistant

to folate supplementation, but the NTDs are partially rescued with sodium formate supplementation (Figure 1.7). The fact that folate does not prevent these birth defects from occurring indicates that the production of formate is essential for proper neural and orofacial development, thereby rendering the *Mthfd1l*-null mouse a model for folate-resistant NTDs.

Formate was also shown to prevent NTDs in a study that analyzed *Mthfd1l* expression in the curly-tail mouse (Sudiwala et al., 2016). The curly tail mouse, like *Mthfd1l*-null mice, is a folate-resistant NTD mouse model, with instances of both spina bifida and exencephaly. By an unknown mechanism, MTHFD1L expression is diminished in this model, and formate is able to prevent NTDs and increase litter size.

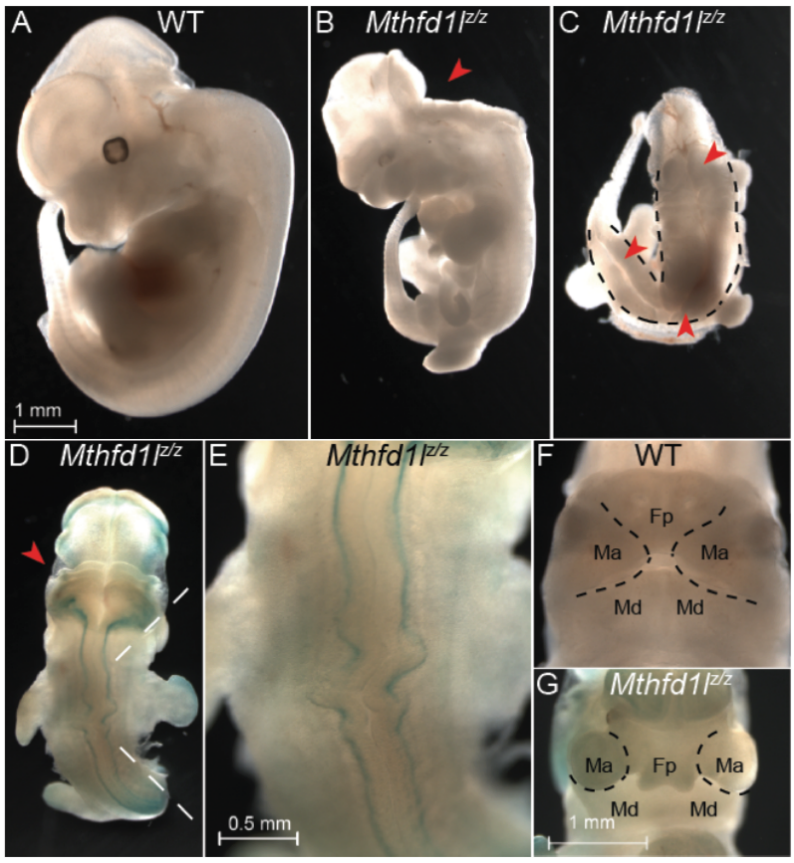

Figure 1.6 **Neural tube defects and orofacial defects in *Mthfd1l*$^{z/z}$ embryos.** "Compared with WT E12.5 embryos (A), E12.5 *Mthfd1l*$^{z/z}$ embryos (B-E) exhibit a spectrum of neural tube defects including exencephaly (B, red arrowhead). (C) Embryo with completely open neural folds (craniorachisisis) is indicated by the dashed lines. Note that the embryo curves to the left so the entire open neural tube is visible (red arrowheads). (D) Embryo with exencephaly (red arrowhead) and a wavy neural tube. (F) WT, 51-somite embryo showing normal facial development. (G) Same *Mthfd1l*$^{z/z}$ embryo (51 somites) imaged (D and E) displaying facial defects." (Momb et al., 2013)

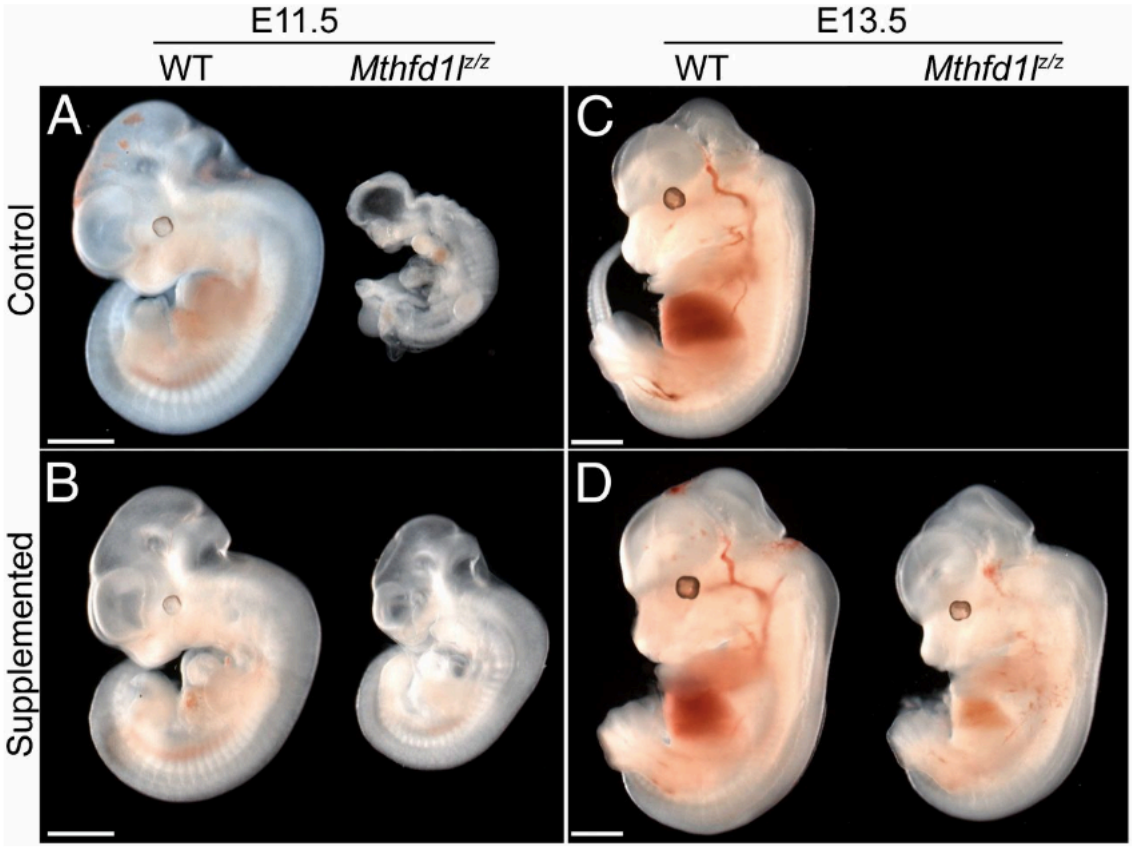

Figure 1.7 "**Maternal supplementation with sodium formate improves development and growth in *Mthfd1l*$^{z/z}$ embryos**. Pregnant dams were administered a calculated dose of 7,500 $mg \cdot kg^{-1} \cdot d^{-1}$ sodium formate. *Mthfd1l*$^{z/z}$ embryos dissected at E11.5 (*B*) Improved growth compared with control embryos from unsupplemented dams (*A*). E13.5 embryos from unsupplemented (*C*) and supplemented (*D*) dams. Precise age of embryos: (*A*) WT, 47 somites; z/z, 36 somites; (*B*) WT 45 somites; and z/z, 41 somites; (*D*) not determined because tails were not intact. (Scale bars, 1.0 mm.)." (Momb et al., 2013)

1.4 MITOCHONDRIAL 10-FORMYL-THF DEHYDROGENASE: ALDH1L2

Exceptional in the folate 1C pathway are the 10-formyl-THF-dehydrogenases; whereas other enzymes utilize THF for biosynthetic processes, these enzymes are catabolic. A human gene with 74% similarity to the cytosolic 10-formyl-THF dehydrogenase (ALDH1L1) was found to be localized to the mitochondria, and thereby is referred to as ALDH1L2 (Krupenko et al., 2010). Mitochondrial 10-formyl-THF dehydrogenase was found to be a later evolutionary product, based on gene analysis across species. Both ALDH1L 1 and 2 catalyze the formation of CO_2 and THF from 10-formyl-THF in an $NADP^+$ dependent manner, and they exemplify how folate metabolism has evolved to become functionally integrated into separate cellular compartments (Strickland et al., 2011a).

Structurally, ALDH1L2 is nearly identical to ALDH1L1, as the main difference in sequence arises from the 22 amino acid mitochondrial localization signal. Both isozymes possess a C-terminal aldehyde dehydrogenase domain, homologous to aldehyde dehydrogenases (ALDHs), and an N-terminal hydrolase domain, which are connected by an intermediate domain (Figure 1.8) (Strickland et al., 2011b; Tibbetts and Appling, 2010). The linker intermediate domain is both structurally and functionally homologous to acyl carrier proteins, and contains a site of attachment (Ser354) for a 4'-pentathione arm that swings to transfer the formyl group bound to the N-terminal domain over to the C-terminus (Donato et al., 2007; Krupenko, 2009). This mechanism is completed with the release of the formyl group as CO_2 by the aldehyde dehydrogenase domain. However, in the presence of exogenous thiols, this enzyme produces formate instead of CO_2 *in vitro* (Osborn et al., 1957; Min et al., 1988; Rios-Orlandi et al., 1986; Scrutton and Beis, 1979; Krupenko et al., 1995). The exogenous thiols in this reaction include 2-mercaptoethanol and dithiothreitol, and this hydrolase activity presents another hypothetical mechanism

for formate production by ALDH1L2 *in vivo*. Because mitochondria are rich in glutathione (more than 10mM), it is possible that the hydrolase activity of ALDH1L2 is supported in this organelle (Shen et al., 2005; Strickland et al., 2011a). Also of note, both ALDH1L1 and ALDH1L2 catalyze the hydrolase reaction with a similar K_m value, but the V_{max} of the mitochondrial isoform was about 7 times higher than its cytoplasmic counterpart (Strickland et al., 2011a). In *Mthfd1l*-null embryos, mitochondria continue to produce a low level of formate, and ALDH1L2 expression has been shown to increase (Bryant et al., 2018). Because mitochondrial formate production contributes so significantly to the biosynthetic cellular pool, these findings by Dr. Bryant suggest that ALDH1L2 may compensate for the lack of formate in the absence of MTHFD1L expression. In Chapter 4, I explore the metabolism of a mouse that does not express MTHFD1L or ALDH1L2 in an attempt to better comprehend the source of residual mitochondrially-produced formate in *Mthfd1l*-null embryos, and decipher if ALDH1L2 is a true source of formate *in vivo*.

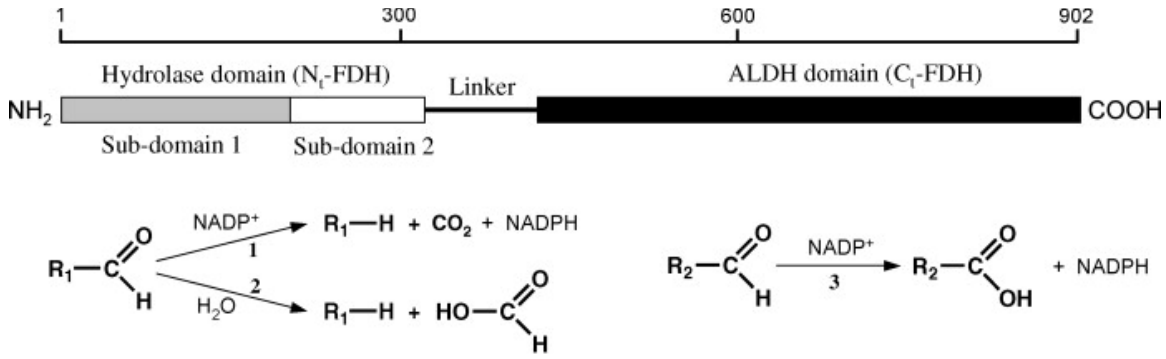

Figure 1.8 **Domain organization of mitochondrial and cytoplasmic 10-formyl-THF dehydrogenases and the reactions they catalyze**. The N-terminal hydrolase domain consists of residues 1-310 and the C-terminal ALDH domain contains residues 420-902. The full length enzyme is required for reaction 1, and the hydrolase reaction can be catalyzed by the full length enzyme or only the hydrolase domain (Krupenko, 2009).

1.5 OBJECTIVE

Six years ago, our lab established that mice lacking *Mthfd1l* expression are born with defects in neural tube closure (Momb et al., 2013). The mechanistic link that explains this failure of the neural tube to close remains undescribed and not well understood, however. Furthermore, we lack a thorough analysis of the metabolic differences that exist between wild-type and *Mthfd1l*-null mice with respect to spatial distribution in the tissue. Although the compartmentalization of folic acid derivatives has been thoroughly analyzed on a cellular level (reviewed in Tibbetts and Appling, 2010), we have yet to quantify and compare the distribution of folate-associated metabolites on a larger, tissue-based level during development, when the presence of folate is necessary for proper growth and morphology.

In this dissertation, I will describe my studies dedicated to better understanding the mechanisms of neural tube closure (NTC). In Chapter 2, I focus on the composition of cranial tissue during NTC using histology and immunohistochemistry. I expand this understanding to the biochemical realm in Chapter 3 by applying imaging mass spectrometry in an attempt to describe the biochemical landscape during tissue development. In Chapter 4, I introduce a novel mouse model that lacks two folate one-carbon pathway associated enzymes, Mthfd1l and Aldh1l2, both of which are associated with mitochondrial formate production. This double knockout mouse serves to demonstrate the importance of mitochondrially-derived formate in biosynthesis during the active changes that occur on the tissue level during neurulation.

CHAPTER 2: DELETION OF MTHFD1L IN MICE CAUSES MORPHOLOGICAL DEFECTS IN CRANIAL MESENCHYME AND EXTRACELLULAR MATRIX

2.1 INTRODUCTION

2.1.1 Overview

MTHFD1L is responsible for mitochondrial formate production, which accounts for 75% of 1C units that enter the methyl cycle (Pike et al., 2010). The methyl cycle is responsible for the production of methionine, an indispensable metabolite in all eukaryotic translation, as it serves as the initiating codon. Methionine is also the source of all methyl groups in the cell, via its conversion to AdoMet. In addition to the methyl cycle, MTHFD1L provides cytoplasmic formate as a source of 1C units for other biosynthetic reactions as well, producing purines and thymidylate. *MTHFD1L* is expressed throughout the entire embryo during all stages of development, and shows increased expression in the neuroepithelium, along the length of the folding neural plates, and the underlying paraxial mesoderm (Figure 2.1, Shin et al., 2014). Mice without *Mthfd1l* do not survive beyond E12.5, and experience 100% penetrance of birth defects, including exencephaly and craniofacial defects (Figure 1.5). In turn, proper neural tube closure and healthy development, especially in the cranial region, requires *MTHFD1L* expression. This chapter will focus on the mechanisms involved in cranial neural tube closure.

Recent experiments done by myself and colleague Dr. Minhye Shin have indicated that *Mthfd1l*-null mice display reduced density in the mesenchymal cells that underlie and expand the cranial neuroepithelium. A similar phenotype has been observed in cranial sections of mice treated with methyl cycle inhibitor (Dunlevy et al., 2006a).

This study examined the effect of methionine adenosyl transferase inhibition on embryonic development, which caused both exencephaly and a decrease in cranial mesenchyme density. In our lab, Dr. Shin examined a number of cellular processes in order to understand how *Mthfd1l* deletion in our mouse model led to a decrease in mesenchyme density. Using immunohistochemistry and *in situ* hybridization methods, she analyzed neuroepithelial cell proliferation, apoptosis, and neural crest cell specification. Phosphohistone H3 was used as a marker of cellular mitotic index to examine if *Mthfd1l* deletion led to a decrease in cellular proliferation, however there was no difference between the *Mthfd1l*-null mice and WT mice until after neural tube closure (18-24 somites) (Shin, 2016). The reduced cellular proliferation at this later stage is consistent with other 1C metabolism gene knockout mouse models, wherein proliferation is reduced between E9 - E11.5 (Pai et al., 2015; Tang et al., 2005). This reduction in cellular proliferation may be in response to the lack of neural tube closure in the hindbrain which occurs in the *Mthfd1l*-null mouse model.

Dr. Shin also examined apoptosis in this mesenchymal cell population using Caspase-3 as a marker, and observed no difference between the levels of apoptosis between WT and *Mthfd1l*-null mice. Because cranial mesenchyme is derived from both paraxial mesoderm and neural crest cells, it is also possible that the reduced cellular density was caused by a failure of neural crest cell migration to this region. The expression patterns of neural crest cell markers Sox9 and FoxD3 were examined using whole-mount *in situ* hybridization. Dr. Shin did not observe dramatic differences in staining of Sox9 or FoxD3 between somite-matched wild-type and *Mthfd1l*-null embryos, suggesting that neural crest cell specification was not dramatically affected by loss of *Mthfd1l.*

In this chapter, I further explore the cranial tissue morphology of the *Mthfd1l*-null mouse model, and the cellular and biochemical mechanisms at work during development of that morphology. Before delving into my work on this topic, I will review findings on cranial mesenchyme during neurulation in Chapter 2.1.2.

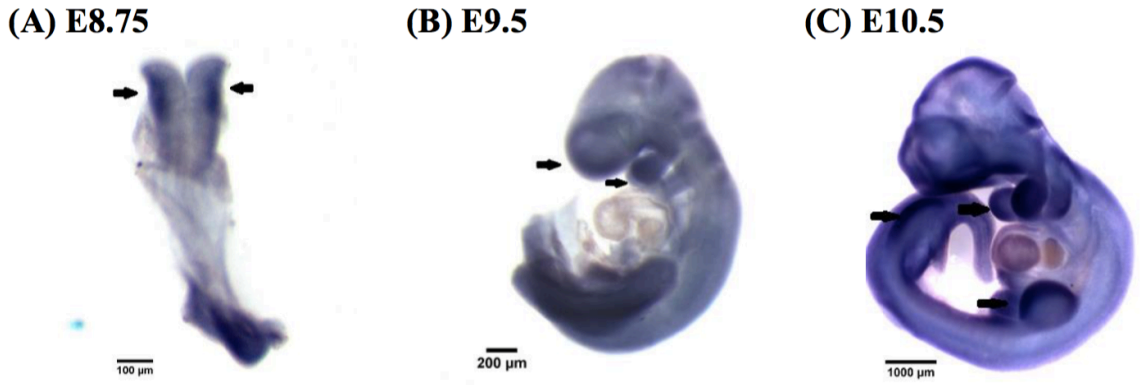

Figure 2.1. **Mthfd1l is expressed ubiquitously but most highly in the basal neuroepithelium**. Whole-mount in-situ hybridization at E8.75 (A), E9.5 (B), and E10.5 (C) show abundant expression of Mthfd1l in the developing forebrain, the limb buds, and the branchial arches (arrows). Expression is observed in the folding neural plates at E8.75 (arrows in A). This hybridization experiment was performed by Dr. Minhye Shin.

2.1.2 Mesenchyme and Extracellular Matrix (ECM) in Morphogenesis

In the nineteenth century, it was accepted as truth that both vertebrate and invertebrate embryos across all taxa develop identically. "Germ layer theory," popularized by Aleksandr Kovalevsky and Ernst Haeckel, posited that the three gastrulation-derived germ layers (ecto-, meso-, and endo-derm) give rise to a universal, fixed set of organs (Haeckel, 1874). Brothers Oscar and Richard Hertwig, among other embryologists of the late 1800s, refuted this claim, and coined the phrase "mesenchyme" to describe a protoplasmic network, filled with a fluid intercellular substance, that may be derived from all three germ layers, but is primarily mesodermal in origin (Hertwig and Hertwig, 1881). They further described that mesenchyme gives rise to a variety of tissues depending on the organism, albeit most are connective in nature. This early view sheds light on the structural importance of mesenchyme, as well as the interconnectivity this tissue maintains with its extracellular matrix.

Mesenchyme in the cranial region is derived from the anterior paraxial mesoderm and the neural crest. Both populations are required for neural fold elevation in rodent and chick embryos (Morriss-Kay, 1981; Fleming et al., 1997; Colas and Schoenwolf, 2001; Copp, 2005). Paraxial mesoderm, originating from the primitive streak, migrates to the anterior region of the embryo along the underside of the presumptive neural plate from early gastrulation (E6.5) to neural tube closure (E9.5) (Yoshida et al., 2008). Simultaneously, neural crest cells are induced at the junction of the neural plate and epidermal ectoderm, undergo epithelial to mesenchymal transition, and migrate into the frontonasal region, first branchial arch, and trigeminal ganglion (Noden and Trainor, 2005). Mesenchyme from the paraxial mesoderm will ultimately form bones of the skull vault and muscles in the face; that from the neural crest eventually becomes cranial nerves, and additional bones and muscles of the face (Jiang et al., 2002). Defects in

cranial neural crest cell formation or emigration have been associated with exencephaly in mice, although the mechanism for how failure to close the cranial neural tube is not well understood (Bamforth et al., 2001).

As the newly formed mesenchyme cells populate the cranial region, which occurs between 7-10 somite stages, the neural folds begin to elevate, transforming the neural plate into a "V" shape with a neural groove in the center (Zohn and Sarkar, 2012). This marks the first phase of cranial neurulation, and several KO mouse models (*twist*, *Cart1, Ski, Alx3, Inka1*) have demonstrated that cranial mesenchyme is essential to this phase (Berk et al., 1997; Chen and Behringer, 1995; Copp et al., 2003; Lakhwani et al., 2010; Reid et al., 2010; Zhao et al., 1996). During neural fold elevation, the amount of cranial mesenchyme cells increase, as well as the space between the cells, resulting in expansion of the tissue (Morriss and Solursh, 1978; Morris-Wiman and Brinkley, 1990a). Neither proliferation nor apoptosis explains this dramatic increase in mesenchyme expansion and neural fold elevation (Morris-Wiman and Brinkley, 1990b). Correlative data in rodents have indicated that expansion of the extracellular matrix (ECM) drives mesenchymal cell translocation and neural fold elevation (Morriss and Solursh, 1978; Morriss-Kay, 1981; Morris-Wiman and Brinkley, 1990a; Zohn and Sarkar, 2012).

The ECM is composed of glycosaminoglycans (GAGs), proteoglycans (PGs), collagens, and non-collagenous glycoproteins. GAGs are linear, unbranched polysaccharides with a repeating disaccharide unit that contains hexosamine and uronic acid. These molecules are abundantly modified with carboxyl, sulfate, and hydroxyl groups, which give GAGs polyionic and electrostatic properties. In turn, they are osmotically active and attract Na^{2+} ions, which draws in water and causes the interstitial spaces surrounding GAGs to swell (Rozario and DeSimone, 2010). The swelling of this region opens up pathways that promote cellular migration, expansion, and other

processes involved in morphogenesis (Toole, 1997). A key element of the ECM in mesenchyme expansion is a GAG called hyaluronic acid (HA), as digestion of HA in cultured rat embryos causes cranial mesenchyme to collapse and a delay in neural tube closure (Morriss-Kay et al., 1986).

Much like the "protoplasmic network" described by the Hertwig brothers in 1886, cranial mesenchyme and the ECM together form a porous meshwork made of star-shaped cells and intercalating strands of ECM components that support neural fold elevation during neurulation (Morriss and Solursh, 1978; Morris-Wiman and Brinkley, 1990a; Zohn and Sarkar, 2012). Mesenchyme is completely surrounded by ECM components, which do not function as an inert scaffold, but rather have been shown to profoundly influence cell fate (Assis-Ribas et al., 2018; Gattazzo et al., 2014; Hall and Watt, 1989; Wang and Chen, 2013; Watt and Huck, 2013). Integrins on the mesenchymal cell surface associate with PGs present in the ECM, which vary in concentration and composition throughout the extracellular network. Integrins also attract focal adhesion proteins which serve to associate the mesenchyme with cell signaling pathways and also the cytoskeleton, thereby allowing for proper cell migration in the expanding cranial tissue.

Among other GAGs, HA has been demonstrated to maintain healthy mesenchyme development both in cell culture models and *in vivo* in rodents (Chen et al., 2007; Morriss-Kay et al., 1986; Morris-Wiman and Brinkley, 1990a). The matrices surrounding migrating and proliferating cells in the developing embryo are enriched in HA, which interacts with cell surface receptors CD44 and RHAMM to further stimulate cell morphogenesis and proliferation (Toole, 1997). With the exception of HA, all GAGs form PGs through covalent linkages with glycoproteins of the basement membrane, such as the collagens, fibronectin, laminins, biglycan, and tenascins. These different PGs further influence cell fate by altering the structural integrity that may enhance or restrict

cell movements, as well as controlling the diffusion of morphogens or providing binding sites for other elements of the ECM (Rozario and DeSimone, 2010).

2.2 Materials and Methods

2.2.1 *Mthfd1l* Mouse Model

This study used protocols approved by the Institutional Animal Care and Use Committee of the University of Texas at Austin, and care of animals was performed in accordance with the guidelines approved by the National Institutes of Health for the Care and Use of Laboratory Animals. All mice were maintained on a C57BL/6 genetic background, exposed to a 12-hour light/dark cycle, and fed commercially available laboratory chow (LabDiet 5K67). Heterozygous *Mthfd1l*$^{Z/+}$ mice were generated by crossing mice that harbored a floxed conditional cassette between exons 4 and 6 of the Mthfd1l gene with mice that expressed Cre recombinase under control of the E2a promoter (E2a-Cre), as previously reported (Momb et al., 2013).

2.2.2 *Mthfd1l* Mouse Model Genotyping

In order to genotype *Mthfd1l* mice, a forward primer (5'-GAGTATGTGATTGCTTGGACCCCCAGGTTCC-3'), a reverse primer for wild-type alleles (5'-TGGCTCCCGAGGTTGTCTTCTGGCTATGAT-3'), and a reverse primer for mutant alleles (5'-CGGCGCCAGCCGCTTTTTTGTACAAACTTG-3') were used. The genotyping method used was outlined by Stratman et al (Stratman et al., 2003).

2.2.3 Collection of *Mthfd1l* Embryos

Heterozygous *Mthfd1l*$^{+/-}$ mice were intercrossed to generate *Mthfd1l*$^{+/+}$ and *Mthfd1l*$^{-/-}$ mouse embryos. Litters were generated by timed matings wherein 0.5 days of embryonic development (E0.5) had elapsed by noon of the day a copulation plug was observed. Pregnant females were sacrificed at both E8.75 and E9.5 for this study. They were killed by asphyxiation, and embryos were dissected from the uterus in chilled PBS under a Zeiss light dissection microscope. Embryos were rinsed in PBS and fixed in 4% paraformaldehyde in PBS at 4ºC overnight.

2.2.4 Histology

For histological analysis, fixed embryos were washed twice with room temperature PBS, then incubated in 70% EtOH for 5 minutes, 95% EtOH for 5 minutes, 100% EtOH for 5 minutes twice, then incubated in Xylene Substitute (Histo-Clear, National Diagnostics) for 5 minutes twice. Following these steps, the embryos were then transferred into Peel-a-way disposable plastic embedding molds (Polysciences, Inc) containing melted paraffin at 60ºC, and were incubated in that paraffin for 5 minutes. The molten paraffin was then changed out, and the embryos were incubated again for 15 minutes. This was repeated for one last incubation of 30 minutes, after which the paraffin was again replaced and embryos were oriented for embedding in cassettes used for sectioning with a microtome. Embryos were then sectioned at 7µm and mounted on positively charged glass microscope slides. Sections were then stained with Hematoxylin/Eosin (American Mastertech Scientific, Inc.) and imaged using a Nikon Eclipse Compound Microscope.

2.2.5 Quantitative Analysis of Head Mesenchyme Cell Density

Quantitative analysis of head mesenchyme cell density was carried out based on a previously described method (Dunlevy et al., 2006a). Cryo-sections of embryos were stained with DAPI and paraffin-embedded sections were stained with Hematoxylin and Eosin. Cell counting areas were defined as a percentage of the section being investigated by using boxes of defined dimensions located in a central site (8.5 % x 33.5 % of each section width) or a lateral site (8.5 % x 16.7 % of each section width). Image processing was conducted using ImageJ.

2.2.6 Alcian Blue Staining

Paraffin-sectioned embryos were deparaffinized with xylene substitute (Histo-clear), and rehydrated using an ethanol series (100%, 95%, 70%). Slides were then rinsed with 3% acetic acid in order to protect the subsequent alcian blue solution from pH changes due to the introduction of water. Slides were incubated in 1% Alcian blue solution at pH 2.5 (Abcam) for 30 minutes at room temperature, and then rinsed briefly with 3% acetic acid to remove the excess Alcian blue. Slides were rinsed in running tap water for 10 minutes, and then rinsed briefly in distilled water. The slides were counterstained with Nuclear fast red solution (Millipore-Sigma) for 5 minutes. Slides were rinsed with distilled water, then dehydrated with 95% alcohol, followed by two 100% alcohols, cleared with xylene substitute, and finally, cover-slipped. Alcian blue stained slides were imaged using a Nikon Eclipse Compound Microscope.

2.2.7 Cryoembedding and Sectioning of Embryos

Dissected embryos were placed in labeled glass vials, and fixed in 4% PFA in PBS at 4°C overnight. The samples were then washed twice in PBS, and then incubated

in 30% sucrose in PBS at 4°C overnight, or until the embryo sank to the bottom of the vial. The following morning, several drops of eosin were added to the sample in order to make the embryo more visible once it was embedded. One minute after eosin was added, the embryos were rinsed in PBS. The embryos were then incubated in a 1:1 mixture of OCT medium and 30% sucrose in PBS for 30 minutes on a rocking platform. Using the Zeiss light dissection microscope, embryos were properly oriented and embedded in OCT medium in cryomolds (Tissue-Tek), and flash frozen with ethanol and dry ice. The samples were stored at -80°C until they were sectioned. Immediately prior to cryosectioning, samples were stored at -20°C for 30 minutes.

Samples were sectioned at 7μm using a CryoStar NX50 cryostat, with the blade oriented perpendicular to the coronal axis to obtain transverse sections of the cranial tissue. Samples were air-dried at least 30 minutes, and stored at -80°C in a sealed slide box until they were analyzed using immunohistological methods.

2.2.8 Immunohistochemistry

Slides with cryo-sectioned embryos were laid at least 1 cm apart in a humid chamber lined with wet paper towels. Once slides were at room temperature, they were rinsed with PBS-T (0.5% (v/v) Triton x-100 in PBS) for 2 minutes, twice. Slides were then blocked for non-specific binding with 5% Normal goat serum (Cell Signaling Technology) in PBS-T for 30 minutes at room temperature. The primary antibody to be used was then diluted to the desired concentration for that specific antibody in 1% serum in PBS-T, and 75μL of the diluted primary antibody was added to each slide. The following primary antibodies were used: anti-collagen, type I (Millipore, 1:40 dilution), anti-collagen, type IV (Millipore, 1:50 dilution), anti-fibronectin (Millipore, 1:80 dilution), and anti-laminin alpha-5 (ThermoFisher, 1:50 dilution).

The slides were incubated in the desired primary antibody overnight at 4°C in the sealed humid chamber. The next morning, slides were washed twice with 1% serum-containing PBS-T for 10 minutes each. The secondary antibody used was goat anti-mouse Alexa Fluor 488 (Life Technologies), which was diluted 1:200 in 1% serum-containing PBS-T; 75µL of this dilution was added to each slide. They were incubated for 1 hour in the dark at room temperature. Slides were then washed twice with 1% serum-containing PBS-T for 10 minutes each. Excess wash was tapped off the slides and one drop of anti-fade mounting medium with DAPI (Vectashield) was added to the slide, and coverslips were applied (VWR).

Images were taken with a Zeiss Axiovert Inverted Fluorescent Light microscope, or a Zeiss 750 Laser Scanning Confocal microscope. Images were analyzed using ImageJ software (U.S. National Institutes of Health). Vimentin fluorescence intensity was expressed as corrected total cell fluorescence: background fluorescence was subtracted from total vimentin signal in mesenchyme, then normalized by area or number of cells (Total fluorescence – background fluorescence)/area or number of cells) (Lisi et al., 2012).

2.2.9 Statistical Analysis

To evaluate the Mendelian ratio of *Mthfd1l*-mutant embryos born and collected in this study, the Chi-squared goodness of fit test was used. For all other experiments in this Chapter, all quantitative data were compared using one- or two-way ANOVA (analysis of

variance), or Mann-Whitney U test. All statistical tests were performed using Prism version 8 (GraphPad, La Jolla, CA).

2.3 RESULTS

2.3.1 Mice Lacking *Mthfd1l* Show Delayed Growth and Developmental Progression

In order to evaluate the mechanism of action of Mthfd1l during NTC, embryonic litters were collected immediately before and after E9.5, which is the approximate embryonic day when neural tube closure occurs in the mouse. Analysis of these embryos at various developmental stages showed that *Mthfd1l*$^{z/z}$ embryos have a reduced somite number compared with WT littermates, and an open neural tube at E10.5. The genotypic distribution across embryos did not follow Mendelian ratios for inheritance of the *Mthfd1l*^{z} allele, and the observed ratio of *Mthfd1l*$^{+/+}$: *Mthfd1l*$^{z/+}$: *Mthfd1l*$^{z/z}$ was 91:134:51 (Table 2.1). A Chi-squared goodness of fit test reflected a p-value of 0.0008, indicating that the *Mthfd1l*$^{z/z}$ genotype causes embryonic death prior to E9.5. This is consistent with previous work with the *Mthfd1l* mouse model (Momb et al., 2013). Because *Mthfd1l*$^{z/z}$ mice develop more slowly than their WT littermates, somite matching was used to standardize comparisons across genotypes. At E9.5, *Mthfd1l*$^{z/z}$ mice are at the same somite stage of development as E8.75 WT mice (Figure 2.2), so in this chapter these ages were used when comparing embryos around the time of NTC.

Table 2.1: **The *Mthfd1l*$^{z/z}$ genotype causes embryonic death prior to E8.5**. Genotype distribution of litters from breeding of *Mthfd1l*$^{z/+}$ mating pairs over a one-year period. Analysis of 310 total mice.

***Mthdf1l* Genotype**	*+/+*	*z/+*	*z/z*	**Resorbed**
Observed	91 (30%)	134 (44%)	51 (16%)	34 (10%)
NTD?	0	0	100%	
Expected	77.5 (25%)	155 (50%)	77.5 (25%)	0

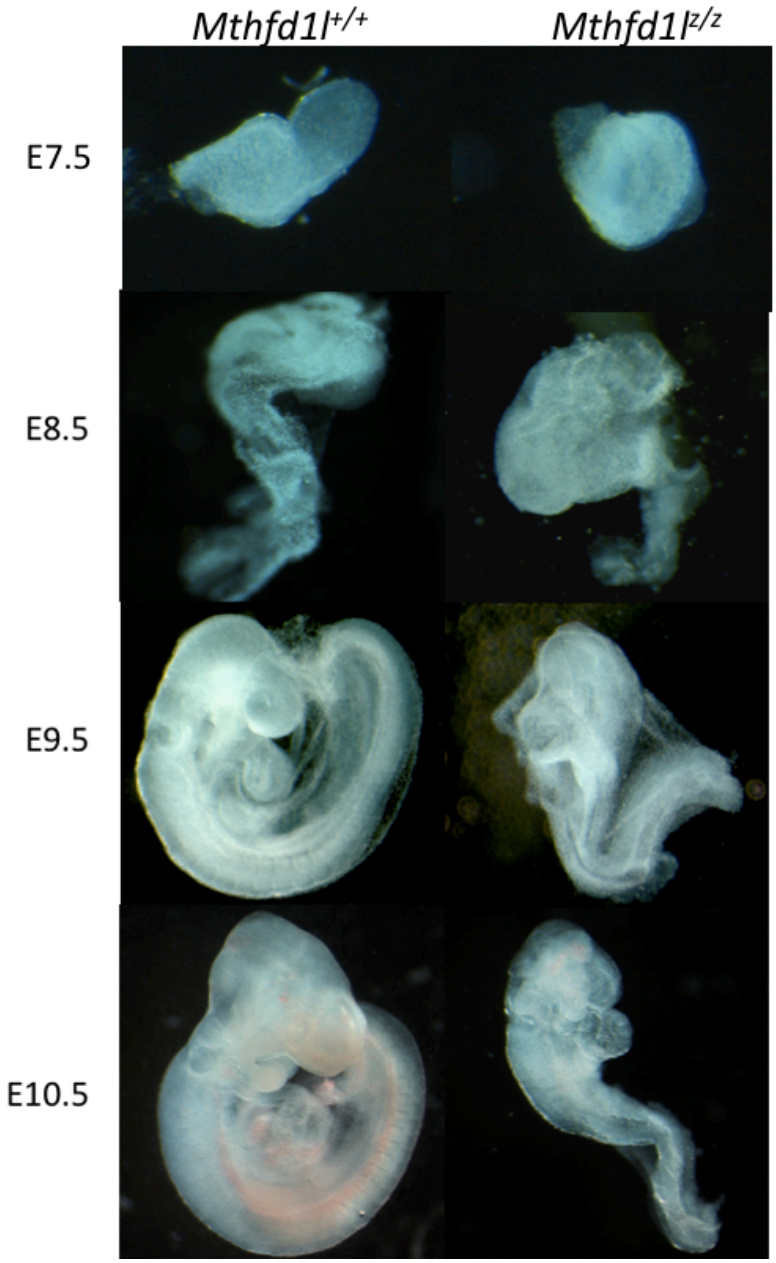

Figure 2.2**. *Mthfd1l* nullizygous mice are smaller than wild-type littermates and have an open neural tube**. Compared with wild-type embryos, *Mthfd1l*$^{z/z}$ embryos show delayed growth and developmental progression at all embryonic stages (E7.5 to E10.5). *Mthfd1l*$^{z/z}$ embryos at E9.5 have similar morphology with *Mthfd1l*$^{+/+}$ embryos at E8.75. *Mthfd1l*$^{z/z}$ embryos at E10.5 are similar in size with *Mthfd1l*$^{+/+}$ embryos at E9.5, but have defects in neural tube closure and orofacial development.

2.3.2 *Mthfd1l* Deletion Leads to Reduced Density of Cranial Mesenchyme

The head mesenchyme in *Mthfd1l*$^{z/z}$ embryos appeared sparser in the vicinity of the neural plate, especially underneath the neural plate. To examine the cell density of head mesenchyme with high morphological preservation, paraffin embedded and subsequent histological methods were utilized. Transverse paraffin sections of 7-13 somite stage *Mthfd1l*$^{+/+}$ and *Mthfd1l*$^{z/z}$ embryos were stained with Hematoxylin and eosin (H&E) to visualize nuclei, and cell density in the head mesenchyme was quantified (Figure 2.3 a, b). The total mesenchyme density was significantly lower in the mutant embryos compared to wild-type embryos (Figure 2.3 e). The decrease in cell density was most apparent in the mesenchyme underlying the neural plate (Figure 2.3 a, b). The apparent difference around the lateral edges of neural plate (Figure 2.3 d) did not reach statistical significance. These data suggest that the development of the head mesenchyme is abnormal in *Mthfd1l*$^{z/z}$ embryos, as evidenced by a total reduction in mesenchymal cell number compared to *Mthfd1l*$^{+/+}$ embryos.

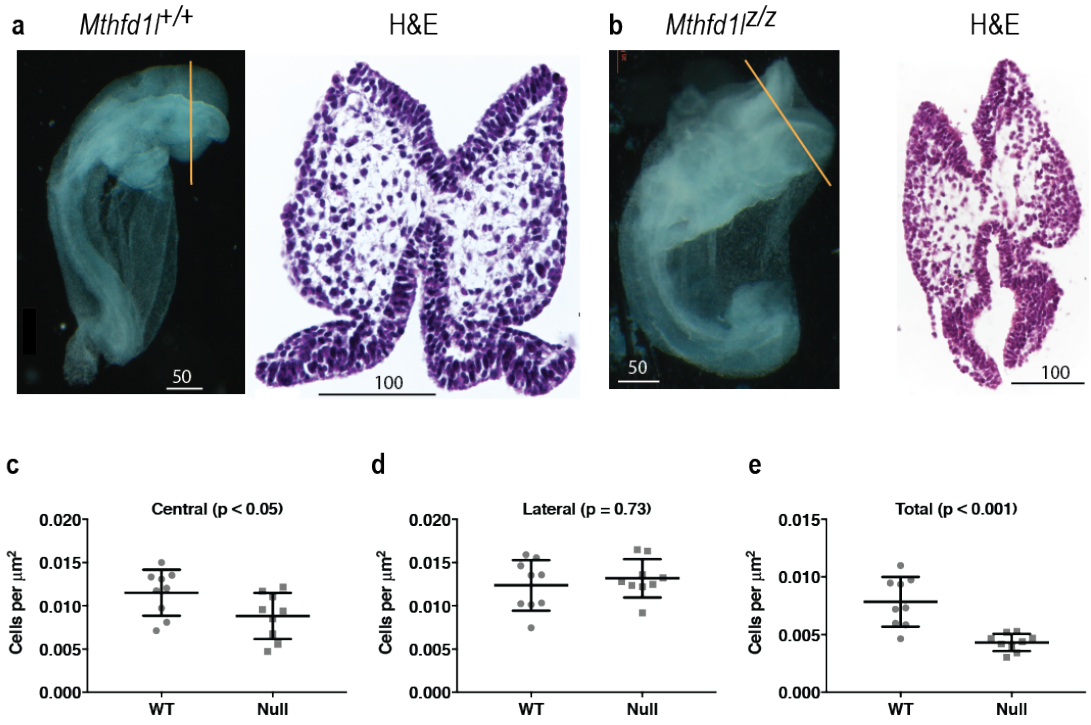

Figure 2.3. **Deletion of *Mthfd1l* causes reduced head mesenchyme density at 7-13 somite stages**. Representative transverse paraffin-embedded sections of wild type (A) and nullizygous embryos (B) show reduction in number of mesenchymal cells of nullizygous embryos in the cranial region. Straight line in the embryos (A-B) indicates the level of sections. Head mesenchyme density is significantly different in the central area as well as the total mesenchyme (C-E). Sections were stained with hematoxylin and eosin. n = three embryos in each genotype with three sections analyzed per embryo. Technical replicates are shown. P value was calculated by Mann-Whitney U test.

2.3.3 Deletion of *Mthfd1l* Causes a Reduction in Vimentin Expression

Vimentin expression was used as a marker for mesenchyme to further explore the defect in head mesenchyme development. At mouse embryonic day 8.5, vimentin expression is observed in cells of the primary mesenchyme and neural crest (Franke et al., 1982). Cryo-sections of 7-13 somite stage embryos were stained with anti-vimentin antibodies (Figure 2.4, upper panel). The fluorescence intensity of vimentin staining normalized by cell number in mesenchyme showed a trend toward higher vimentin expression in WT embryos, but did not reach significance (Figure 2.4, lower right panel; $p = 0.09$). However, when the intensity was normalized by mesenchyme area, vimentin expression was significantly lower in nullizygous embryos compared with WT embryos (Figure 2.4, lower left panel; $p < 0.05$). These data indicate that mitochondrial formate production via Mthfd1l is important in determining the density of cells that populate the cranial mesenchyme.

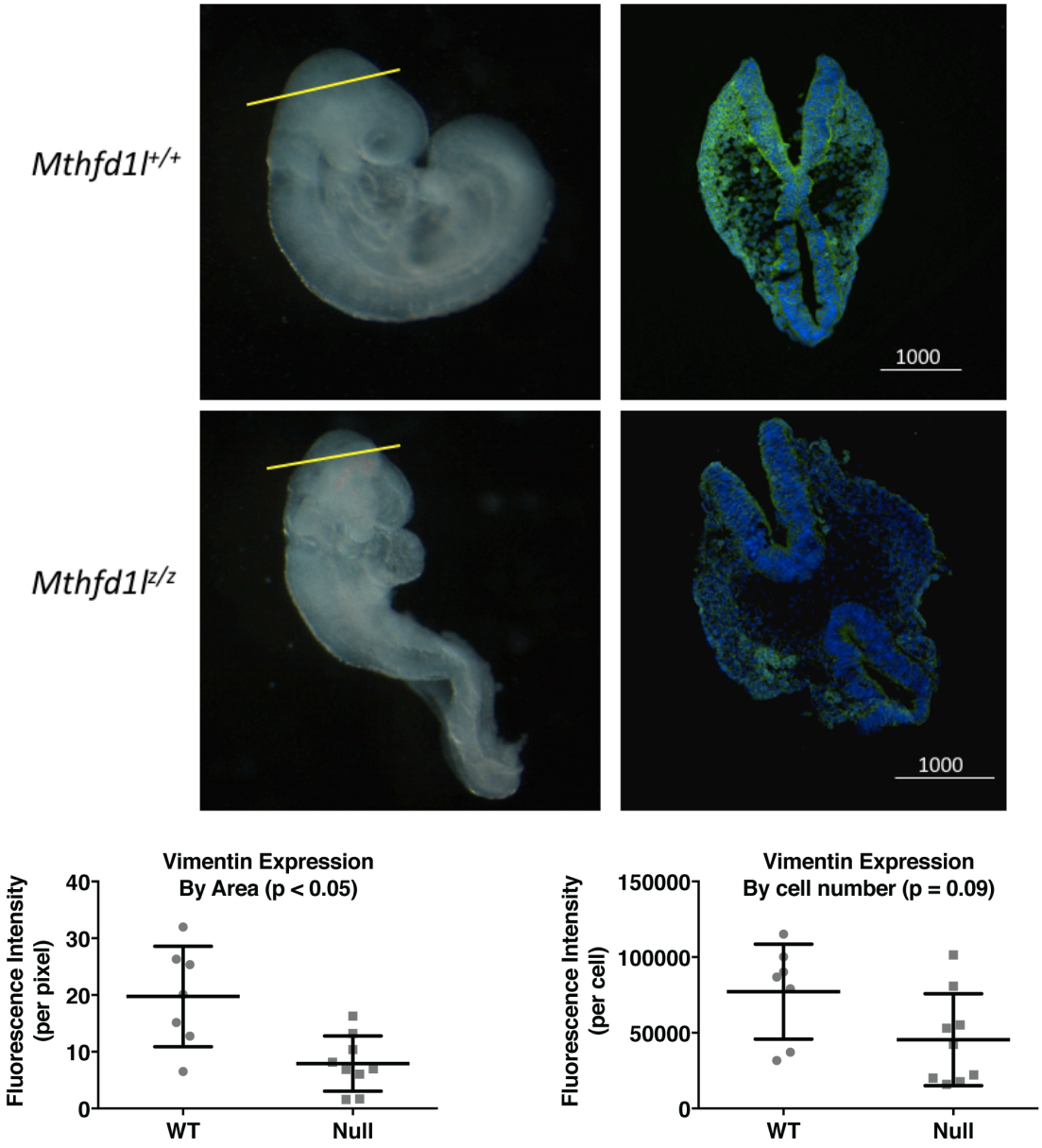

Figure 2.4. "**Vimentin expression is reduced in *Mthfd1l* mutant embryos at 7-13 somite stages.** Representative transverse cryo-sections of *Mthfd1*$^{+/+}$ (wild-type) and *Mthfd1*$^{z/z}$ (nullizygous) embryos were stained for vimentin and DAPI for nuclei. In the merged images, vimentin staining is green and DAPI staining is blue. Straight line in the whole embryos indicates the level of sections. Lower panel: fluorescence intensity of vimentin staining in the cranial region was normalized by mesenchyme area (left) or by mesenchyme cell number (right). n = three embryos in wild type and five embryos in nullizygotes with three sections analyzed per embryo. P values were calculated by Mann-Whitney U test."

2.3.4 Deletion of *Mthfd1l* Diminishes Hyaluronic Acid Content in the Extracellular Matrix

Following our discovery of a mesenchyme defect in the *Mthfd1*$^{z/z}$ embryo, the ECM was examined as a possible source of mesenchyme depletion. As HA has been shown to influence mesenchyme integrity during development (Morriss-Kay et al., 1986), abnormal HA concentration in the *Mthfd1*$^{z/z}$ cranial tissue might be associated with the observed reduction in mesenchyme cell number. Alcian blue staining of paraffin-sectioned embryos at the time of NTC was performed, and sections were qualitatively compared for differences in HA composition. Nuclear Fast Red stain was used as a counterstain. Compared to *Mthfd1*$^{+/+}$ sections, *Mthfd1*$^{z/z}$ embryos appear to have a reduced amount of HA in the ECM surrounding the embryonic cranial mesenchyme (Figure 2.5).

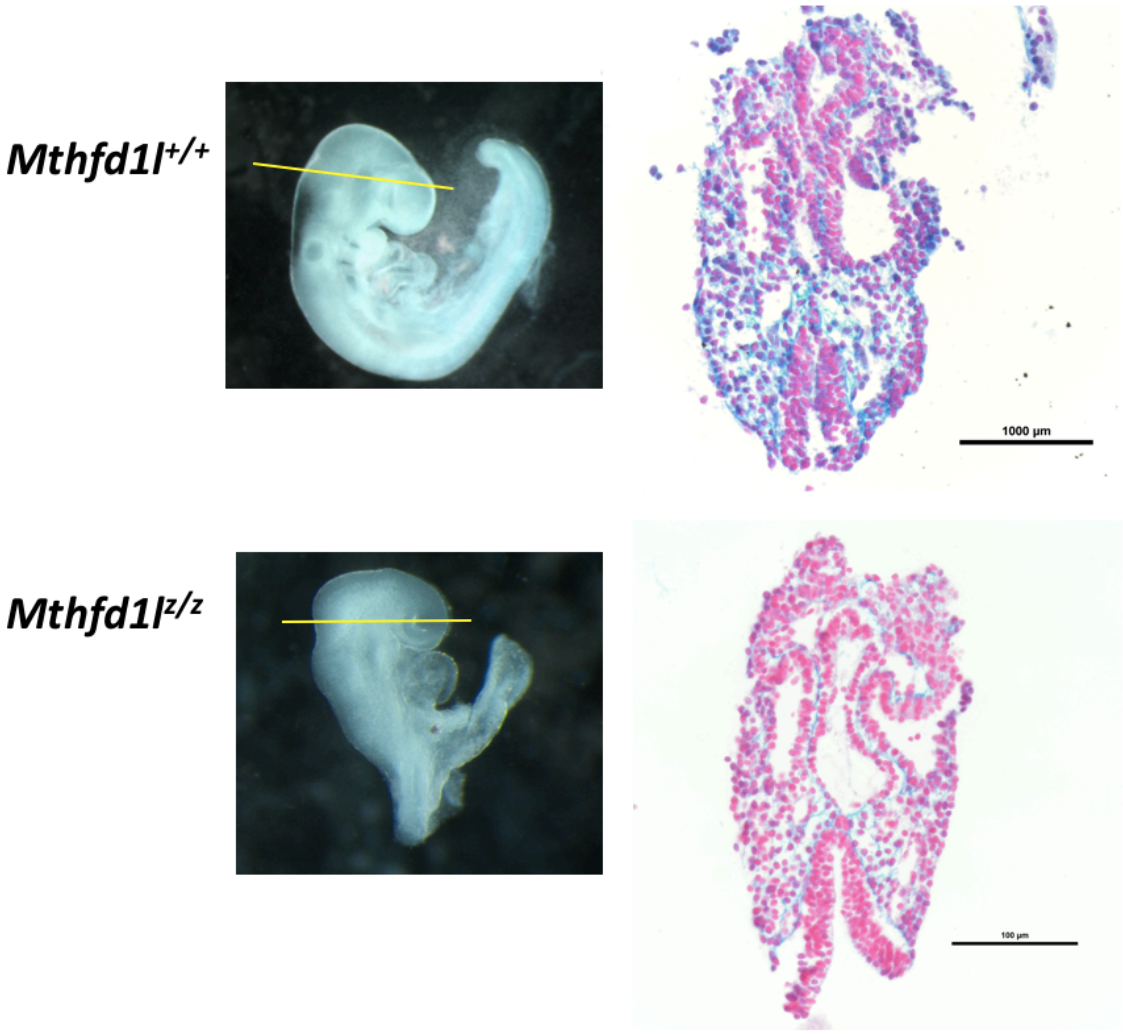

Figure 2.5. **Alcian blue staining indicates a reduction in HA concentration surrounding the cranial mesenchyme of *Mthfd1*$^{z/z}$ embryos**. Top panel: *Mthfd1*$^{+/+}$ embryo with Representative transverse paraffin section of cranial tissue, stained with alcian blue and nuclear fast red. Bottom panel: *Mthfd1*$^{z/z}$ embryo with Representative transverse paraffin section of cranial tissue, stained with alcian blue and nuclear fast red.

2.3.5 Immunohistochemistry of Extracellular Matrix Proteins

2.3.5.1 Mthfd1l Deletion Does Not Significantly Alter Fibronectin Expression

The extracellular matrix protein fibronectin is a principle component of the basement membrane that surrounds mesenchymal cells and plays an essential role in convergent extension during neural tube closure (Dady et al., 2014; Tada and Heisenberg, 2012). Mouse embryos lacking fibronectin exhibit a lack of somite condensation, as well as defects in neural tube morphogenesis, mesoderm specification, and yolk sac vasculature—they live until the approximate age of neural tube closure, E9.5 (Davidson et al., 2006; George et al., 1993; Georges-Labouesse et al., 1996; Le A. Trinh and Stainier, 2004; Linask and Lash, 1988a, 1988b).

Because a defect was observed in the glycosaminoglycan composition of the ECM of *Mthfd1l*-null embryos (Figure 2.5), fibronectin was analyzed to determine if ECM proteoglycan expression was also compromised, and if it may be related to the observed growth defects in these embryos. Twelve embryos, 6 of each genotype, were cryosectioned and analyzed using immunohistochemical methods, and fluorescence intensity was calculated and normalized to tissue area for each sample (μm^2). Three sections per embryo were analyzed to give one averaged value per biological replicate. There was a slight reduction in fibronectin expression in Mthfd1l-null embryo cranial tissue, however this difference was not statistically significant (Figure 2.6).

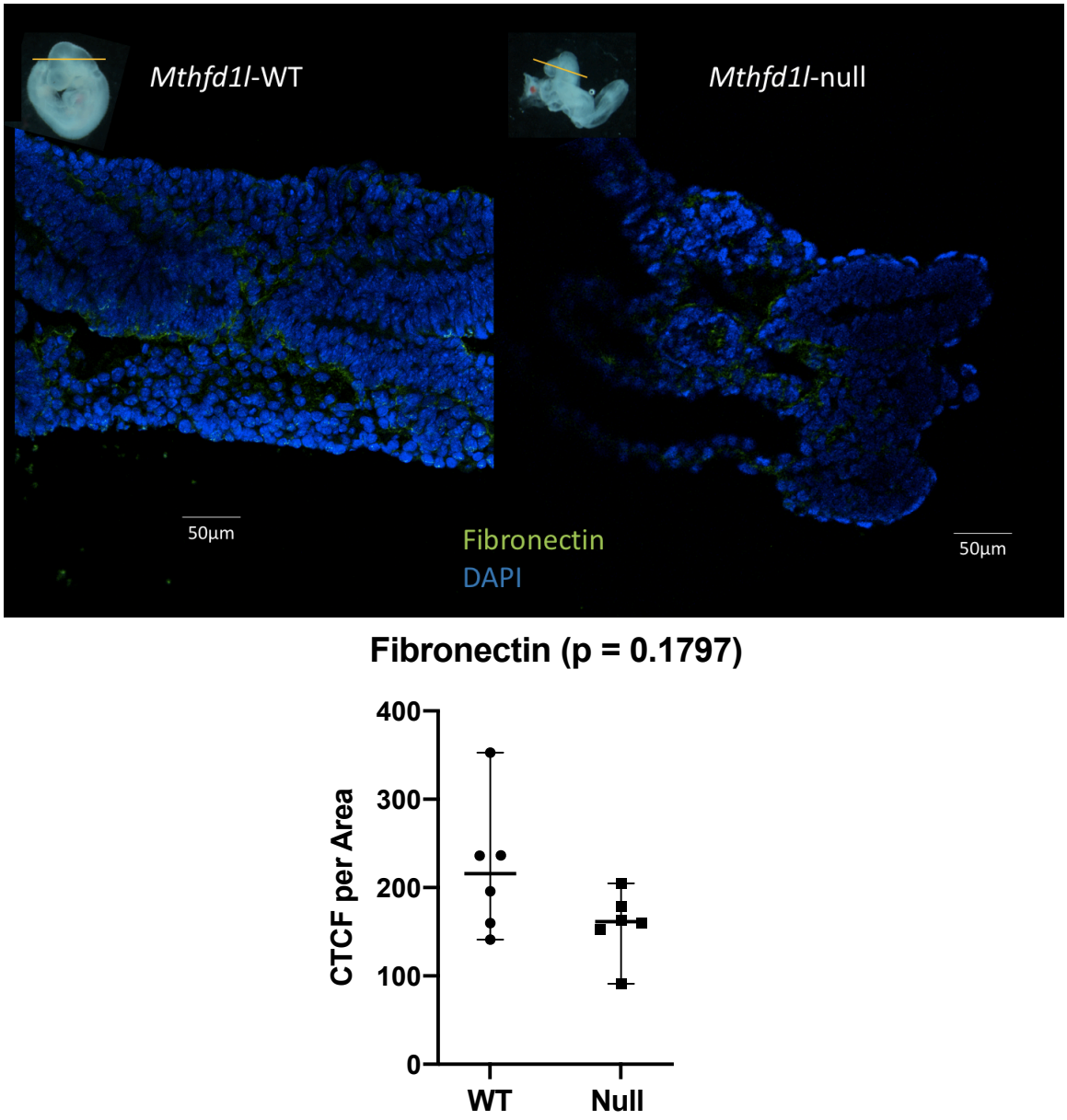

Figure 2.6. **Fibronectin expression does not differ significantly between WT and *Mthfd1l*-null embryos.** Fibronectin expression as measured by area in transverse cryosections of cranial tissue of WT and *Mthfd1l*-null embryos. The fluorescence intensity of fibronectin as shown in green in WT (left) and *Mthfd1l*-null (right) embryos is not significantly different (lower panel). Biological replicates of n=6 WT (circles) and null (squares) embryos were analyzed. Yellow lines indicate plane of section in embryonic cranial tissue evaluated. P values were calculated by Mann-Whitney U test.

2.3.5.2 Mthfd1l Deletion Significantly Alters Collagen IV Expression

Of all proteins in the animal kingdom, collagens are the most abundant. Mice lacking Collagen I do not live beyond E12, and exhibit mesenchymal cell death and defects in vascularization (Liu et al., 1995; Löhler et al., 1984; Schnieke et al., 1983); whereas those without Collagen IV (ColIV) expression die earlier, just before E10, and have defects in basement membrane integrity (Cosgrove et al., 1996; Miner and Sanes, 1996; Pöschl et al., 2004; Rheault et al., 2004). Because ColIV affects embryonic development in mice at an earlier stage, I first evaluated the possible association of *Mthfd1l* deletion and ColIV scaffolding in the basement membrane. Additionally, embryonic expression of ColIV has been associated with proliferation during development (Chamoux et al., 2002), therefore immunostaining was carried out to see if ColIV expression was altered in *Mthfd1l*$^{z/z}$ embryos. Nine WT embryos were cryosectioned and stained, and seven *Mthfd1l*$^{z/z}$ embryos were also analyzed. Flourescence intensity values (CTCF) per tissue area (μm^2) were evaluated in 3 sections per embryo, and averaged to give a final data point for each biological replicate. Mann-Whitney U analysis showed that there was a statistically significant lower Collagen IV expression in *Mthfd1l*-null compared with WT embryos (Figure 2.7).

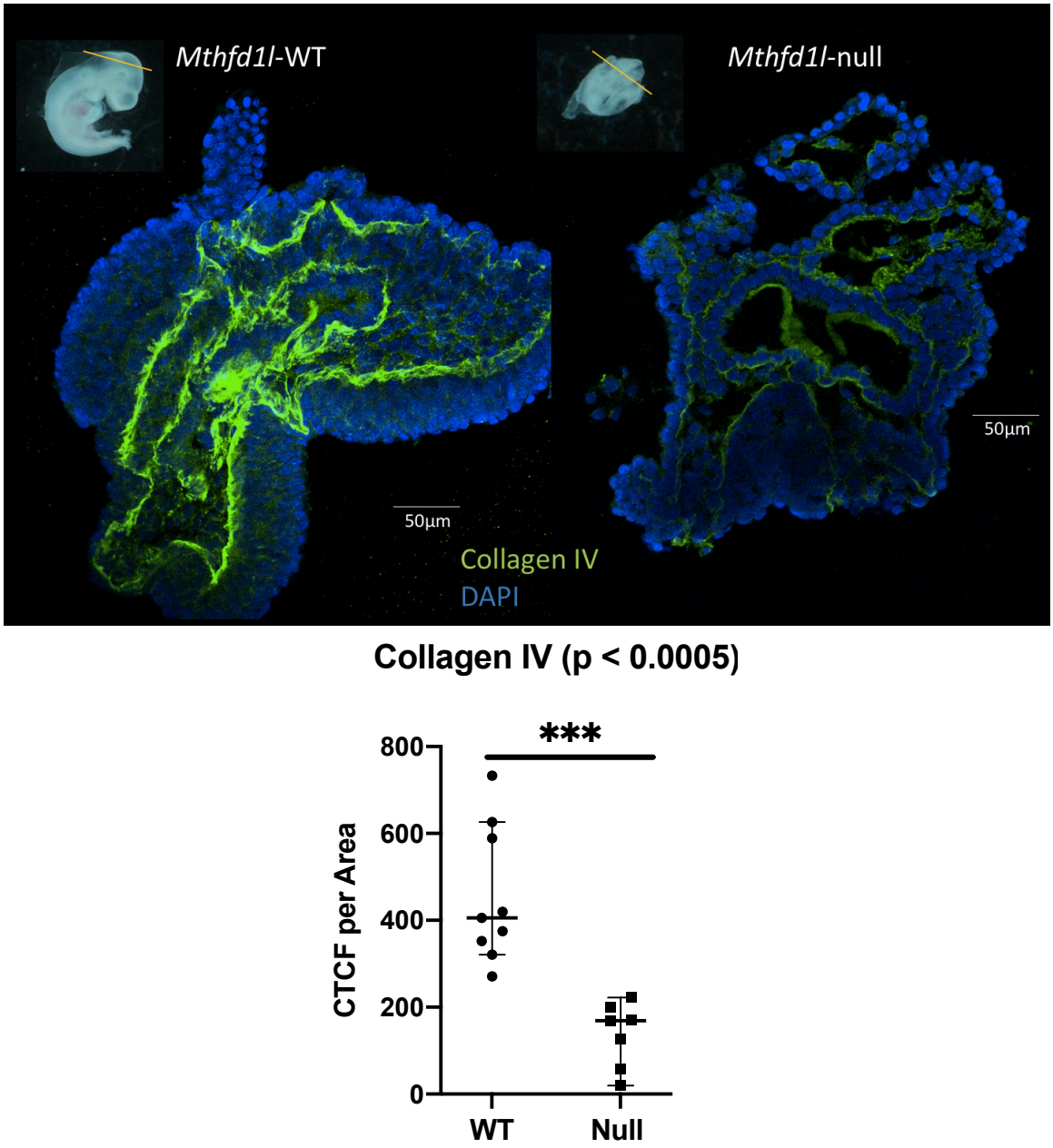

Figure 2.7. **Collagen IV expression is significantly decreased in *Mthfd1l*-null embryos.** Collagen IV expression as measured by area in transverse cryosections of E9.5 WT and *Mthfd1l*-null embryos. The fluorescence intensity of Collagen IV as shown in green in WT (left) and *Mthfd1l*-null (right) embryos is significantly different (lower panel). Biological replicates of n=9 WT (circles) and n=7 null (squares) embryos were analyzed. Yellow lines indicate plane of section in embryonic cranial tissue evaluated. P values were calculated by Mann-Whitney U test.

2.4 DISCUSSION

Mthfd1l is expressed at all stages during embryogenesis, and when it is defective, we observed neural tube defects, a delay in growth, and embryonic death at day E12.5 in the mouse (Momb et al., 2013). The biochemical mechanism by which Mthfd1l is associated with embryonic growth and neurulation is unknown, although one possible source of dysregulation is aberrant methylation. Mthfd1l is responsible for generating mitochondrial formate, which accounts for more than 75% of the 1C units that enter the methyl cycle (Pike et al., 2010). Around the time of neural tube closure, the mesenchyme in *Mthfd1l*-null mouse embryos is less dense (Figure 2.3), which parallels observations of methyl cycle disruption in mouse embryos at a similar age (Dunlevy et al., 2006b, 2006a). The methyl cycle is the source of the universal methyl donor S-adenosyl methionine (AdoMet), which is required for histone and DNA methylation, processes intrinsically linked to cell differentiation and migration (Horswill et al., 2008; Kobayakawa et al., 2007). Furthermore, aberrant DNA methylation in embryonic brain tissue has been associated with impaired maternal folate metabolism and the occurrence of NTDs (Chang et al., 2011; Lin et al., 2019; Wang et al., 2015). Because a large number of genes are involved in cranial neurulation (Copp et al., 2003), epigenetic dysregulation of any of these may result in embryonic cranial defects or exencephaly. In separate studies of methionine deficiency in rat embryos, it was demonstrated that AdoMet-dependent methylation of cytoskeletal proteins β-actin and tubulin are required for NTC (Coelho and Klein, 1990; Moephuli et al., 1997). Inhibition of the methyl cycle has also caused NTDs in the chick model (Afman et al., 2005), hence DNA and protein methylation are essential for NTC to occur properly, and decreased flux through the methyl cycle may explain why *Mthfd1l* deletion causes growth defects and NTDs.

The observed reduction of cranial mesenchyme cell density of *Mthfd1l*-null embryos (Figure 2.3, 2.4) may contribute to the development of exencephaly, as the elevation of neural folds is likely supported by the layer of mesenchyme below the neuroepithelium (Copp, 2005; Copp et al., 2003). This possibility is supported by the observation that digestion of hyaluronic acid (HA) in cultured rat embryos caused mesenchyme to collapse and delayed neural tube closure (Morriss-Kay et al., 1986). In our mouse model, we observed a decrease in mesenchyme density and lower HA abundance and distribution in the *Mthfd1l*-null embryo (Figure 2.5), both of which may contribute to the growth defect and open neural tube at E10.5. Based on these findings, we propose a model describing the relationship between Mthfd1l and NTC, wherein Mthfd1l expression in the neuroepithelium and underlying paraxial mesoderm leads to a high density of mesenchyme cells and adequate distribution of HA, allowing for neural plate elevation and DLHP formation (Figure 2.8). A lack of Mthfd1l expression throughout the paraxial mesoderm and neuroepithelium leads to a reduction in mesenchyme density, which produces insufficient forces on the neural plate to result in NTC. This model is only applicable to cranial neural tube closure, as mesenchyme expansion does not accompany spinal neural tube closure, and removal of the paraxial mesoderm also does not affect spinal neural tube closure (Copp et al., 2003; van Straaten et al., 1993).

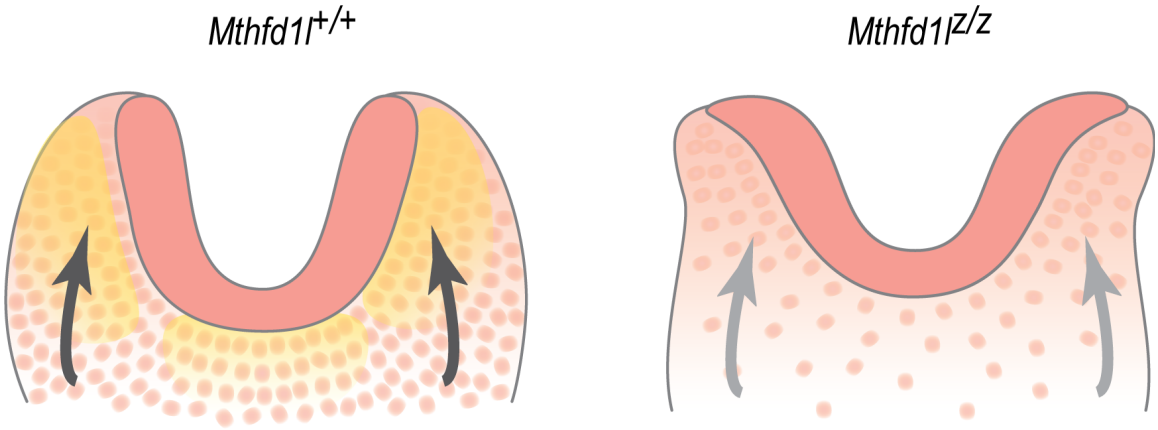

Figure 2.8. "**Schematic illustration of the cranial mesenchyme during neural fold elevation**. (left) Normal elevation of neural plates is supported by head mesenchymal cells in wild type embryos. (right) Apposition and fusion of neural plates are failed in *Mthfd1l* nullizygotes. Neuroepithelium and mesenchyme are shown in dark and light pink, respectively. Yellow shading in panel A indicates Mthfd1l expression. Arrows indicate physical forces generated by mesenchyme acting on the neural plates that drive neural fold elevation."

According to our model, in the absence of Mthfd1l expression, a reduction of mitochondrially-derived formate likely decreases flux through the 1C and methyl cycles, which retards development due to impaired biosynthesis as well as AdoMet-dependent epigenetic regulation and protein methylation, ultimately resulting in decreased cranial mesenchyme density. Aside from methyl cycle impairment (Dunlevy et al., 2006b, 2006a), the additional cellular mechanisms involved that cause reduction in cranial mesenchyme remain unknown. In past experiments, our lab examined proliferation, neural crest cell migration, and apoptosis, and found no major difference between WT and *Mthfd1l*-null embryos prior to neural tube closure (Shin, 2016). In this chapter, I explored the hypothesis that the ECM may be altered in the absence of Mthfd1l expression, as mesenchyme cells are surrounded by glycosaminoglycans (GAGs), structural proteins, and other ECM components that affect their behavior (Morriss and

Solursh, 1978). Because HA has been reported to influence the proliferation, migration, adhesion, and differentiation of mesenchyme (Chen et al., 2007; Knudson, 2003; Morris-Wiman and Brinkley, 1990a; Nilsson et al., 2003; Peck and Isacke, 1996), the diminished HA distribution observed in *Mthfd1l* nullizygous embryos may contribute to their impaired mesenchymal cell development. HA is enriched in developing tissue (Toole, 1997), and interacts with cells directly during embryogenesis directly via the receptor CD44 (Knudson, 2003). In order to further investigate the role of HA on reduced mesenchyme and failed neural tube closure, immunohistochemical staining of CD44 in *Mthfd1l*-null mesenchyme would more clearly indicate the extent of cell-matrix interactions.

The most abundant protein in the ECM is collagen, which contains a polypeptide chain with glycine as every third amino acid (~33% of the residues). *Mthfd1l*$^{z/z}$ embryos produce approximately half the amount of glycine as WT embryos (Bryant et al., 2018), which may affect collagen production as well. In this study, we found Collagen IV expression to be decreased in the absence of Mthfd1l (Figure 2.7), which is consistent with the hypothesis that glycine is required for collagen synthesis. We also examined the expression of fibronectin, another ECM protein required for embryogenesis and somite formation (George et al., 1993; Georges-Labouesse et al., 1996), however expression levels between null and WT cranial tissue were not significantly different (Figure 2.6).

In the future, immunohistochemical analysis of Collagen I expression would reveal if the phenomenon of decreased collagen expression is universal to all collagens, or specific to Collagen IV. Collagen I is associated with mesenchymal cell death, and like Collagen IV, Collagen I loss is embryonically lethal (Liu et al., 1995; Löhler et al., 1984; Schnieke et al., 1983). Another ECM protein associated with NTC is Laminin α5, which is responsible for directing the movement of neural crest cells along narrow streams, and

knockout mouse models have resulted in exencephaly, among other embryonic defects (Miner et al., 1998; Webb et al., 2007). It would be interesting to determine if Laminin α5 is altered in the *Mthfd1l*$^{-/-}$ embryo, as like Collagen IV, Laminin α5 is a component of the basement membrane, which lines the neuroepithelium and may be associated with the birth defects observed in the absence of Mthfd1l expression during development. Interestingly, proliferation of human fetal adrenal cells was induced with the addition of Collagen IV or Laminin α5 to the culture matrix; conversely, fibronectin encouraged apoptosis in the same cells in culture (Chamoux et al., 2002).

Finally, lineage tracing of the neural crest and paraxial mesoderm populations that form the mesenchyme would shed light on the mechanism of neural fold elevation and mesenchyme development. In the *Mthfd1l*-null mouse, the cause of reduced cranial mesenchyme density is not yet fully understood, therefore fate-mapping of the cells that ultimately form mesenchyme and elevate the neural folds is a way to explore the onset of this phenotype. This experiment can be done using Wnt1-cre and Mesp1-cre transgenic mouse lines to differentiate the neural crest and paraxial mesoderm, respectively, as described previously (Yoshida et al., 2008). These mouse lines can be bred with our lab's *Mthfd1l*$^{-/+}$mouse in order to elucidate why the *Mthfd1l*$^{-/-}$ mouse has reduced mesenchyme density and failed elevation of the neural folds. Furthermore, this experiment will isolate the relative contributions of neural crest cells and paraxial mesoderm during neural fold elevation.

CHAPTER 3: DESI-IMS OF *MTHFD1L*-NULL EMBRYOS

3.1 INTRODUCTION

Cell proliferation and differentiation are concurrent processes during development, and both greatly depend on metabolism (Agathocleous and Harris, 2013; Tennessen et al., 2011). One of the main functions of 1C metabolism is to provide anabolic intermediates for the biosynthesis of purines, thymidylate, and AdoMet, all of which are in great demand as cells proliferate and differentiate rapidly to meet the needs of a developing organism. In an effort to understand the metabolic processes disrupted by *Mthfd1l* deletion, our lab has performed untargeted metabolomics on whole WT and *Mthfd1l*-null embryos previously (Bryant et al., 2018). NMR and LC-MS analyses of whole embryo samples and mouse embryonic fibroblasts (MEFs) indicated that deletion of *Mthfd1l* leads to perturbations in amino acid metabolism, the TCA cycle, glycolysis, and 1C metabolism (Bryant et al., 2018). Comprehensive embryo metabolome analysis sheds light on how metabolism is altered in *Mthfd1l*-null embryos; however, because neural tube closure is driven by a number of morphogenetic processes, the spatial organization of the tissue is particularly relevant and should be taken into consideration in metabolic pathway analyses.

Recent technical advances in mass spectrometry have allowed for visualization of metabolism *in vivo* via imaging mass spectrometry (IMS). There is one report of the use of IMS on embryonic murine tissue, which revealed an increase in pools of citrate and lactate between E8.5 and E10.5, suggesting that glycolysis is upregulated during neural tube closure (Miyazawa et al., 2017). In that experiment, lactate was shown to accumulate along the dorsal neural tube and in the cranial mesenchyme at the time of neural tube closure, which is consistent with the onset of NTDs that result from

glycolysis inhibition in cultured embryos (Hunter and Tugman, 1995). Interestingly, our comprehensive metabolome study indicated that *Mthfd1l*-null MEFs have significantly decreased flux through glycolysis (Bryant et al., 2018). Although it is known that 1C metabolism, energy metabolism, and amino acid metabolism are altered in the *Mthfd1l*-null embryo, the metabolic flaws that result in aberrant neural tube formation remain elusive. The neural tube can be analyzed directly using IMS, offering a mechanistic link between 1C metabolism and morphology during development. In this chapter, I describe my collaboration with Rachel Dehoog of Dr. Livia Eberlin's lab, in which we use IMS to identify significantly altered metabolites in the cranial neural tube of the *Mthfd1l*-null mouse model that may contribute to the occurrence of NTDs. Ultimately, this work can be combined with future efforts to address how metabolism is coordinated with development.

3.2 Materials and Methods

3.2.1 DESI-based Imaging Mass Spectrometry (IMS)

In order to prevent excessive background signal detection from fixative materials, embryos were not fixed, but rather transferred directly into optimal cutting temperature (OCT) embedding medium, flash frozen with dry ice and ethanol, and stored at -80°C. Eight mouse embryos including 4 wild type and 4 null were sectioned at a thickness of 16µm using a CryoStar NX50 cryostat and stored at -80°C until analysis. Embryo sections were thawed at room temperature for ~10 minutes before desorption electrospray ionization mass spectrometry (DESI-MS) analysis. Sections were then imaged in the Eberlin lab with DESI-MS using a Q Exactive Orbitrap mass spectrometer (Thermo Fisher Scientific, CA) fitted with a 2D Omni spray stage (Prosolia Inc., IN) and a lab-built DESI sprayer. DESI-MS imaging was performed at a spatial resolution of 100µm in

the negative ion mode with a mass range of *m/z* 100-1,500 at a resolving power of 70,000. The solvent system of acetonitrile:dimethylformamide (ACN:DMF) 3:1 (v/v) was used at a flow rate of 1.2 μL/min. The N2 pressure set to 180psi. Ion images were assembled using Firefly and Biomap software. Ions were tentatively identified using high mass accuracy measurements and/or tandem mass spectrometry using higher-energy collisional dissociation (HCD).

After DESI-MS analysis, tissue sections were hematoxylin and eosin (H&E) stained and examined using light microscopy to identify sections containing cranial mesenchyme cell populations. Furthermore, Tandem Mass Spectrometry (MS/MS) was used following IMS analysis to confirm the identity of metabolites discovered by DESI.

3.2.2 Statistical Analysis for IMS

Three sections per embryo in the area of interest were selected to use for statistical analysis. One null embryo was excluded from statistical analysis due to its smaller size and low DESI-MS signal. For each section, 10 mass spectra corresponding to mesenchyme histology were extracted using MSiReader software. The data was then imported into R language where the mass range was discretized by binning each *m/z* value to the nearest hundredth. In this process, *m/z* bins that appeared in less than 10% of pixels were excluded and each mass spectrum was normalized to the median non-zero intensity, and then the logarithm of these normalized intensity values was taken.

Significance analysis of microarrays (SAM) analysis was performed in R using the SAM function from the samr library (Eberlin et al., 2014). A false discovery rate (FDR) of 0.05 was used to identify significant *m/z* values with altered abundances between the null and WT groups. SAM analysis was performed on the normalized values

from 10 mass spectra that corresponded to mesenchyme-containing regions, as explained in the above paragraph.

At this point, an average mass spectrum was calculated for each section and principal component analysis (PCA) was performed using the prcomp function in R. PCA was performed on the total average mass spectra, as well as on the 10 mass spectra that corresponded to mesenchyme-containing regions.

3.3 RESULTS

3.3.1 DESI-MS of Embryonic Cranial Mesenchyme

Our lab has previously conducted non-targeted metabolomics screens of whole *Mthfd1l*$^{-/-}$ embryos using NMR and MS (Bryant et al., 2018). Because the results of that study were not specific to our region of interest, the following MS-based experiments in this chapter are concerned with isolating regions where phenotypic differences exist in the *Mthfd1l*$^{-/-}$ mouse model; specifically, we directly analyzed metabolomics of the cranial mesenchyme using DESI-IMS.

Embryos were dissected around the time of neural tube closure and embedded in cryogenic OCT medium without fixing to avoid contamination of the MS signal during molecule detection. Once the embryos were sectioned, they were mounted on slides and the spatial metabolome of these samples were investigated with negative ion mode DESI-MS in the *m/z* range 100 to 1,500. The embryo tissue sections were sprayed with microdroplets of dimethylformamide:acetonitrile (1:1) solvent, which is histologically compatible and allows for H&E staining to be completed following DESI analysis (Eberlin et al., 2011), but first dissolves hundreds of metabolites, forming secondary

microdroplets that are analyzed by MS to produce a chemical map of the sample. The IMS-produced ion maps give spatial relevance to metabolism, providing information regarding the abundance and distribution of each *m/z* detected by this process.

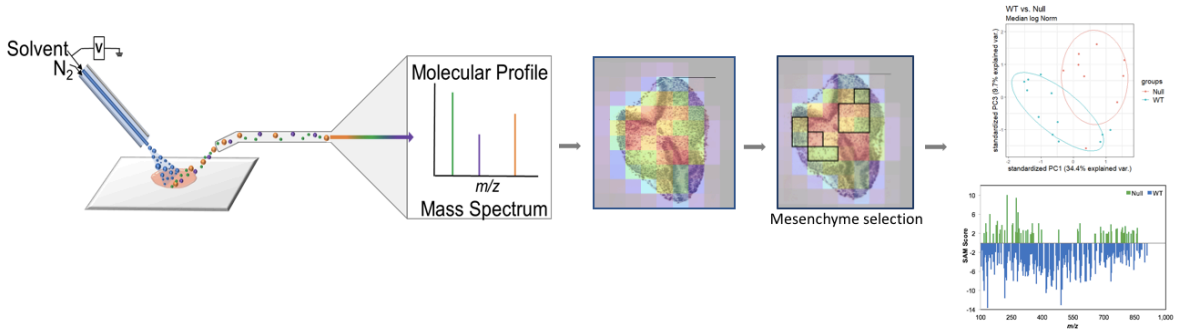

Figure 3.1. **Experimental design for targeted DESI-IMS of mouse embryonic cranial mesenchyme**. From left to right, following DESI-MS of sectioned cryoembedded embryos on microscope slides, visual spectra of region are viewed atop H&E stain of embryo section. Ten spectra that align with mesenchyme tissue are selected, and the average intensities of these spectra are used in PCA and SAM analysis.

As outlined in Figure 3.1, once both chemical mapping by DESI-IMS and H&E staining were completed, an overlay of the two images was used to identify the pixels correlating to the regions of the tissue containing mesenchyme. Ten pixels were selected for each sample, and these ten spectra were averaged for each sample, yielding an averaged mesenchyme spectrum. The averaged mesenchyme spectra of all samples from each group (WT: n=12; *Mthfd1l*-null: n=9) were averaged to produce a DESI-MS spectra of metabolites found in the mesenchyme (Figure 3.2). Given the hundreds of data points obtained by this method, the subtle (and some not-so-subtle) differences in metabolism between WT and *Mthfd1l*-null spectra are not immediately apparent from the spectra

themselves, however the alterations in specific metabolism were further explored by SAM analysis.

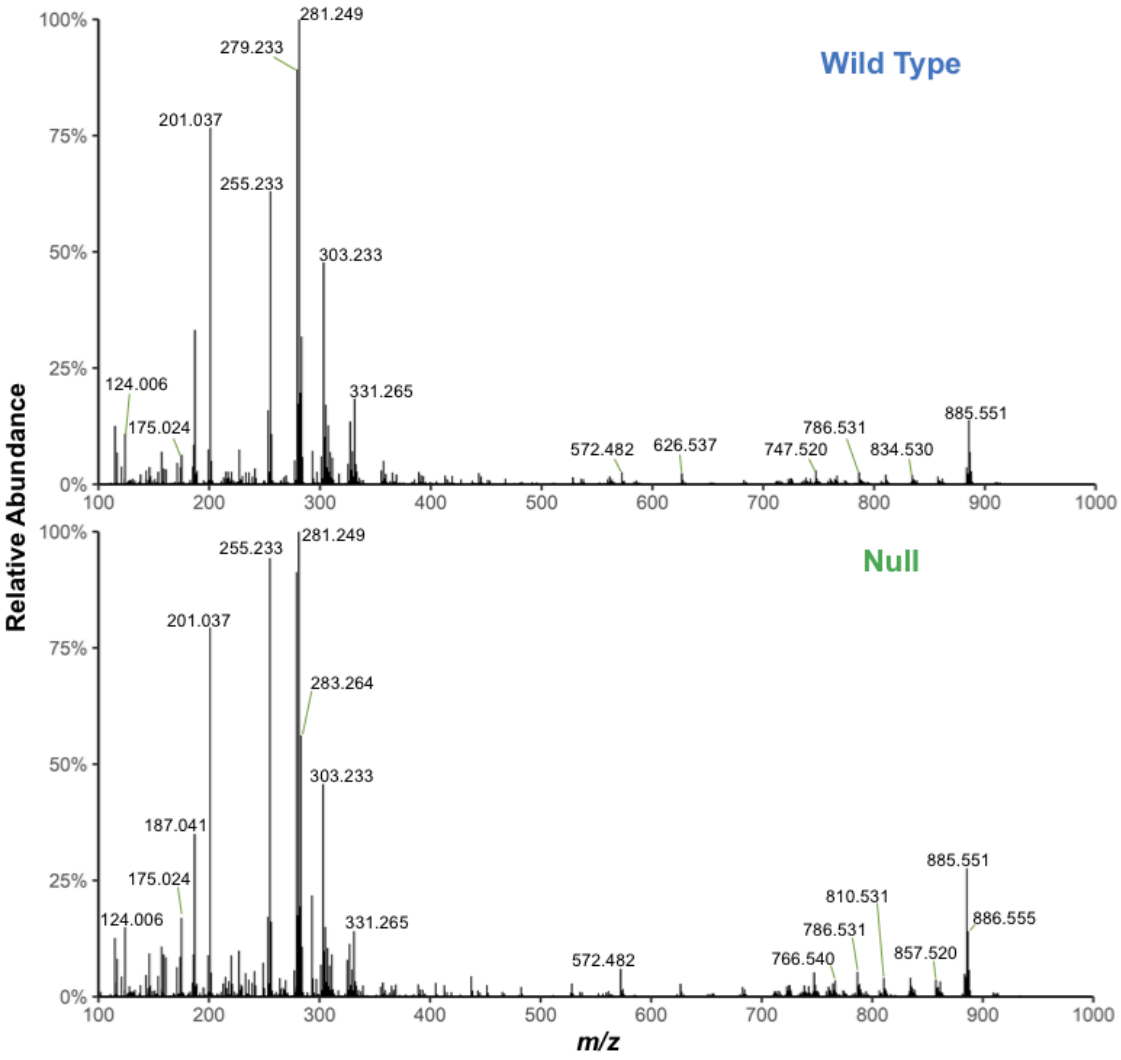

Figure 3.2. **DESI-MS Spectra of Embryonic Cranial Mesenchyme**. Averaged spectra of ions detected in WT (top panel) and *Mthfd1l*-null (bottom panel) embryos with optimized DESI-MS parameters. Mass spectra are averages of 10 pixels extracted from the mesenchyme region of the cranial embryonic tissue.

3.3.2 SAM Analysis

In order to process the plethora of data obtained by DESI-MS, we used the significance analysis of microarrays (SAM) method to select those metabolites with statistically significant increased or decreased abundance in the *Mthfd1l*-null embryo sections. This method is a useful means to compare differences between two large data sets, and was performed using R as previously described (Eberlin et al., 2014). From our data, SAM selected 516 molecular ions that were significantly increased or decreased in the *Mthfd1l*-null embryos compared to WT embryos with a FDR of less than 5%. Of the selected ions, 437 were significantly decreased in the nullizygous embryos, and 79 were significantly increased. Tandem mass spectrometry was used to confirm the identify of some of the biologically relevant selected ions using fragmentation pattern analysis. The majority of metabolites identified by SAM reflected a decrease in abundance in the *Mthfd1l*-null embryos (Figure 3.3).

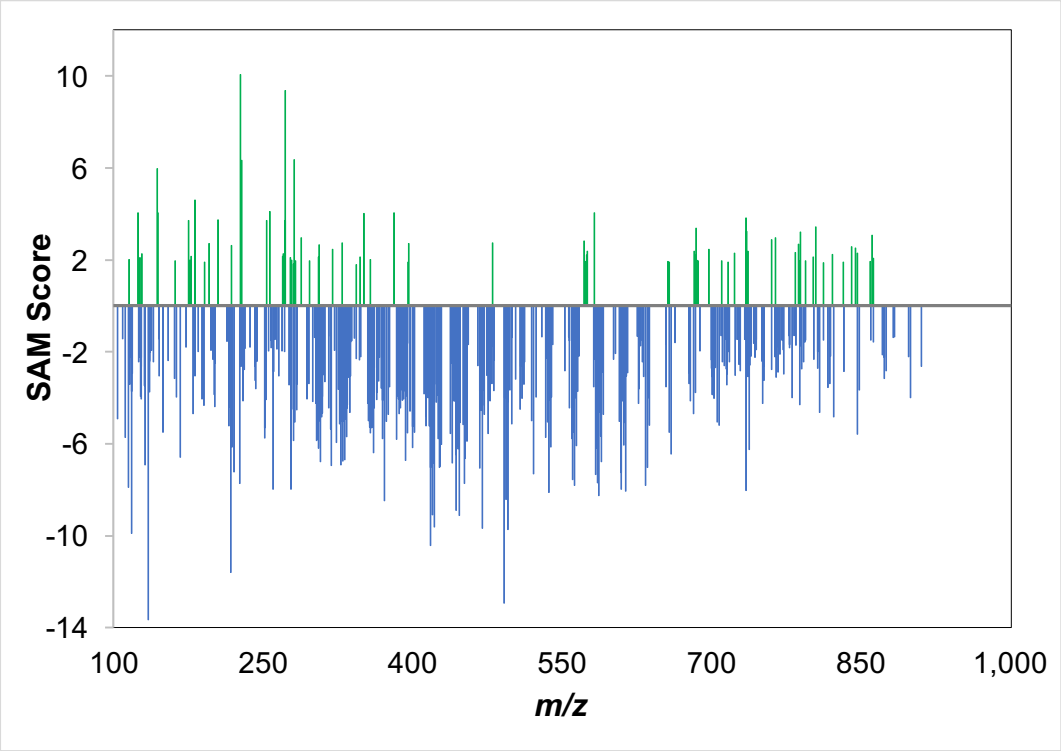

Figure 3.3. **SAM analysis of metabolites of *Mthfd1l*-null and WT embryos using R.** Metabolite ions with significantly different abundance that were selected by SAM analysis are organized by *m/z* values along the x-axis, with the corresponding SAM score along the y-axis. Some of the metabolites selected were increased in the null samples and were given positive SAM scores (green) and some metabolites were decreased in the null samples and assigned negative SAM scores (blue).

Table 3.1: **Metabolite species selected by SAM as increased or decreased in the cranial mesenchyme of *Mthfd1l*$^{e/z}$ embryos (FDR < 5%) identified using DESI-IMS**. SAM scores in the negative range indicate metabolites downregulated in *Mthfd1l*$^{e/z}$ embryos and positive range indicate upregulation in *Mthfd1l*$^{e/z}$ embryos compared to WT.

Tentative attribution	SAM score (d)	Measured *m/z*	Exact *m/z*	Proposed formula	Mass error (ppm)
Uracil	-5.723	111.019	111.020001	$C_4H_4N_2O_2$	9.0
Proline	-7.88	114.055	114.056053	$C_5H_9NO_2$	9.2
Fumarate	2.011	115.002	115.0037	$C_4H_4O_4$	-14.8
Succinate	-3.71	117.018	117.019333	$C_4H_6O_4$	11.4
Taurine	-2.446	124.006	124.007	$C_2H_6NO_3S$	8.1
Pyroglutamate	2.267	128.034	128.0353	$C_5H_7NO_3$	-10.2
Propionylglycine, Hydroxyproline, Acetyl-beta-alanine	-3.475	130.05	130.050967	$C_5H_9NO_3$	7.4
Ureidopropionic acid or Asparagine	-3.49	131.045	131.046216	$C_4H_8N_2O_3$	9.3
Asparagine, Glycyl-glycine, Carbamoyl-sarcosine, Ureido-propionic acid	-1.455	131.045	131.0462	$C_4H_8N_2O_3$	9.2
Adenine	-13.649	134.046	134.047219	$C_5H_5N_5$	9.1
Threonic acid or Erythronic acid	-2.418	135.029	135.0299	$C_4H_8O_5$	6.7
Phenylacetate, Ethenylbenzenediol	-3.751	135.044	135.045153	$C_8H_7O_2$	8.5
Glutamine	-1.447	145.061	145.062	$C_5H_9N_2O_3$	6.9
Hydroxyheptanoic acid	-3.055	145.086	145.087018	$C_7H_{14}O_3$	7.0
Dichlorophenol	-3.16	160.956	160.956644	$C_6H_4Cl_2O$	4.0
Acetyltaurine or Homocysteine sulfinic acid	-6.575	166.017	166.017952	$C_4H_9NO_4S$	5.7
Ascorbic acid	3.705	175.024	175.0248	$C_6H_8O_6$	-4.6
Glucose	-4.693	179.055	179.056112	$C_6H_{12}O_6$	6.2
L-Iditol/Galactitol/ Mannitol/Sorbitol	4.616	181.071	181.0718	$C_6H_{14}O_6$	-4.4
L-methionine	-4.328	190.054	190.054338	$C_7H_{13}NO_3S$	1.8
Citrate/Isocitrate	1.9	191.019	191.0197	$C_6H_8O_7$	-3.7
Gluconic Acid	2.72	195.05	195.051	$C_6H_{12}O_7$	-5.1
Lactate dimer	-4.396	201.037	201.0381	$[C_3H_5O_3]^{2+}Na$	5.5

(Table 3.1 continued)

3-Hydroxynonyl acetate, 3-hydroxyundecanoic acid, or 2-Hydroxyundecanoate	-2.489	201.149	201.1496	$C_{11}H_{22}O_3$	3.0
Undecanedioic acid, Butyl butyryllactate	-5.225	215.128	215.128883	$C_{11}H_{20}O_4$	4.1
Pantothenic acid (vitamin B5)	2.633	218.103	218.1034	$C_9H_{17}NO_5$	-1.8
Trihydroxyquinoline-carboxylic acid	-7.228	220.026	220.025146	$C_{10}H_7NO_5$	-3.9
Phosphatidic acid or citrate	10.061	226.996	226.9964	$C_6H_8O_7Cl$	-1.8
Glycerol 1-propanoate diacetate	-1.846	231.087	231.0874	$C_{10}H_{16}O_6$	1.7
S-Cysteinosuccinic acid	-1.786	236.021	236.0234	$C_7H_{11}NO_6S$	10.2
Uridine	-1.429	243.062	243.0623	$C_9H_{12}N_2O_6$	1.2
Palmitate (FA(16:0))	-1.957	255.233	255.233	$C_{16}H_{31}O_2$	0.0
Ribothymidine	-1.837	257.076	257.0779	$C_{10}H_{14}N_2O_6$	7.4
Deoxyuridine	-1.881	263.044	263.044	$C_9H_{12}N_2O_5Cl$	0.0
FA(16:0(OH))	-2.001	271.228	271.2279	$C_{16}H_{32}O_3$	-0.4
L-Thyronine	3.72	272.094	272.0928	$C_{15}H_{15}NO_4$	4.4
Glutaminylproline	1.975	278.093	278.0913	$C_{10}H_{17}N_3O_4Cl$	6.1
FA(18:1)	-5.043	281.249	281.248604	$C_{18}H_{32}O_2$	-1.4
Glutamylhistidine	-4.537	283.104	283.104794	$C_{11}H_{16}N_4O_5$	2.8
FA(18:3(OH))	-1.31	293.212	293.2122	$C_{18}H_{30}O_3$	0.7
Nonadecanedione	-3.375	295.264	295.264254	$C_{19}H_{36}O_2$	0.9
Hydroxyoctadecanoic acid	-4.169	299.259	299.259169	$C_{18}H_{36}O_3$	0.6
MG(14:0)	-1.374	301.238	301.2384	$C_{17}H_{34}O_4$	1.3
FA(20:4)	-5.851	303.233	303.233	$C_{20}H_{32}O_2$	0.0
FA(20:3)	-6.197	305.249	305.2486	$C_{20}H_{34}O_2$	-1.3
Glutathione (GSH)	2.658	306.076	306.0765	$C_{10}H_{17}N_3O_6S$	-1.6
FA(20:2)	-6.781	307.264	307.2643	$C_{20}H_{36}O_2$	1.0
FA(20:1)	-4.661	309.28	309.2799	$C_{20}H_{38}O_2$	-0.3
FA(20:0)	-3.299	311.296	311.2956	$C_{20}H_{40}O_2$	-1.3
FA(21:5)	-4.438	315.233	315.232954	$C_{21}H_{32}O_2$	-0.1
FA(18:1)	-1.311	317.226	317.2253	$C_{18}H_{34}O_2Cl$	-2.2
FA(20:3(OH))	-1.932	321.244	321.2437	$C_{20}H_{34}O_3$	-0.9
FA(22:6)	-6.921	327.233	327.233	$C_{22}H_{32}O_2$	0.0

(Table 3.1 continued)

MG(16:1)	-1.852	327.254	327.2541	$C_{19}H_{36}O_4$	0.3
FA(22:5)	-6.764	329.249	329.2486	$C_{22}H_{34}O_2$	-1.2
FA(22:4)	-6.69	331.264	331.2643	$C_{22}H_{36}O_2$	0.9
FA(22:3)	-4.467	333.28	333.2799	$C_{22}H_{38}O_2$	-0.3
FA(22:2)	-3.039	335.296	335.2956	$C_{22}H_{40}O_2$	-1.2
MG(14:0)	-3.054	337.215	337.215112	$C_{17}H_{34}O_4Cl$	0.3
FA(22:1)	-1.409	337.311	337.3112	$C_{22}H_{42}O_2$	0.6
2'-Deoxyguanosine 5'-monophosphate, 3'-AMP, Adenosine 2'-phosphate, 2-hydroxy-dAMP, AMP	-2.343	346.056	346.0558	$C_{10}H_{14}N_5O_7P$	-0.6
FA(24:6)	-4.991	355.264	355.2643	$C_{24}H_{36}O_2$	0.8
FA(24:5)	-5.539	357.28	357.2799	$C_{24}H_{38}O_2$	-0.3
FA(24:4)	-5.283	359.296	359.2956	$C_{24}H_{40}O_2$	-1.1
FA(24:3)	-4.452	361.312	361.3112	$C_{24}H_{42}O_2$	-2.2
FA(22:6)	-4.072	363.21	363.2096	$C_{22}H_{32}O_2$	-1.1
MG(16:1)	-2.688	363.231	363.230762	$C_{19}H_{36}O_4Cl$	-0.7
FA(24:2)	-3.761	363.327	363.3269	$C_{24}H_{44}O_2$	-0.3
MG(16:0)	-3.278	365.246	365.246412	$C_{19}H_{38}O_4Cl$	1.1
FA(26:6)	-5.814	383.296	383.2956	$C_{26}H_{40}O_2$	-1.0
FA(26:5)	-4.057	385.311	385.3112	$C_{26}H_{42}O_2$	0.5
MG(18:3)	-2.575	387.231	387.2308	$C_{21}H_{36}O_4Cl$	-0.5
FA(26:4)	-4.45	387.327	387.3269	$C_{26}H_{44}O_2$	-0.3
MG(18:2)	-3.671	389.247	389.246412	$C_{21}H_{38}O_4Cl$	
FA(26:3)	-1.764	389.343	389.3425	$C_{26}H_{46}O_2$	-1.3
FA(26:2)	-1.837	391.359	391.3582	$C_{26}H_{48}O_2$	-2.0
11-Hydroxyeicosatetraenoate glyceryl ester	-3.907	393.262	393.264648	$C_{23}H_{38}O_5$	6.7
FA(28:6)	-3.835	411.327	411.326855	$C_{28}H_{44}O_2$	-0.4
FA(28:5)	-4.775	413.343	413.3425	$C_{28}H_{46}O_2$	-1.2
Palmitoyl glucuronide	-10.428	417.287	417.285778	$C_{22}H_{42}O_7$	-2.9
DG(20:0) or MG(20:0)	-3.411	421.311	421.309012	$C_{23}H_{46}O_4Cl$	-4.7
Hydroxy-trihydroxy-dimethyltetracyclo-heptadecan-ylpentanoic acid	-4.182	423.275	423.275213	$C_{24}H4_0O_6$	0.5
MG(22:6)	-5.541	437.247	437.246412	$C_{25}H_{38}O_4Cl$	-1.3
MG(22:5)	-2.33	439.262	439.2621	$C_{25}H_{40}O_4Cl$	0.2

(Table 3.1 continued)

FA(30:6)	-2.369	439.36	439.3582	$C_{30}H_{48}O_2$	-4.1
FA(30:5)	-4.019	441.375	441.3738	$C_{30}H_{50}O_2$	-2.7
FA(32:6)	-3.685	467.389	467.3895	$C_{32}H_{52}O_2$	1.1
LPG(O-16:0)	-2.555	469.292	469.2936	$C_{22}H_{47}O_8P$	3.4
FA(32:5)	-4.336	469.406	469.4051	$C_{32}H_{54}O_2$	-1.9
PS(P-16:0)	-1.753	480.273	480.2732	$C_{22}H_{44}NO_8P$	0.4
LysoPE(18:0)	2.75	480.311	480.3096	$C_{23}H_{48}NO_7P$	2.9
FA(34:6)	-4.168	495.42	495.4208	$C_{34}H_{56}O_2$	1.6
FA(34:5)	-3.653	497.437	497.4364	$C_{34}H_{58}O_2$	-1.2
Oleic acid + palmitic acid dimer	-4.117	537.49	537.489	$C_{34}H_{65}O_4$	-1.9
Cer(d34:1)	2.836	572.482	572.4815	$C_{34}H_{67}NO_3Cl$	0.9
DG(32:1)	-2.34	601.462	601.4604	$C_{35}H_{66}O_5Cl$	-2.7
DG(32:0)	-2.076	603.477	603.4761	$C_{35}H_{68}O_5Cl$	-1.5
DG(34:2)	-2.038	627.477	627.4761	$C_{37}H_{68}O_5Cl$	-1.4
Cer(d38:1)	-1.531	628.547	628.5441	$C_{38}H_{75}NO_3Cl$	-4.6
Cer(d40:1)	1.941	656.576	656.5754	$C_{40}H_{79}NO_3Cl$	0.9
Cer(d42:2)	2.376	682.592	682.5911	$C_{42}H_{81}NO_3Cl$	1.3
Cer(d42:1)	3.374	684.609	684.6067	$C_{42}H_{83}NO_3Cl$	3.4
PE(32:1)	-1.977	688.492	688.4923	$C_{37}H_{72}NO_8P$	0.4
CL(68:4)	-2.367	699.478	699.4788	$C_{77}H_{142}O_{17}P_2$	1.1
PE(O-34:2) or PE(P-34:2)	-3.079	700.528	700.5287	$C_{39}H_{76}NO_7P$	1.0
CL(68:0)	-2.675	703.509	703.5101	$C_{77}H_{150}O_{17}P_2$	1.6
PE 34:4	1.949	710.472	710.4766	$C_{39}H_{70}NO_8P$	-6.5
CL(70:4)	-1.45	713.495	713.4945	$C_{79}H_{146}O_{17}P_2$	-0.7
PE(34:1)	1.91	716.523	716.5236	$C_{39}H_{76}NO_8P$	-0.8
PE(34:1)	-1.988	716.525	716.5236	$C_{39}H_{76}NO_8P$	-2.0
PE-Cer(d36:1)	-3.028	723.518	723.5213	$C_{38}H_{77}N_2O_6P$	4.6
CL(72:6)	-1.469	725.495	725.4945	$C_{81}H_{146}O_{17}P_2$	-0.7
CL(72:4)	-2.552	727.508	727.5101	$C_{81}H_{150}O_{17}P_2$	2.9
HexCer(d34:1)	3.823	734.534	734.5343	$C_{40}H_{77}NO_8Cl$	-0.4
CL 74:8	-1.595	737.496	737.4945	$C_{83}H_{146}O_{17}P_2$	-2.0
PS(P-34:2) or PS(O-34:3)	-1.629	742.505	742.5029	$C_{40}H_{74}NO_9P$	-2.8
PS(O-34:2) or PS(P-34:1)	-1.92	744.52	744.5185	$C_{40}H_{76}NO_9P$	-2.0
CL(76:9)	-2.403	750.507	750.5023	$C_{85}H_{148}O_{17}P_2$	-6.3
PS(34:1)	2.887	760.514	760.5134	$C_{40}H_{76}NO_{10}P$	0.8

(Table 3.1 continued)

PS(34:1)	-2.779	760.515	760.5134	$C_{40}H_{76}NO_{10}P$	-2.1
PE(38:5)	2.95	764.524	764.5236	$C_{43}H_{76}NO_8P$	0.5
PE(38:5)	-3.097	764.525	764.5236	$C_{43}H_{76}NO_8P$	-1.8
PS(O-36:5) or PS(P-36:4)	-2.89	766.505	766.5029	$C_{42}H_{74}NO_9P$	-2.7
PS(O-36:3) or PS(P-36:2)	-1.487	770.536	770.5342	$C_{42}H_{78}NO_9P$	-2.3
PE(P-40:7)	-2.973	772.533	772.5287	$C_{45}H_{76}NO_7P$	-5.6
PE(39:5)	-1.826	778.539	778.5392	$C_{44}H_{78}NO_8P$	0.3
PE(O-40:5) or PE(P-40:4)	-1.684	778.574	778.5756	$C_{45}H_{82}NO_7P$	2.1
PE(38:4(OH))	-1.293	782.537	782.5342	$C_{43}H_{78}NO_9P$	-3.6
PS(36:3)	2.314	784.514	784.5134	$C_{42}H_{76}NO_{10}P$	0.8
PS(36:3)	-1.725	784.515	784.5134	$C_{42}H_{76}NO_{10}P$	-2.0
PS(36:1)	-1.525	788.54	788.5447	$C_{42}H_{80}NO_{10}P$	6.0
PS(36:1)	1.96	788.547	788.5447	$C_{42}H_{80}NO_{10}P$	2.9
PE(40:6)	-2.732	790.541	790.5392	$C_{45}H_{78}NO_8P$	-2.3
PE(40:5)	-2.448	792.556	792.5549	$C_{45}H_{80}NO_8P$	-1.4
PS(P-38:4) or PS(O-38:5)	-1.491	794.536	794.5342	$C_{44}H_{78}NO_9P$	-2.3
PC(34:1) or PE(37:1)	1.965	794.548	794.5472	$C_{42}H_{82}NO_8PCl$	1.0
PS(37:1)	2.124	802.557	802.5604	$C_{43}H_{82}NO_{10}P$	-4.2
PE(P-42:6)	-2.323	802.572	802.5756	$C_{47}H_{82}NO_7P$	4.5
PE(40:6(OH))	-2.713	806.535	806.5342	$C_{45}H_{78}NO_9P$	-1.0
PS(38:3)	-1.489	812.545	812.5447	$C_{44}H_{80}NO_{10}P$	-0.4
PS(38:3)	1.881	812.546	812.5447	$C_{44}H_{80}NO_{10}P$	1.6
PI-Cer(d34:0)	-3.551	816.521	816.5163	$C_{40}H_{80}NO_{11}P$	-5.8
PS(P-40:6)	-3.376	818.538	818.5342	$C_{46}H_{78}NO_9P$	-4.6
PG(40:7)	-2.192	819.518	819.5182	$C_{46}H_{77}O_{10}P$	0.2
PS(40:7)	-2.853	832.515	832.5134	$C_{46}H_{76}NO_{10}P$	-1.9
PC(38:6) or PE(41:6)	2.579	840.53	840.5316	$C_{46}H_{80}NO_8PCl$	-1.9
PC(38:4) or PE(41:4)	2.517	844.56	844.5629	$C_{46}H_{84}NO_8PCl$	-3.4
PI(36:3)	-1.486	859.534	859.5342	$C_{45}H_{81}O_{13}P$	0.2
PI(36:3)	1.939	859.534	859.5342	$C_{45}H_{81}O_{13}P$	-0.2
PI(36:2)	3.072	861.55	861.5499	$C_{45}H_{83}O_{13}P$	0.1
PI(38:5)	-1.345	883.536	883.5342	$C_{48}H_{81}O_{10}P$	-2.0

3.3.3 DESI-IMS Ion Maps

The strength of the IMS technology is the ability to evaluate the spatial distribution of metabolites in tissue. This perspective is particularly informative when examining neural tube closure, where cellular gene and metabolite profiles are rapidly changing in order for an early organism to expand and meet the spatiotemporal requirements of forming a neural plate and then folding into a tube (Smith and Schoenwolf, 1997). Because we observed defects in the cranial mesenchyme of *Mthfd1l*-null embryos, the metabolomics of the mesenchymal tissue was particularly of interest, and IMS allowed not only for extraction of data corresponding to that region, but also chemical mapping of the tissue (Figure 3.4).

Based on the metabolite map data, several qualitative observations can be made. The metabolites analyzed in these maps appear most concentrated in the mesenchyme and central regions of the cranial tissue. It seems that very little adenine or uracil was detected in the *Mthfd1l*-null samples, as well as a reduction in all of the essential amino acids that were measured by DESI-MS. L-methionine is lower in nullizygous cranial mesenchyme, which was expected due to its role downstream of mitochondrial formate in one-carbon metabolism. Based on ion maps of lactate, glucose, fumarate, citrate, and succinate, it seems that energy metabolism is dysregulated in the *Mthfd1l*-null samples compared to WT. Lastly, several ceramides were detected that SAM identified as significantly different, all of which were increased in abundance in *Mthfd1l*-null embryos. It is also important to note that succinate and citrate ion maps have significant amounts of background resulting from very low signal levels. These background values were not taken into account when evaluating the differences in metabolite abundance for each sample.

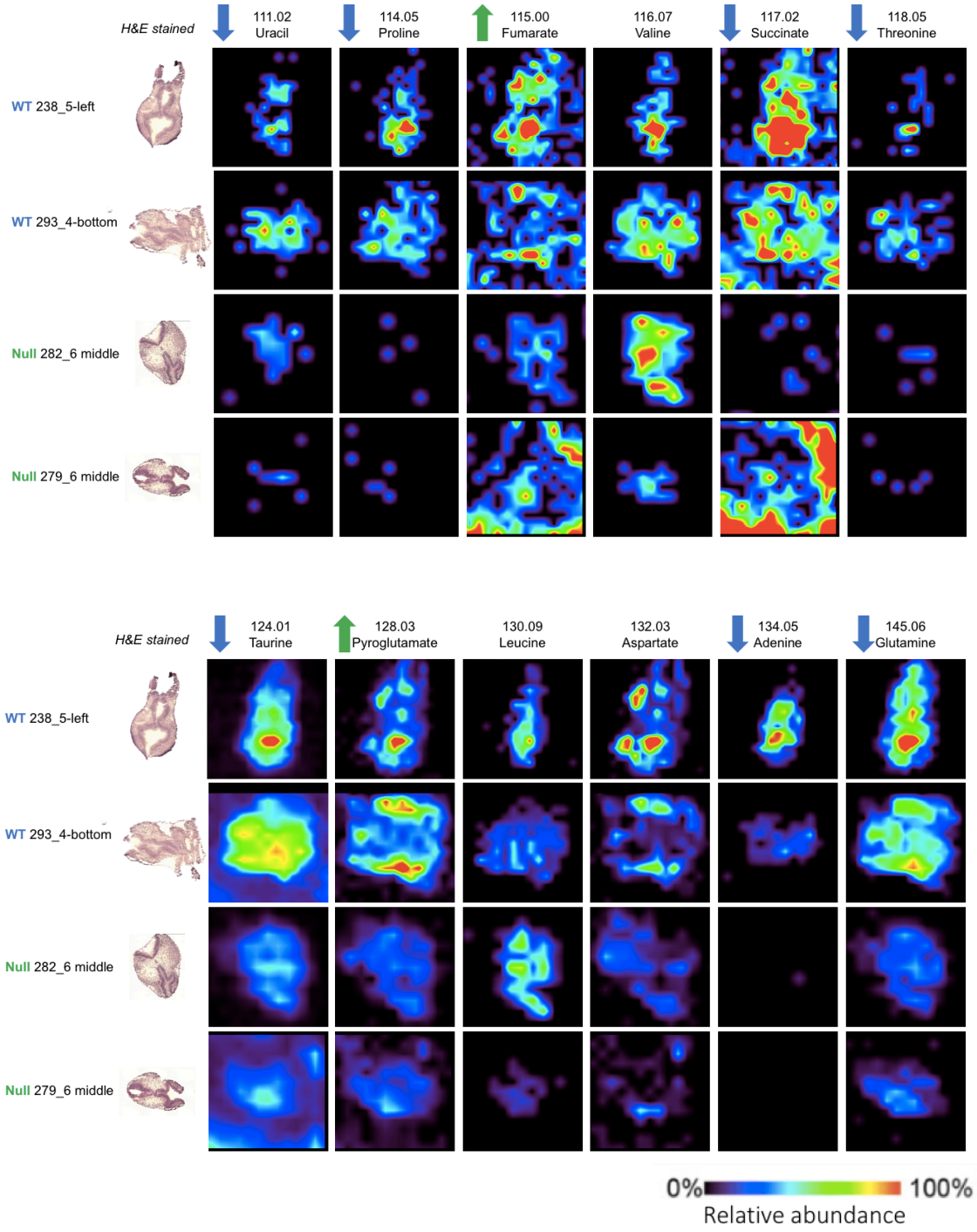

(Figure 3.4, continued on next page)

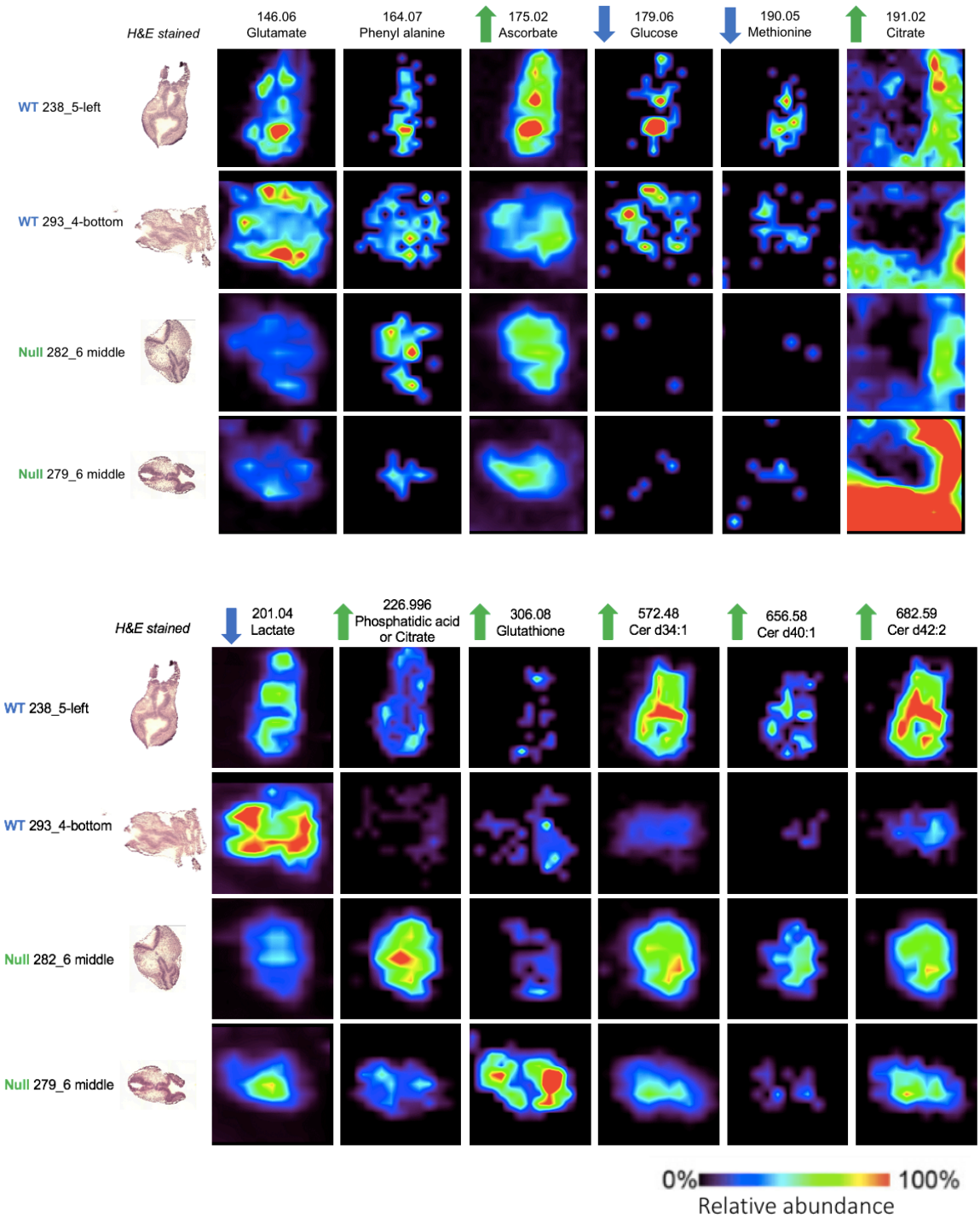

Figure 3.4. **DESI-MS ion images of transverse sections of cranial embryonic tissue of *Mthfd1l*-null and WT embryos**. Metabolites are organized from smallest *m/z* to largest, *m/z* value is displayed above each metabolite. Green arrows indicate metabolites selected by SAM analysis that are up-regulated in the mesenchyme of

null samples compared to WT, and blue arrows indicate metabolites selected by SAM analysis that are down-regulated in the mesenchyme of null samples compared to WT. Lack of an arrow indicates that this metabolite was not selected by SAM analysis as being significantly different between the mesenchyme-containing regions of both groups (WT and null). Two representative embryo samples (rows) that display the range of metabolite concentrations observed within each group are shown for each metabolite (columns). H&E stains of tissue sectioned used in the DESI-IMS analysis displayed to the left of the visual spectra for each sample. Relative abundance is shown from 0 to 100%, from violet to red, respectively.

Figure 3.4: continued.

3.3.4 PCA Analysis

The hundreds of metabolites detected by DESI-MS were analyzed by PCA, and a clear separation between WT and *Mthfd1l*-null embryos was observed along component 3 (Figure 3.5, A). When only metabolite data from the mesenchyme region was analyzed, the separation along component 1 was made more apparent as well (Figure 3.5, B). This method served to reveal trends between the two groups across all of the data obtained by DESI-MS, providing a clear picture of the grouping of data across different batches. In Figure 3.5 A, the batch effect was observed across component 1, when samples had lower PC1 values from an earlier run from both WT and *Mthfd1l*-null groups, and higher PC1 values from a later run. This variation did not influence the observed separation along PC3, however.

A.

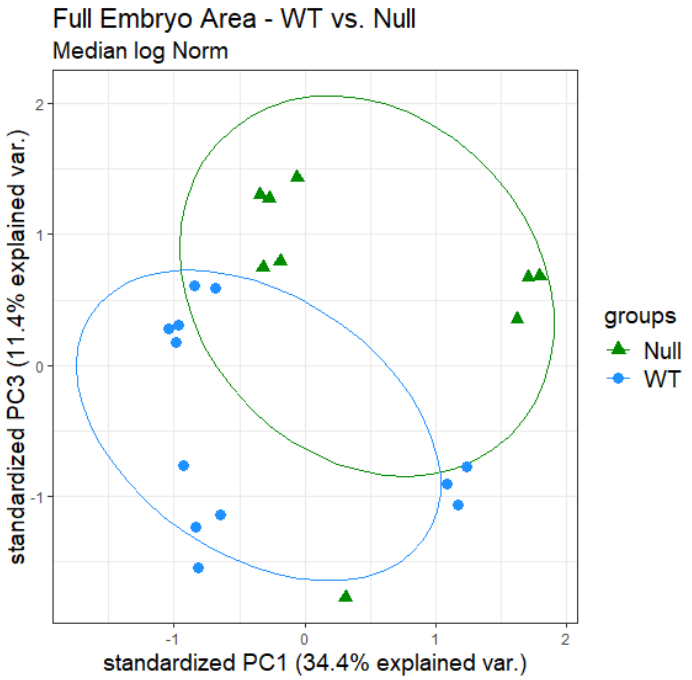

B.

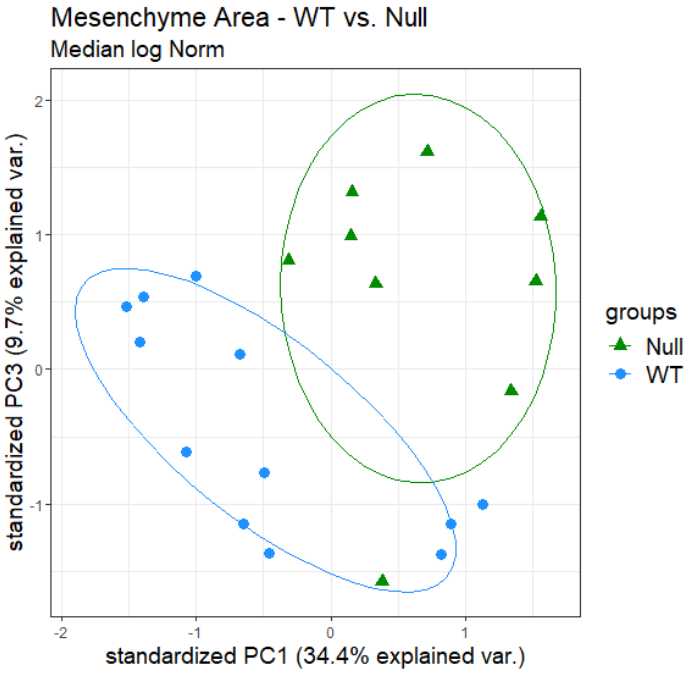

Figure 3.5. **PCA analysis of metabolites of *Mthfd1l*-null and WT embryos using median log normalization**. Each data point is an embryo sample; nulls are

represented in green, and WT samples are in blue. Principle components (PCs) 1 and 3 were considered in analyzing the data. PCA analysis was performed using R. (A) The PCA of spectra from the total embryo analyzed by IMS along components 1 and 3. (B) The PCA of the spectra from mesenchyme along components 1 and 3.

Figure 3.5: continued

3.3.5 T-test of Metabolites

Differences in the relative abundance of metabolites in WT and *Mthfd1l*-null samples were analyzed by t-test, and p-values were adjusted for the false discovery rate (FDR) (Benjamini and Hochberg, 1995). The detected metabolites relevant to energy metabolism and amino acid metabolism compared by t-test are shown in Figure 3.6. Glucose, proline, uracil, and adenine levels in the *Mthfd1l*-null embryonic mesenchyme were significantly decreased. Ascorbic acid, lactate, glutamine, glutamate, and taurine did not vary much between groups nor across samples within each group. For citrate, fumarate, succinate, AMP, glutathione, and threonine, the means of the two groups appeared significantly different, yet SD values were too great for these metabolite differences to be statistically significant.

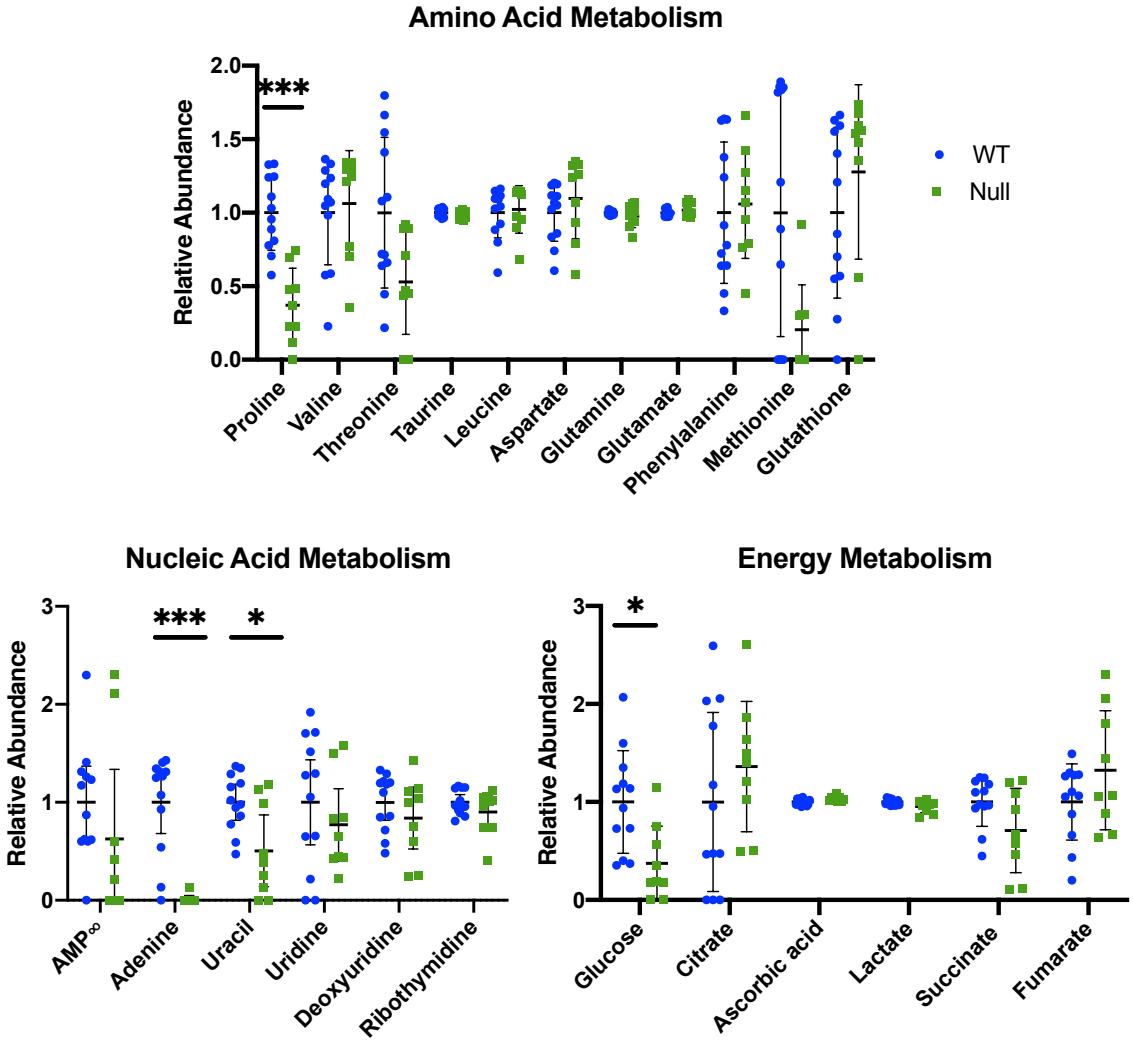

Figure 3.6. **Metabolomics analysis of cranial mesenchyme of *Mthfd1l*$^{-/-}$ embryos.** Abundance of metabolites related to amino acid metabolism (top panel), nucleic acid metabolism (bottom left), and energy metabolism (bottom right) in *Mthfd1l*$^{-/-}$ embryos (green) relative to *Mthfd1l*$^{+/+}$ embryos (blue). Data are shown with mean ± SD. *, *** indicates $q < 0.05$, and $q < 0.0005$, respectively. Calculated in Prism 8.

∞Tentative attribution includes any of the following AMP species: 2'-Deoxyguanosine 5'-monophosphate, 3'-AMP, Adenosine 2'-phosphate, 2-hydroxy-dAMP, or AMP

3.4 DISCUSSION

Removal of a key THF-interconverting enzyme from the one-carbon pathway is destined to disrupt metabolic homeostasis, and through evaluation of this disruption we come closer to understanding one-carbon metabolism. In particular, gene deletion during early development reflects even greater metabolic consequences due to the requirement of 1C units to meet the demands of a rapidly growing and changing cell population. The DESI-IMS platform used in this chapter provided high sensitivity in profiling molecules at specific locations in the early developing E8.75-9.5 mouse embryos, while still allowing for broad metabolite coverage. Using this non-targeted metabolomics approach, we were able to identify disruptions in amino acid, nucleic acid, and energy metabolism.

Interestingly, the abundance of nearly all detected amino acids was decreased in the embryos lacking *Mthfd1l*. Based on IMS map images (Figure 3.4), proline, threonine, and glutamine all appeared to be diminished in the mesenchyme of the *Mthfd1l*-null samples. Further statistical analysis and FDR correction of all samples evaluated in this study reflected that only proline is significantly decreased in the nullizygous embryos (Figure 3.6). Maternal proline supplementation has been shown to increase growth and polyamine availability in porcine embryos (Wu et al., 2008). A decreased supply of amino acids could have deleterious effects on protein synthesis in the developing embryo, especially during neural tube closure, when rapid growth and cell division are occurring. These findings are consistent with whole embryo LC-MS metabolomics done previously by our lab, although the data from the whole embryo lysates reflected significant increases in aspartate and taurine in the null samples (Bryant et al., 2018). This discrepancy is likely a result of the difference in biosynthetic demands across tissue types. A decrease in amino acid abundance was also reported in the NTD-prone *Lrp6*$^{-/-}$ mutant mouse embryo (Hansler et al., 2014). The impact of *Mthfd1l* deletion on a wider

range of amino acids than just serine and glycine is intriguing, and further studies on how one-carbon metabolism impacts amino acid synthesis should be considered. Furthermore, maternal proline supplementation in our mouse model, possibly in combination with formate, may partially rescue the growth defects characteristic of *Mthfd1l*-null embryos.

Compared to WT embryos, energy metabolism was disrupted in the mesenchyme of embryos lacking *Mthfd1l.* Glucose was significantly diminished (Figure 3.6), and the IMS maps (Figure 3.4) indicate very little to no signal in the mesenchyme. Although they do not reach statistical significance following FDR correction, both citrate and fumarate are increased slightly in the *Mthfd1l*-null embryos, suggesting an increase in flux through the tricarboxylic acid (TCA) cycle. Because healthy E9.5 embryos exhibit increased contributions from glycolysis during chorioallantoic branching (Miyazawa et al., 2017), deletion of *Mthfd1l* may reduce lactate production and shift energy metabolism towards the more efficient TCA cycle. This is supported by earlier MS studies indicating that *Mthfd1l*-null embryos have decreased lactate abundance (Bryant et al., 2018). In my study, lactate was identified by SAM analysis as being significantly decreased in the null samples (Figure 3.3, 3.4). Pyruvate was not detected by DESI-IMS, likely due to its small size, but it would be interesting to observe pyruvate distribution in cranial mesenchyme tissue using MALDI-IMS, in order to more clearly evaluate rewiring of glucose metabolism that may occur in embryos lacking *Mthfd1l.* Whereas the best resolution offered by DESI is approximately 100µm, MALDI is capable of reaching 10µm resolution (Touboul and Brunelle, 2016). MALDI would also be able to detect smaller metabolites involved in one-carbon metabolism such as formate, which would be very informative in our understanding of how formate is processed in the developing *Mthfd1l*-null mouse embryo.

Another reason formate ($m/z = 45$) was not detected in this study is a result of the m/z range readable by the Orbitrap mass analyzer, which can only detect $m/z \geq 50$. In future studies, a mass analyzer with a lower m/z range should be utilized so that formate might be detected and analyzed. A further challenge with formate detection arises from the presence of CO_2 in the sample, as the mass is so similar to formate (44g/mol and 45g/mol, respectively) that the two signals overlap.

The vast majority of 1C units used to synthesize purines, thymidylate, and AdoMet in the cytoplasm are first oxidized in the mitochondria (Yoshida and Kikuchi, 1971; Barlowe and Appling, 1988). Without Mthfd1l, these oxidized 1C units won't be released from the mitochondria as formate, and intercellular pools of purines, thymidylate, and AdoMet should decrease. Our findings in this study confirmed this hypothesis. Of nucleotide species, DESI-IMS detected adenine and AMP, as well as a number of thymidylate derivatives, including uridine, uracil, deoxyuridine, and ribothymidine. Every one of these metabolies were decreased in the mesenchyme of *Mthfd1l*-null embryos (Figure 3.4, 3.6). It is likely that reduced flux of formate into the cytoplasm inhibits normal purine synthesis, and any free intracellular adenine (or guanine) will likely be used to synthesize DNA. Cytoplasmic 1C units that are not used for purine or thymidylate synthesis are reduced to 5-methyl THF for the synthesis of methionine, which was also reduced in embryos lacking *Mthfd1l.*

Although SAM analysis identified 516 molecular ions that were significantly different between the two groups, we were unable to assign all of the ions selected because there were no potential matches in the Human Metabolome Database (HMDB) or Lipidmaps database with a mass error of less than 10ppm. Of those that we were able to assign, we further processed with MS/MS in order to confirm by fragmentation analysis. Unfortunately, due to the small area of these E8.75-9.5 embryo samples, it was

difficult to isolate all of the identified molecules using DESI-MS/MS. In the future, we propose running a lipid extraction prior to MS/MS in order to more competently isolate ions.

The number of ions selected by SAM analysis as significantly increased or decreased in null samples suggests that deletion of *Mthfd1l* leads to an overall reduction in abundance of metabolites. Of 516 significantly different ions, 437 were decreased in *Mthfd1l*-null embryos, leaving only 79 metabolites that increased in abundance compared to WT. It is likely that the absence of mitochondrially-derived formate slows flux through the cytoplasmic 1C biosynthetic reactions of purine and thymidylate synthesis, as well as methionine synthesis, which remethylates AdoHcy to produce AdoMet in the methyl cycle. Further analysis of AICAR, FAICAR, fluorouracil, phosphoribosyl pyrophosphate, and other intermediates involved in purine and thymidylate synthesis using MALDI-MS and/or NMR methods is needed to elucidate the mechanism at work when *Mthfd1l* is deleted.

CHAPTER 4: CHARACTERIZATION OF EMBRYONIC MICE LACKING MITOCHONDRIAL FORMATE-PRODUCING ENZYMES MTHFD1L AND ALDH1L2

4.1 INTRODUCTION

Formate is a smaller and more mobile carrier of 1C units than THF-bound metabolites, as evidenced by the greater concentration of formate in blood than folates. Approximately 50% of the formate found in serum is produced via a folate-dependent mechanism in the mitochondria, as it is the final product of the 10-formyl-THF synthetase reaction catalyzed by MTHFD1L (Meiser et al., 2016). Formate is also produced via folate-independent mechanisms in the cytoplasm, from the catabolism of tryptophan and choline, the synthesis of cholesterol and sterol, the oxidation of formaldehyde, peroxisomal α-oxidation of phytanic acid, and lastly in the endoplasmic reticulum, by a number of different cytochrome-P450-catalyzed demethylation reactions (Figure 4.1, reviewed in Brosnan and Brosnan, 2016). The endogenous pool of formate in an organism is further increased by contributions from the intestinal microbiome. In the gut, formate (along with acetyl CoA) is a fermentation product of anaerobic bacteria, and is found in milimolar concentrations in the intestinal lumen of mice (Hughes et al., 2017).

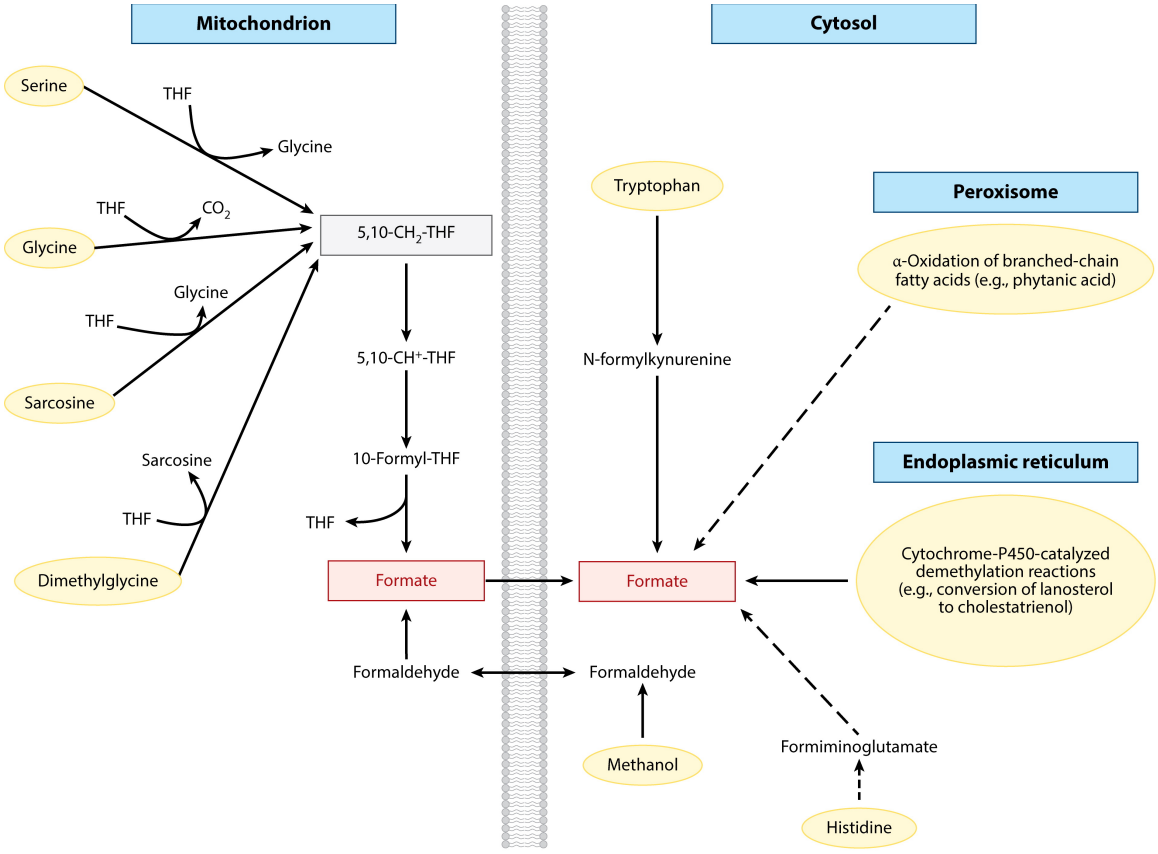

Brosnan ME, Brosnan JT. 2016.
Annu. Rev. Nutr. 36:369–88

Figure 4.1. **Intercellular sources of formate**. Figure from (Brosnan and Brosnan, 2016).

As mentioned previously, formate supplementation during pregnancy has been proven to reduce the incidence of NTDs caused by defects in 1C metabolism in mice (Momb et al., 2013; Narisawa et al., 2012; Pai et al., 2015). The requirement for mitochondrially derived formate during embryonic development was demonstrated by our lab's *Mthfd1l*-null mouse model, as formate supplementation via maternal drinking water was not able to completely prevent birth defects (Momb et al., 2013). Based on what is currently known, Mthfd1l is the sole enzyme responsible for formate production in the mitochondria. For this reason, it was unexpected that mitochondria isolated from

Mthfd1l-null embryos continue to produce formate—which they do at approximately 1/3 the amount produced by mitochondria from WT embryos (Bryant et al., 2018). The tracing experiment that identified this residual formate production measured the conversion of L-[3-^{14}C]-serine to [^{14}C]-formate, thereby suggesting the existence of an additional formate-producing mitochondrial pathway from the 3-carbon of serine. It is important to note that the amount of formate produced by *Mthfd1l*-null mitochondria *in vivo* is still insufficient to support embryonic development, as demonstrated by the 100% penetrance of birth defects and reduction in methionine production in *Mthfd1l*-null embryos (Momb et al., 2013; Bryant et al., 2018).

This chapter is focused on better understanding additional sources of formate resulting from serine oxidation in the mitochondria. As described in Chapter 1.4, Aldh1l2 is the mitochondrial 10-formyl-THF dehydrogenase that catalyzes the formation of CO_2 and THF from 10-formyl-THF in an $NADP^+$ dependent manner. Because Aldh1l2 has been shown to produce formate *in vitro*, it is possible that this enzyme is responsible for mitochondrial 10-formyl-THF dehydrogenase activity as well (Krupenko et al., 2010; Strickland et al., 2011a). As confirmed with immunoblotting, Aldh1l2 was shown to be highly expressed in both WT and *Mthfd1l*-null mitochondria that continue to produce formate *in organello* (Bryant et al., 2018). Because the specific metabolic processes underlying NTDs are not understood, the generation of a mouse line that lacks the mitochondrial 1C pathway enzymes *Aldh1l2* and *Mthfd1l* will help elucidate the source and role of mitochondrially produced formate during development.

4.2 MATERIALS AND METHODS

4.2.1 *Mthfd1l*$^{tz/tz}$/*Aldh1l2*$^{-/-}$ Mouse Model Design

This study used protocols approved by the Institutional Animal Care and Use Committee of the University of Texas at Austin, and care of animals was performed in accordance with the guidelines approved by the National Institutes of Health for the Care and Use of Laboratory Animals. All mice were maintained on a C57BL/6 genetic background, exposed to a 12-hour light/dark cycle, and fed commercially available laboratory chow (LabDiet 5K67).

Aldh1l2$^{-/-}$ mice were a generous gift from the Krupenko lab (University of North Carolina Nutrition Research Institute), and were produced at the Medical University of South Carolina (MUSC) Transgenic Models Facility using embryonic stem cells with a targeted knockout of *Aldh1l2* purchased from the Knockout Mouse Program (KOMP) resource. These ESCs were generated by insertion of the target sequence by homologous recombination, and injected into Albino B6 blastocysts. These embryos were then injected into pseudo-pregnant mice. Male chimeras born from injected blastocysts were bred to Albino B6 females to obtain heterozygous *Aldh1l2*$^{+/-}$ mice with one targeted allele (germline transmission). These heterozygous mice were interbred to produce the *Aldh1l2*$^{-/-}$ mouse line (Krupenko, unpublished).

Heterozygous *Mthfd1l*$^{tz/+}$ mice were generated as explained in Chapter 2.2.1. *Mthfd1l*$^{tz/+}$ and *Aldh1l2*$^{-/-}$ mice were crossed to yield *Mthfd1l*$^{tz/+}$ / *Aldh1l2*$^{+/-}$ mice, which were interbred to produce the *Mthfd1l*$^{tz/+}$ / *Aldh1l2*$^{-/-}$ mouse line that was bred to generate

the desired double knock-out *Mthfd1l*$^{gt/z}$ / *Aldh1l2*$^{-/-}$ embryo model.

4.2.2 *Mthfd1l*$^{gt/z}$/*Aldh1l2*$^{-/-}$ Mouse Model Genotyping

Mice were genotyped for *Mthfd1l* as described in Chapter 2.2.2. For *Aldh1l2*, the same genotyping protocol was utilized (Stratman et al., 2003). A set of primers was used to amplify a 338 bp region of DNA in the wild type allele. In the forward direction, 5'-AATTGGTGGTTCTCTCAAGTCTG was used, and in the reverse, 5'-GCACCCATAAAGGGGCTCAAG was used. In the mutant allele, an amplicon 598 bp was produced from forward primer 5'-CACACCTCCCCCTGAACCTGAAA and reverse primer 5'-GACATATACTGACCTCTGAGGGTGGC.

4.2.3 Embryo Collection

Embryos were collected as outlined in Chapter 2.2.3.

4.2.4 Histology

Histology was performed as outlined in Chapter 2.2.4.

4.2.5 Alcian Blue Staining

Alcian blue staining was performed as outlined in Chapter 2.2.6.

4.2.6 Isolation of Mitochondria from Adult Mouse Liver

The morning of the mitochondrial isolation, 3 month old mice were euthanized by CO_2 asphyxiation and livers were removed and rinsed in ice cold 1X PBS. For each mouse 0.5 g of liver was added to 5mL homogenization medium (0.3 M sucrose, 1 mM EGTA, 5 mM MOPS, 5 mM KH2PO4, 0.1% BSA (pH 7.4)), and minced with scissors.

Cells were disrupted using a glass-teflon Thomas homogenizer attached to a drill press operating at 87-rpm. For each sample, 10 up-and-down strokes were used to homogenize the cells in the mixture. The homogenate was diluted to 18mL, and centrifuged for 15 minutes at 660 X g in a Sorval RC5C SS-34 rotor at 4°C to pellet out cell debris. The supernatant was carefully removed and spun at 7,700 X g for 15 minutes to pellet the mitochondria. For samples to be analyzed by Western blot, the pellet was resuspended in 1mL 0.1% NP-40 buffer (0.1% Nonidet P-40, 100 mM Tris, pH 7.5, 150 mM NaCl) that contained a Pierce protease inhibitor tablet (ThermoFisher). (Pike et al., 2010; Bryant et al., 2018)

4.2.7 Bradford Assay

Bradford Dye Reagent (Bio-Rad) absorbance was measured at 595 nm, a standard curve was created from a range of BSA concentrations (0, 5, 10, 20 μg/L) that was used to determine concentration of mitochondrial protein extracts.

4.2.8 Western Blot Analysis

Mitochondrial extracts in 0.1% NP-40 buffer were standardized using concentration levels determined by the Bradford Assay. For each sample, mitochondrial lysate was added to SDS-PAGE loading buffer and boiled at 90ºC before analysis by SDS-PAGE. Each well contained 200 μg of mitochondrial protein (Pike et al., 2010).

4.2.9 Maternal Supplementation with Calcium Formate

Formate supplementation was achieved by the addition of calcium formate to the drinking water of *Mthfd1l*$^{e/+}$ mating pairs. Concentration of calcium formate was 0.1 M to deliver 2,500 mg formate·kg^{-1}·d^{-1}, based on an average water intake of 5 mL per day for a

25 g C57BL/6 mouse (Momb et al., 2013).

4.2.10 Fertility Analysis in Male Mice

Testis, vas deferens and epididymis were dissected from both *Mthfd1l*$^{+/+}$/ *Aldh1l2*$^{+/+}$ (WT) and *Mthfd1l*$^{tz/+}$/ *Aldh1l2*$^{-/-}$ males. Testis were imaged using a Leica M80 stereomicroscope and Leica IC80 camera. Testis, vas deferens and epididymis were minced and placed in HTF medium for 5 minutes at 55ºC to release sperm, which were also imaged with the Leica stereomicroscope and camera.

4.3 RESULTS

4.3.1 Phenotype Analysis of *Mthfd1l* and *Aldh1l2* Mutant Mice

4.3.1.1 Breeding Phenotype

Mthfd1l$^{tz/+}$ and *Aldh1l2*$^{-/-}$ mouse lines were crossed and bred for three generations in order to generate *Mthfd1l*$^{tz/tz}$/ *Aldh1l2*$^{-/-}$ embryos for analysis (Figure 4.2). Timed matings were set up between *Mthfd1l*$^{tz/+}$/ *Aldh1l2*$^{-/-}$ mice in order to collect embryos at E10.5 for embryonic phenotype analysis, however only 5 of 32 (15.6%) females that were plugged were actually pregnant at E10.5 (Table 4.1). In comparison, 35 of 40 (87.5%) *Mthfd1l*$^{tz/+}$/ *Aldh1l2*$^{+/+}$ plugged female mice were pregnant at E10.5. Litter sizes of *Mthfd1l*$^{tz/+}$/ *Aldh1l2*$^{-/-}$ mice were comparable in size to those born to *Mthfd1l*$^{tz/+}$/ *Aldh1l2*$^{+/+}$ mice.

To examine the reduced fertility phenotype of *Mthfd1l*$^{tz/+}$/ *Aldh1l2*$^{-/-}$ mice, I mated *Mthfd1l*$^{tz/+}$/ *Aldh1l2*$^{-/-}$ males with *Mthfd1l*$^{+/+}$/ *Aldh1l2*$^{+/+}$ (WT) females, as well as WT males with *Mthfd1l*$^{tz/+}$/ *Aldh1l2*$^{-/-}$ females. Over 10 months, these mating pairs failed to become pregnant.

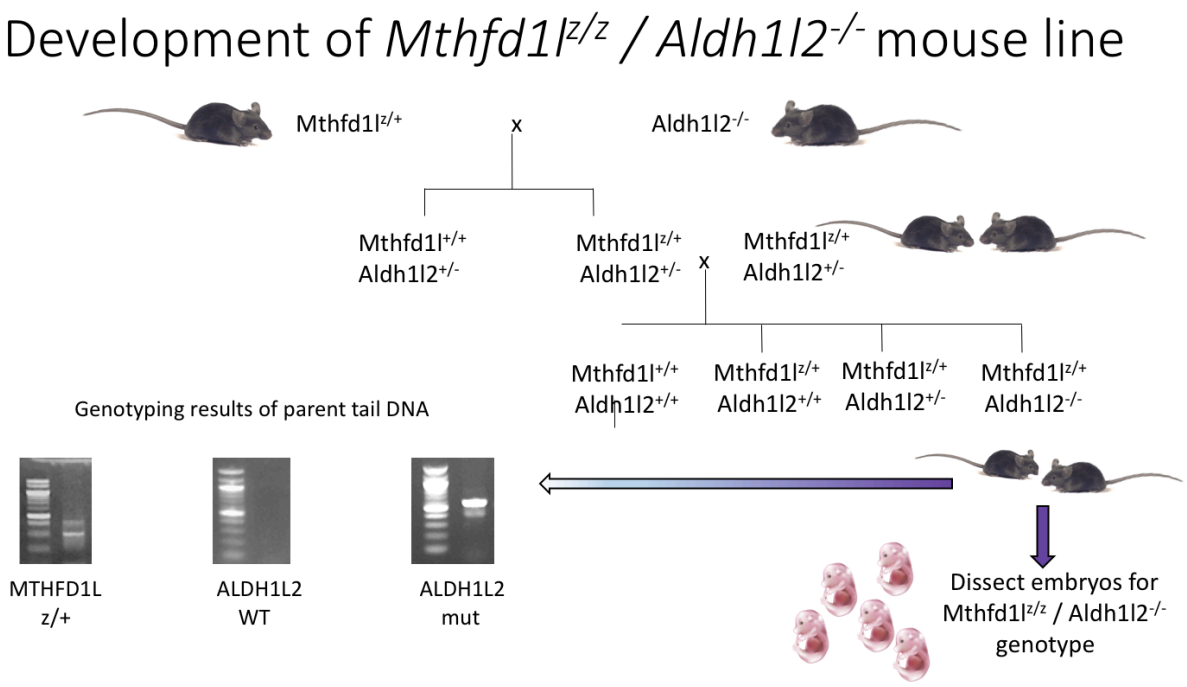

Figure 4.2. **Breeding scheme of *Mthfd1l*$^{z/+}$ x *Aldh1l2*$^{-/-}$ mice to generate *Mthfd1l*$^{z/z}$ / *Aldh1l2*$^{-/-}$ compound KO mouse line**. Genotyping of both gene constructs is shown to the lower left. Embryos were to be analyzed in this study because the compound Mthfd1l$^{z/z}$ / Aldh1l2$^{-/-}$ genotype is incompatible with life.

Table 4.1: **Litter size and fertility of Mthfd1l$^{z/+}$/ Aldh1l2$^{-/-}$ breeding pairs**. All pregnant females were dissected at E10.5 for embryo analysis. Fertility rate is calculated as number of litters divided by number of inseminated females (as determined by observation of vaginal plug at E0.5). Average litter size is presented as mean ± SD number of pups.

	Plugged females	Number of litters	Fertility rate (percentage of litters)	Average litter size
Mthfd1l $^{z/+}$	40	35	87.5%	9.1±1.6
Mthfd1l $^{z/+}$ ***/ Aldh1l2*** $^{-/-}$	32	5	15.6%	7.2±1.2

4.3.1.2 Embryonic Phenotype

Due to the dramatically reduced fertility of *Mthfd1l*$^{tz/+}$/ *Aldh1l2*$^{-/-}$ mice, only 5 litters were alive at E10.5, the time of dissection of mothers that were determined to be pregnant, based on the observation of a conspicuous vaginal plug. Analysis of this limited number of *Mthfd1l*$^{tz/tz}$/ *Aldh1l2*$^{-/-}$ embryos revealed that 100% of the *Mthfd1l*-null, *Aldh1l2*-null embryos exhibited an open neural tube and severely stunted growth (Figure 4.3). When compared to *Mthfd1l*-null embryos alone, the double KO embryos had reduced crown-rump (CR) length, reduced overall body size, and were slightly more transparent. Because the y-intercepts of the trendlines of somite number versus CR length for each embryonic genotype group are not statistically significantly different ($p > 0.05$), the relationship between growth and developmental progression does not appear to be disrupted in *Mthfd1l*$^{tz/tz}$/ *Aldh1l2*$^{-/-}$ embryos (Figure 4.4).

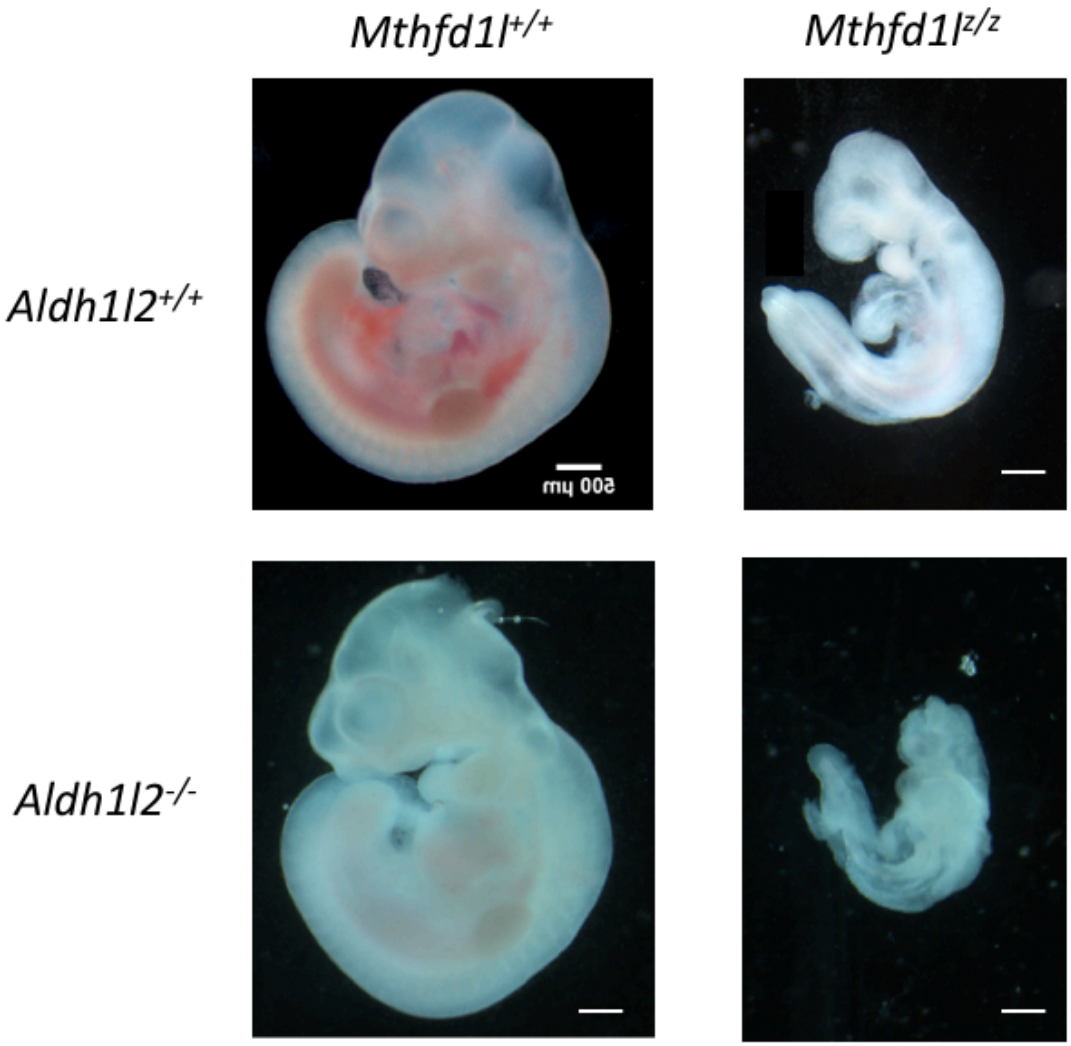

Figure 4.3. **Gross morphology of *Mthfd1l*/*Aldh1l2* breeding embryos at E10.5**. Matched littermates were imaged at 28X from breeding crosses with *Mthfd1l*$^{z/+}$ mice (top row) and *Mthfd1l*$^{z/+}$/*Aldh1l2*$^{-/-}$ mice (bottom row). Scalebar shown is 500µm. Deletion of both *Mthfd1l* and *Aldh1l2* results in an embryo with severely restricted growth, whereas deletion of *Aldh1l2* alone does not affect embryonic development.

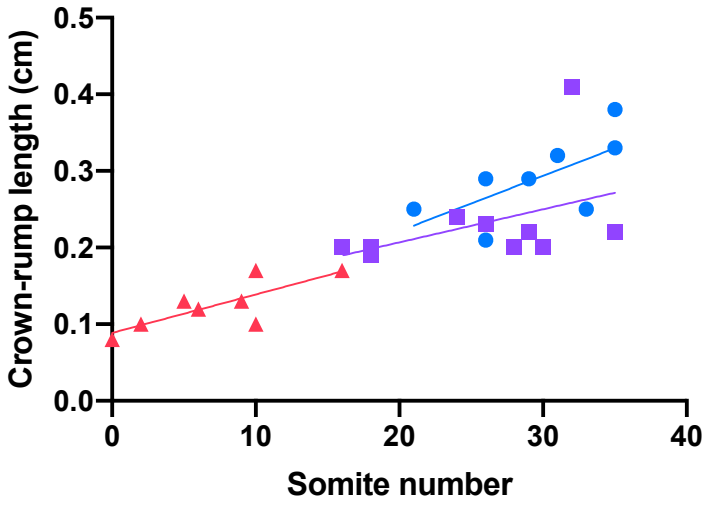

Figure 4.4. **Growth and developmental progression in *Mthfd1l/Aldh1l2* mutant embryos.** Growth is measured by crown-rump length, in centimeters, and developmental progression is measured by somite number of embryos. The relationship between growth and developmental progression does not appear to be disrupted in *Mthfd1l*$^{z/z}$/ *Aldh1l2*$^{-/-}$ embryos (p>0.05). (●, *Mthfd1l*$^{+/+}$ / *Aldh1l2*$^{-/-}$; ■ , *Mthfd1l*$^{z/+}$ / *Aldh1l2*$^{-/-}$; ▲, *Mthfd1l*$^{z/z}$ / *Aldh1l2*$^{-/-}$ embryos)

4.3.1.3 Adult Phenotype

Because *Mthfd1l* deletion is incompatible with life, *Mthfd1l*$^{z/z}$/*Aldh1l2*$^{-/-}$ mice do not survive to full term. However, the ≥ 8 week old *Mthfd1l*$^{z/+}$/*Aldh1l2*$^{-/-}$ mice used to breed *Mthfd1l*$^{z/z}$/*Aldh1l2*$^{-/-}$ embryos did present a phenotype (Figures 4.5 and 4.6).

Neither *Mthfd1l*$^{z/+}$ nor *Aldh1l2*$^{-/-}$ mice show any observable phenotype, but mice with a combined *Mthfd1l*$^{z/+}$/*Aldh1l2*$^{-/-}$ background do present a phenotype. These mice occasionally have congenital hydrocephaly and/or anophthalmia (lacking one or both eyes). Additionally, after 8 weeks of age, some display stunted growth and many have extremely low fertility rates.

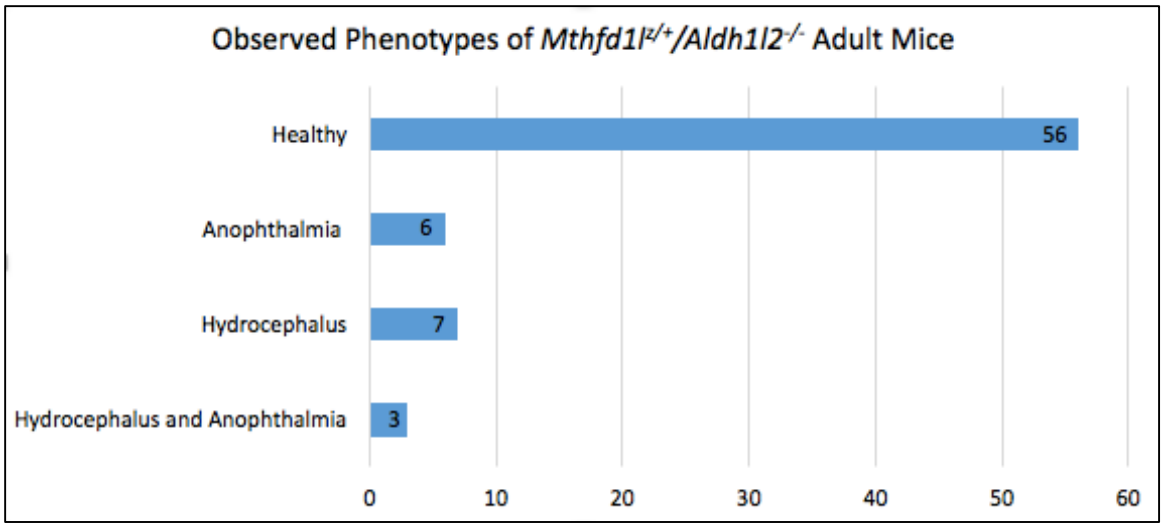

Figure 4.5. **Observed phenotypes of adult mice with the genotype *Mthfd1l*$^{-/+}$*/Aldh1l2*$^{-/-}$ born from *Mthfd1l*$^{-/+}$*/Aldh1l2*$^{+/-}$ breeding pairs**. Some mice, both male and female, were born with anophthalmia in one or both eyes (6), some were born with hydrocephalus (7), and some with both (3).

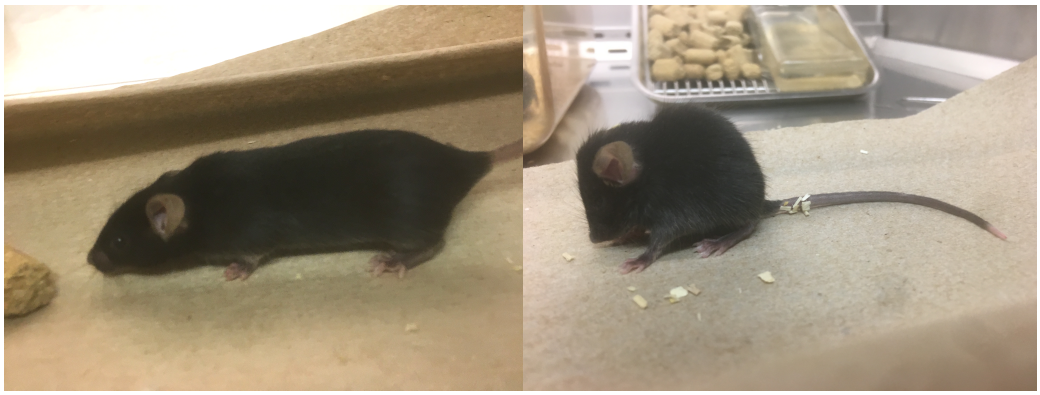

Figure 4.6. ***Mthfd1l*$^{-/+}$*/Aldh1l2*$^{-/-}$ mice occasionally display hydrocephalus and anopthalmia phenotype**. Image of healthy *Mthfd1l*$^{+/+}$*/Aldh1l2*$^{+/+}$ mouse (left) and image of mouse with *Mthfd1l*$^{-/+}$*/Aldh1l2*$^{-/-}$ genotype (right). Both mice pictured at an age of 6 weeks.

4.3.2 Analysis of Mthfd1l and Aldh1l2 Expression Across Different Mouse Lines

Adult liver lysates from mice with different genotypes were evaluated for Mthfd1l and Aldh1l2 protein expression (Figure 4.7). The purpose of this experiment was to determine if the observed phenotype of reduced fertility in *Mthfd1l*$^{+/+}$/*Aldh1l2*$^{-/-}$ mice was associated with varying levels of Mthfd1l expression across individual mice of this genotype. Expression levels of both Mthfd1l and Aldh1l2 are inconsistent within a single genotype. For example, among *Aldh1l2*$^{+/+}$ mice, Aldh1l2 expression varies across individuals. As expected, there was reduced expression of Mthfd1l and Aldh1l2 in mice heterozygous for either gene compared to WT homozygous expression levels.

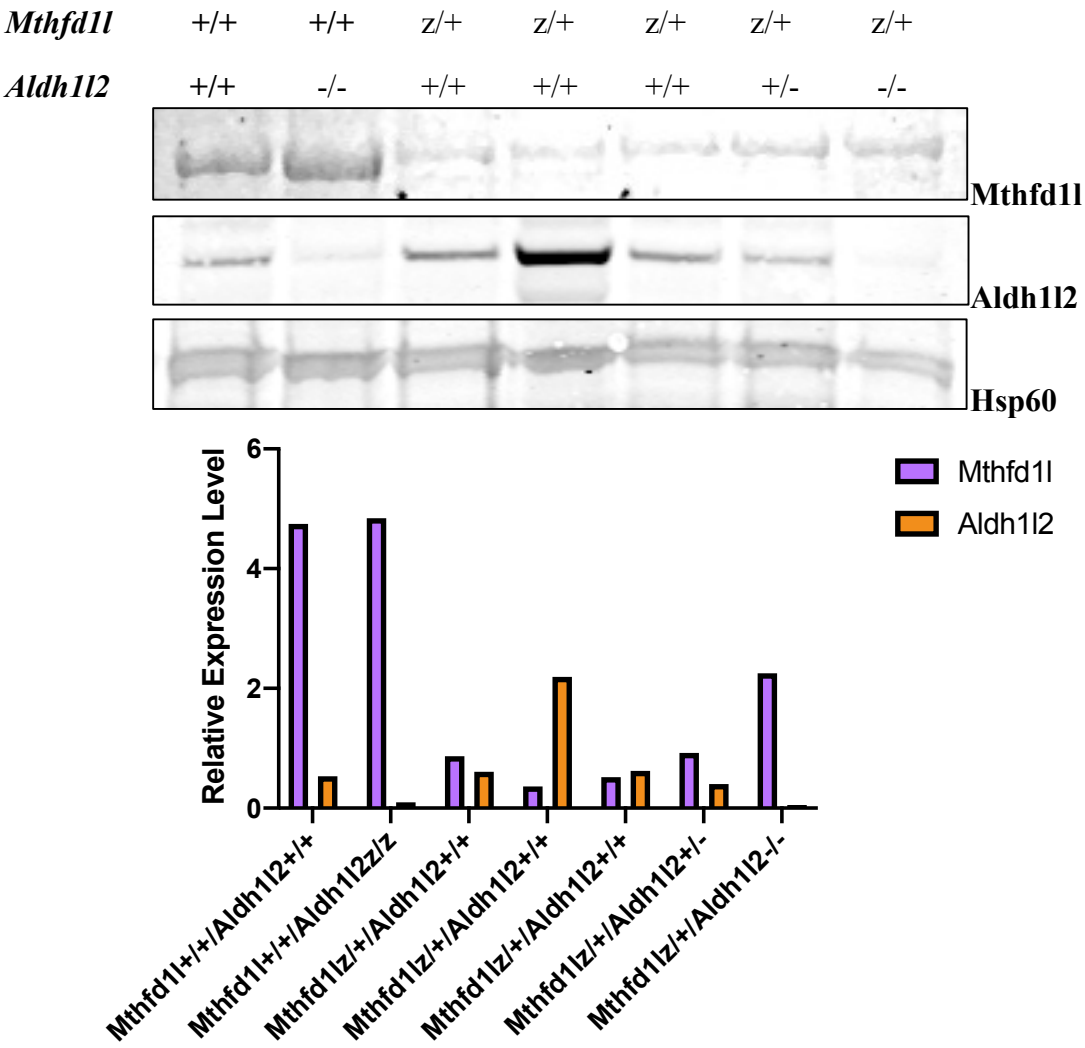

Figure 4.7. **Western blot analysis of Mthfd1l and Aldh1l2 expression in individual adult mouse livers of different genotypes**. Upper panel: Lane 1 contains mitochondrial lysate from a mouse with a WT background, lane 2 from *Mthfd1l*$^{+/+}$/*Aldh1l2*$^{-/-}$, lanes 3-5, from *Mthfd1l*$^{z/+}$/*Aldh1l2*$^{+/+}$, lane 6 from *Mthfd1l*$^{+/+}$/*Aldh1l2*$^{+/-}$, and lane 7 from *Mthfd1l*$^{z/+}$/*Aldh1l2*$^{-/-}$. Mitochondria were isolated from maternal livers, and a western blot of standardized total mitochondrial protein extracts was analyzed by SDS-PAGE electrophoresis. Each lane was loaded with 200 µg protein due to the low expression levels of Mthfd1l in adult mice. Immunoblots were probed with antibodies against Mthfd1l (100 kDa), Aldh1l2 (100kDa), and the mitochondrial matrix protein Hsp60 (60 kDa) as a loading control. Lower Panel: Densitometry of the expression of Mthfd1l and Aldh1l2 in upper panel normalized to the Hsp60 signal. Genotype of mice used in liver protein extraction along x-axis. Hsp60 expression level set to 1.0.

4.3.3 Formate Supplementation Fails to Rescue NTDs caused by *Mthfd1l* and *Aldh1l2* Deletion

Because formate supplementation has been shown to partially rescue the NTD and growth defect in *Mthfd1l*$^{e/z}$ embryos, the *Mthfd1l*$^{e/z}$/*Aldh1l2*$^{-/-}$ embryos were also supplemented to evaluate if partial rescue was possible. Pregnant mothers were supplemented with calcium formate at a dose of 2,500 mg/kg/day in the drinking water. The reduced fertility of *Mthfd1l*$^{e/+}$/*Aldh1l2*$^{-/-}$ adult mice was not improved with formate supplementation, and of 12 supplemented pregnant mothers, only 2 litters were present at E10.5, when mothers were dissected. Although this study is extremely limited in sample size, calcium formate supplementation did not rescue the NTDs or growth defects of *Mthfd1l*$^{e/z}$/*Aldh1l2*$^{-/-}$ embryos (Figure 4.8).

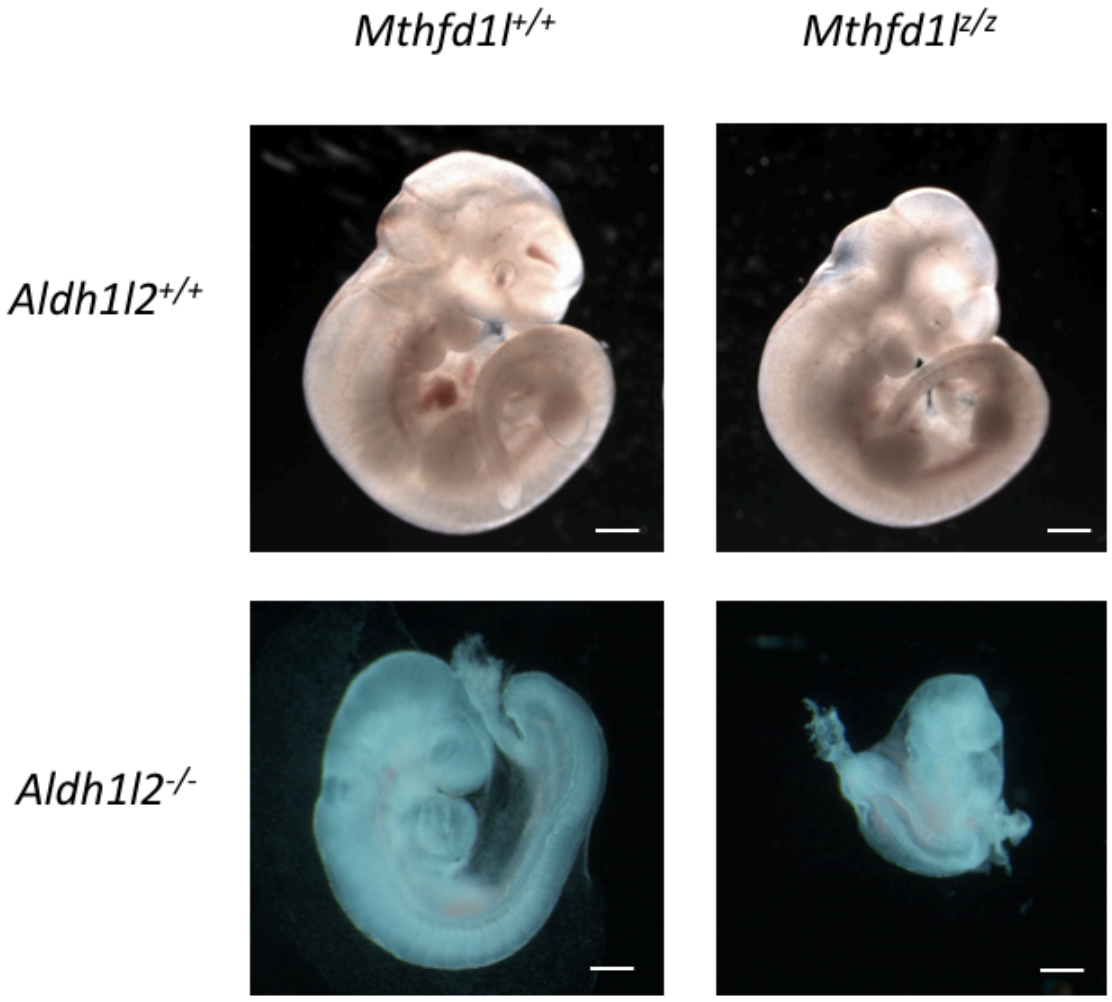

Figure 4.8. **Formate supplementation of *Mthfd1l*$^{z/z}$/*Aldh1l2*$^{-/-}$ embryos does not rescue growth defect phenotype as significantly as it does *Mthfd1l*$^{z/z}$ mice**. Embryos imaged at E10.5. In the top panel, the supplementation of calcium formate at a dose of 2,500 mg/kg/day in maternal drinking water partially rescues the growth defect in *Mthfd1l*$^{z/z}$ embryos (experiment done by Dr. Jessica Momb), but the same treatment fails to rescue the growth defect in *Mthfd1l*$^{z/z}$/*Aldh1l2*$^{-/-}$ embryos as significantly.

4.3.4 Deletion of *Mthfd1l* and *Aldh1l2* Disrupts Embryonic Tissue Organization

Like in Chapter 2.3.2, the histology of *Mthfd1l*$^{e/z}$/*Aldh1l2*$^{-/-}$ embryos were evaluated by H&E stains of paraffin sections. The cranial tissue of *Mthfd1l*$^{e/z}$/*Aldh1l2*$^{-/-}$ embryos appeared disordered and cell shape was dysmorphic, unlike the round and evenly distributed cells observed in WT embryos (Figure 4.9). This observation was consistent from transverse sections starting in the cranial regions to the branchial arches. The sample population for this experiment was n=1 WT, with multiple technical replicates throughout the embryo, and n=2 *Mthfd1l*$^{e/z}$/*Aldh1l2*$^{-/-}$, also with multiple sections throughout the embryo.

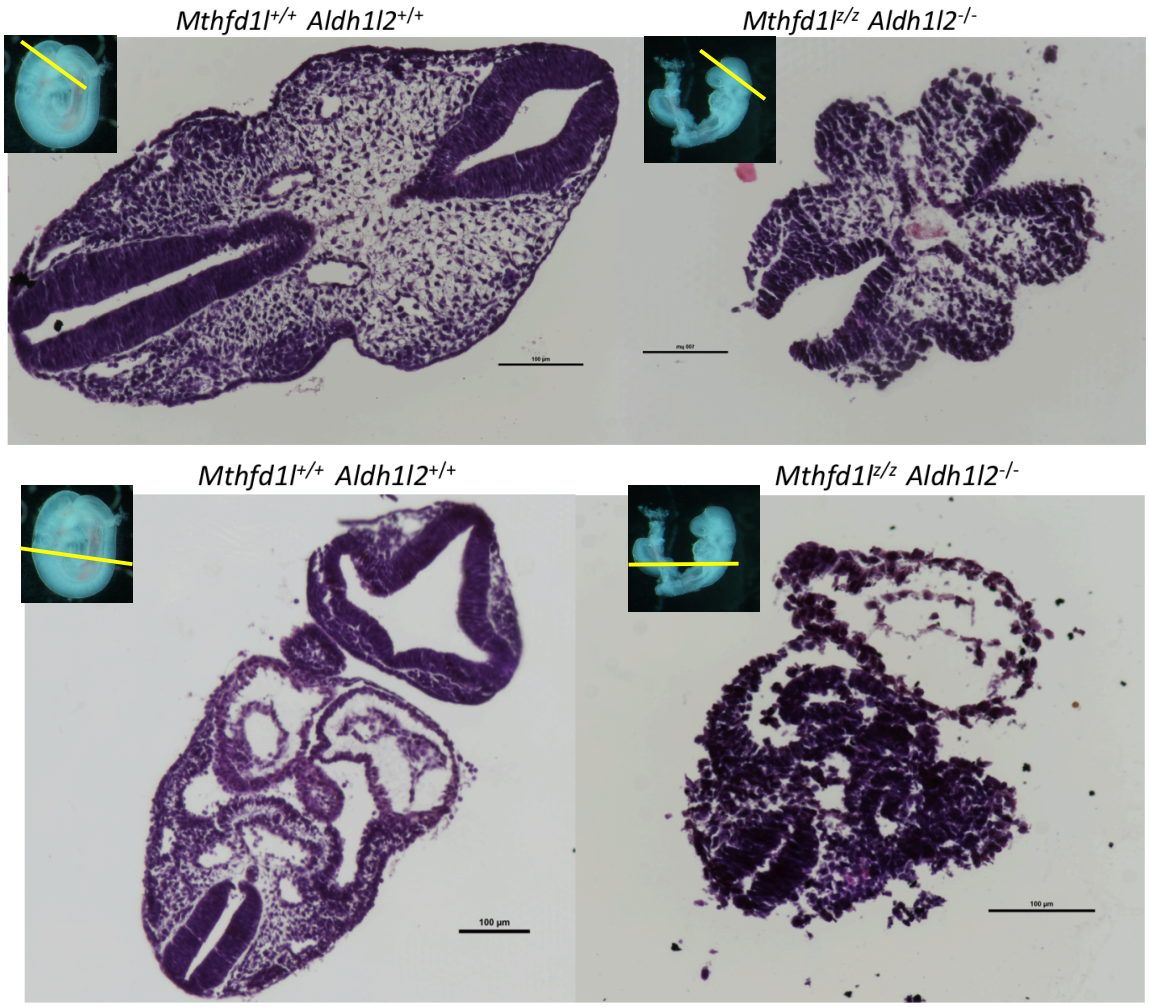

Figure 4.9. **Deletion of Mthfd1l and Aldh1l2 result in disrupted cell structure and tissue organization**. H&E stains of paraffin embedded E10.5 embryo sections along the transverse plane in the cranial region (top panel) and through the branchial arches (bottom panel). n=1 WT (left), and n=2 *Mthfd1l*$^{z/z}$/*Aldh1l2*$^{-/-}$ (right).

4.3.5 Deletion of *Mthfd1l* and *Aldh1l2* Disrupts Extracellular Matrix Structure

Hyaluronic acid (HA) has been shown to influence mesenchyme cell fate, proliferation, adhesion, and morphology, which are all important during neural tube closure (Chen et al., 2007; Knudson, 2003; Morris-Wiman and Brinkley, 1990a; Nilsson et al., 2003; Peck and Isacke, 1996). As with the *Mthfd1l*$^{z/z}$ embryo analysis in Figure 2.5, *Mthfd1l*$^{z/z}$*/Aldh1l2*$^{-/-}$ embryos were evaluated for HA composition within the ECM. Littermate embryos dissected at E10.5 were paraffin embedded, sectioned, and stained with Alcian blue to detect HA and evaluate the integrity of the ECM, and determine if it is more poorly structured than in the *Mthfd1l*$^{z/z}$ embryo. *Mthfd1l*$^{z/z}$*/Aldh1l2*$^{-/-}$ embryos not only display sparse distribution of mesenchyme, but HA is not evenly distributed throughout the ECM, causing cell clusters and poor adhesion and matrix formation between mesenchyme cells. This experiment was done with a sample size of n=2 embryos per group.

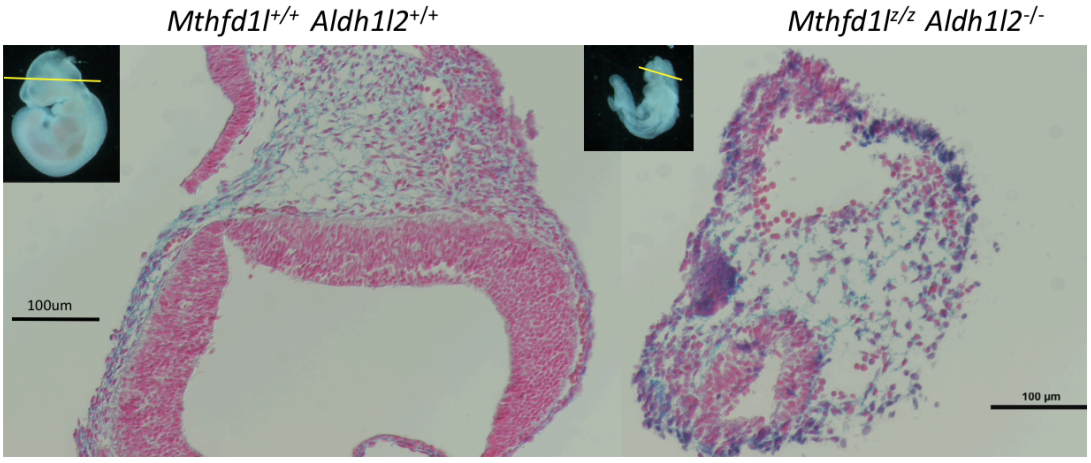

Figure 4.10. ***Mthfd1l***$^{z/z}$ ***/Aldh1l2***$^{-/-}$ **embryos have a disruption in HA distribution in the ECM**. Alcian blue staining of paraffin embedded sections at E10.5 of WT (left) and *Mthfd1l*$^{z/z}$ */Aldh1l2*$^{-/-}$ (right) mouse embryos. Nuclear fast red was used as a counterstain, and appears pink. n=2 for both groups.

4.3.6 Males with *Mthfd1l*$^{+/+}$/*Aldh1l2*$^{-/-}$ Genotype Exhibit Healthy Testes and Sperm

Because adult *Mthfd1l*$^{+/+}$/*Aldh1l2*$^{-/-}$ mice exhibit reduced fertility, the testis and sperm cells of *Mthfd1l*$^{+/+}$/*Aldh1l2*$^{-/-}$ males was examined for any observable phenotype. The testes of 6-month-old WT and *Mthfd1l*$^{+/+}$/*Aldh1l2*$^{-/-}$ mice appeared to be approximately the same size, and no overall significant difference was observed. Mice dissected for analysis had been mated previously with female mice of the same age.

Similarly, the sperm of both groups were robust and motile, indicating that the lack of fertility was not caused by unhealthy nor insufficient sperm production in *Mthfd1l*$^{+/+}$/*Aldh1l2*$^{-/-}$ male mice.

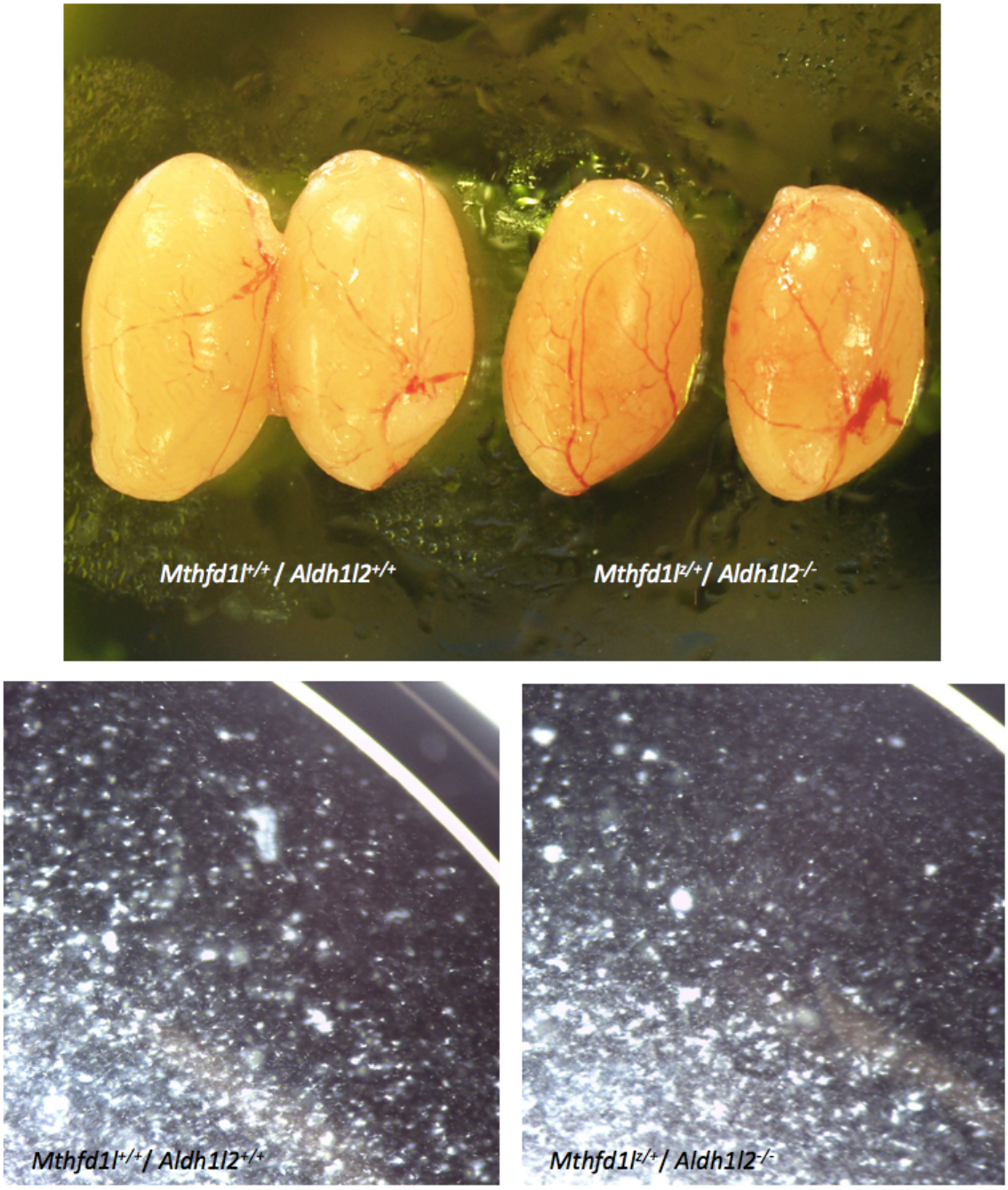

Figure 4.11. ***Mthfd1l***$^{z/+}$***/ Aldh1l2***$^{-/-}$ **adult males appear to be fertile with healthy testes and sperm**. Top panel: Testis of WT (left) and *Mthfd1l*$^{z/+}$*/ Aldh1l2*$^{-/-}$ (right) males. Bottom panel: Sperm of WT (left) and *Mthfd1l*$^{z/+}$*/ Aldh1l2*$^{-/-}$ (right) males. Both cell populations appeared robust and motile, indicating that the *Mthfd1l*$^{z/+}$*/ Aldh1l2*$^{-/-}$ genotype does not lead to unhealthy sperm in adult male mice.

4.4 DISCUSSION

This study was designed to examine if Aldh1l2 serves as a source of formate *in vivo*, and also to further explore the importance of formate during neurulation. Due to the observed phenotype of reduced fertility in the parental F1 generation, we were unable to collect a sufficient number of embryo samples to confirm with confidence the developmental consequences of a *Mthfd1l*$^{tz/tz}$/*Aldh1l2*$^{-/-}$ mutant mouse. This chapter is a reflection of the work completed on this mouse model, however these experiments will need to be repeated to generate essential statistical support of a larger sample size.

From the limited number of available embryos, we observed that *Mthfd1l*$^{tz/tz}$/*Aldh1l2*$^{-/-}$ embryos were further reduced in size compared with *Mthfd1l*$^{tz/tz}$ embryos (Figure 4.3), and were not responsive to maternal formate supplementation (Figure 4.8). It is possible that in the *Mthfd1l*$^{tz/tz}$ embryo, the formate produced by Aldh1l2 in combination with 2,500 mg/kg sodium formate daily in maternal drinking water is sufficient to partially improve the growth defects that occur without supplementation. If this is the case, then *Mthfd1l*$^{tz/tz}$/*Aldh1l2*$^{-/-}$ embryos may not have enough basal formate production to respond to exogenous maternally-sourced formate. In the future, experiments using labeled formate in maternal drinking water are warranted in order to examine the fate of maternal formate in the embryo.

Histological analysis revealed cellular disorganization in the neural tissue of E10.5 embryos lacking Mthfd1l and Aldh1l2 (Figure 4.9). This embryonic phenotype was similar to that of *Cbp-/-* embryos, which lack a gene associated with pattern formation and exhibit exencephaly, defective NTC, and reduced density of neuroepithelium (Tanaka et al., 2000). *Cbp-/-* mice die between E10.5-12.5 due to defective blood vessel formation in the central nervous system. Although it is unknown

what caused the observed defects in *Mthfd1l*$^{gt/tz}$/*Aldh1l2*$^{-/-}$ embryos, it may be informative to examine haematopoiesis in this mouse in the future.

A recent experiment suggests that respiring mitochondria lacking Mthfd1l expression continue to produce formate, and evidence an increase in Aldh1l2 expression (Copp and Greene, 2013). In order to test our hypothesis that the measured formate was a product of the Aldh1l2 hydrolase reaction, we planned to repeat the serine oxidation assay using isolated respiring mitochondria from *Mthfd1l*$^{gt/tz}$/*Aldh1l2*$^{-/-}$ embryos. This experiment requires a substantial amount of embryos in order to isolate enough mitochondria to generate a detectable quantity of formate. Unfortunately, the reduced fertility in the *Mthfd1l*$^{gt/+}$/*Aldh1l2*$^{-/-}$ parent generation prevented sufficient collection of embryos which was necessary to realize the assay at this time. It will be necessary to carry out this experiment in the future in order to test the hypothesis that Aldh1l2 is a source of mitochondrial formate during development. Because maternal formate supplementation failed to prevent the infertility issue, additional approaches to enhance fertility may be successful. It has been shown that maternal diets supplemented with omega 3-fatty acids improves egg health (Nehra et al., 2012), therefore possible dietary supplementation may enhance fertility in *Mthfd1l*$^{gt/+}$/*Aldh1l2*$^{-/-}$ females. In this study, the fertility of *Mthfd1l*$^{gt/+}$/*Aldh1l2*$^{-/-}$ males were examined to reveal healthy spermatogenesis, as sperm count and motility was indistinguishable from WT sperm (Figure 4.11). The fertility of both *Mthfd1l*$^{gt/+}$/*Aldh1l2*$^{-/-}$ males and females was further investigated by cross-mating adults with their WT counterparts, yet these breeding pairs also did not become pregnant.

To our knowledge, there are no examples of mice mutant for one-carbon pathway genes that evidence only a reduction in fertility. It is unclear what may have caused this dramatic reduction in pregnancy, although it has been reported that fertility in rodents

decreases during times of stress (Castelhano-Carlos and Baumans, 2009). Given that the *Mthfd1l*$^{+/+}$ mice are from a C57BL/6N substrain mouse, and the *Aldh1l2*$^{-/-}$ mice are from a C57BL/6J substrain, it may be that one or a combination of both leads to an increase in sensitivity to stress.

In addition to the challenges of reduced fertility, adult *Mthfd1l*$^{+/+}$/*Aldh1l2*$^{-/-}$ mice also evidenced an abnormally high instance of hydrocephalus—10 out of 72 total adults. In C57BL/6 mice, the reported hereditary rate of hydrocephalus is 1-4% (Sundberg et al.), however we found that to be the case for 13.89% of *Mthfd1l*$^{+/+}$/*Aldh1l2*$^{-/-}$ mice in this study. Hydrocephalus is often associated with NTDs (Copp and Greene, 2013), therefore it was considered that mice with mutations in both *Mthfd1l* and *Aldh1l2* may have NTDs or delayed NTC. The expression of Mthfd1l and Aldh1l2 of *Mthfd1l*$^{+/+}$/*Aldh1l2*$^{-/-}$ mice were investigated (Figure 4.7), and mice heterozygous for either gene displayed variable expression levels: between 7.8 and 47.9% that of WT. It is possible that in some cases, expression levels were low enough to reduce overall catalytic activity and disrupt healthy development. Further protein expression assays will be required to make any conclusions about the cause of hydrocephalus, anophthalmia, and reduced fertility in *Mthfd1l*$^{+/+}$/*Aldh1l2*$^{-/-}$ mice. Although the relationship between Aldh1l2 and formate metabolism during development remains unclear, the embryonic and adult phenotypes described in this chapter indicate that this topic is worthy of continued evaluation.

CHAPTER 5: SUMMARY, CONCLUSIONS, AND FUTURE DIRECTIONS

5.1 SUMMARY

Mthfd1l is the only known mitochondrial enzyme that catalyzes the production of formate from 10-formyl THF (Prasannan et al., 2003). This formate is used in purine and thymidylate synthesis, and accounts for at least 75% of the 1C units that enter the methyl cycle (Pike et al., 2010). The work presented in this dissertation is focused on understanding how mitochondrially-derived formate supports healthy neurulation, and exploring additional sources of mitochondrial formate. Paraffin sectioning of *Mthfd1l*-null mouse embryos revealed reduced density in cranial mesenchyme and dysregulated extracellular matrix (ECM) formation. The ECM component hyaluronic acid (HA) is associated with proper neural fold elevation (Morris-Wiman and Brinkley, 1990a). HA was found to be decreased in abundance in null embryos. Similarly, expression of basement membrane protein Collagen IV was reduced in embryos lacking Mthfd1l. Imaging mass spectrometry (IMS) suggested that decreased purine, thymidylate, and amino acid synthesis occurs in *Mthfd1l*-null cranial mesenchyme, as well as altered energy metabolism. Residual production of formate from *Mthfd1l*-null mitochondria suggests that Aldh1l2 may contribute to formate synthesis in the mitochondria (Figure 5.1) (Bryant et al., 2018). A *Mthfd1l*/*Aldh1l2* double KO mouse line was constructed to test this hypothesis. Mouse embryos null for both genes exhibited dramatic defects in growth, which were not improved with maternal formate supplementation.

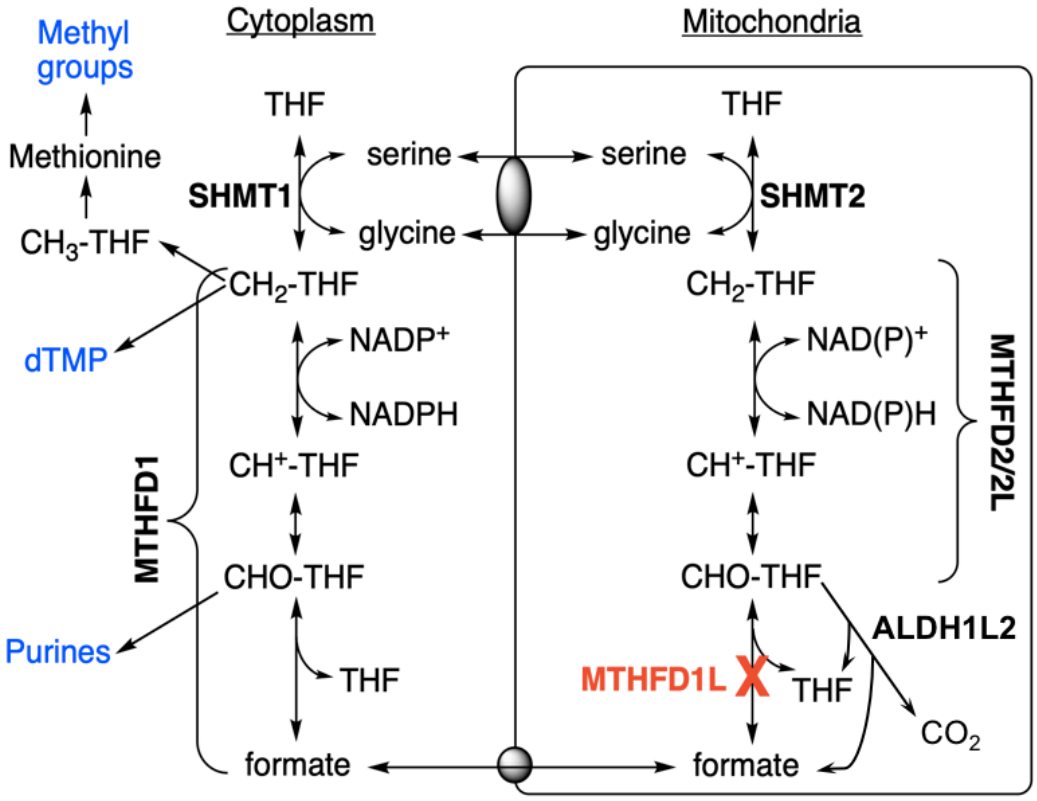

Figure 5.1. **Hypothetical model of formate production in the mitochondria.** Deletion of *Mthfd1l* reduces formate production and flux through folate-dependent one-carbon metabolism, yet mitochondria from *Mthfd1l*-null mouse embryos still produce formate (Bryant et al., 2018). Mitochondrially-derived formate enters the cytoplasm and fuels the production of purines, thymidylate (dTMP), and methyl groups via AdoMet. Grey ovals represent putative metabolite transporters.

5.2 Conclusions and Future Directions

Deletion of *Mthfd1l* causes dysregulated mesenchyme development (Shin, 2016), and my work described in Chapter 2 focused on understanding the origin of these defects. The reduced density of cranial mesenchyme cells in *Mthfd1l*$^{-/-}$ embryos prior to NTC was confirmed with classical histological analysis of paraffin-embedded tissue. Alcian blue staining reflected defects in glycosaminoglycan (GAG) formation, which suggests that the ECM does not form properly in embryos without *Mthfd1l* expression. Because the ECM influences mesenchyme formation (Assis-Ribas et al., 2018; Gattazzo et al., 2014; Hall and Watt, 1989; Wang and Chen, 2013; Watt and Huck, 2013), I hypothesized that the poorly formed mesenchyme evident in *Mthfd1l*$^{-/-}$ embryos was associated with dysregulated ECM development. This hypothesis was investigated using immunohistochemistry to evaluate the integrity of the ECM in embryonic cranial tissue lacking *Mthfd1l*, and Collagen IV expression was found to be significantly reduced. Fibronectin expression was also examined, and was not altered in *Mthfd1l*$^{-/-}$ embryos. Continued work is needed in order to understand this association between ECM proteins and mesenchyme formation in *Mthfd1l*$^{-/-}$ mice. I am currently studying the expression of Collagen I and Laminin α5 in embryos to better understand how *Mthfd1l* deletion impacts ECM formation during development.

I complimented my evaluation of cranial tissue formation with non-targeted metabolomics analysis of *Mthfd1l*$^{-/-}$ embryos in the regions where mesenchyme defects were observed. We collaborated with the Eberlin research group to perform DESI-IMS on these embryos, and analyzed significant differences in metabolite abundance between WT and *Mthfd1l*-null embryos. We determined that *Mthfd1l* deletion led to reduced abundance in purine and thymidylate derivatives in the cranial mesenchyme tissue, as well as a reduction in amino acids. The cranial tissue of null mice also reflected

dysregulated energy metabolism. Further work that utilizes the high resolution of MALDI-IMS will be needed in order to evaluate formate distribution and abundance in the cranial mesenchyme of *Mthfd1l*$^{e/z}$ embryos. The use of IMS to correlate tissue formation and metabolism provides a direct link between biochemistry and development. In turn, continued application of this approach using additional developmental mutant models will expand our current understanding of the role of metabolism during development.

Because Mthfd1l is a mitochondrial protein that encourages both metabolic homeostasis and healthy tissue formation, it is also a possibility that mitochondria lacking *Mthfd1l* are not properly formed. Work is currently underway to evaluate the state of mitochondria in *Mthfd1l*$^{e/z}$ embryos using electron microscopy.

Mitochondria derived from *Mthfd1l*-null embryos continue to produce a small amount of formate and exhibit an increase in *Aldh1l2* expression (Bryant et al., 2018). I explored the hypothesis that Aldh1l2, which can produce formate *in vitro* (Krupenko et al., 2010), is responsible for the formate synthesis we observe in *Mthfd1l*$^{e/z}$ embryos. I did this by breeding mice null for both *Mthfd1l* and *Aldh1l2*, which hypothetically lack mitochondrial production of formate. A breeding phenotype of reduced fertility in the parental *Mthfd1l*$^{e/+}$ */Aldh1l2*$^{-/-}$ generation prevented my collection of a sufficient number of embryo samples. Of the *Mthfd1l*$^{e/z}$ */Aldh1l2*$^{-/-}$ embryos I was able to collect, I observed more dramatic growth defects than those of *Mthfd1l*$^{e/z}$ embryos. Additionally, formate supplementation did not rescue the phenotype as significantly as it does *Mthfd1l*$^{e/z}$ embryos. Lastly, both mesenchyme tissue formation and ECM composition appeared dysregulated in *Mthfd1l*$^{e/z}$ */Aldh1l2*$^{-/-}$ embryos. More studies of this double KO mouse model are needed in order to repeat my work and confirm my observations, which can be done with continued breeding of *Mthfd1l*$^{e/+}$ */Aldh1l2*$^{-/-}$ mice. Furthermore, a serine tracing

experiment should be performed in mitochondria isolated from *Mthfd1l*$^{f/z}$/*Aldh1l2*$^{-/-}$ embryos, because if Aldh1l2 is responsible for redundant mitochondrial formate production, no serine will be oxidized to formate.

Appendix I: List of Acronyms

1C: One-carbon

AICAR: Aminoimidazole carboxamide ribonucleotide

ALDH1L1: Cytoplasmic 10-CHO-THF dehydrogenase

ALDH1L2: Mitochondrial 10-CHO-THF dehydrogenase

AMT: Aminotransferase

BHMT: Betaine hydroxymethyltransferase

CDC: Centers for disease control and prevention

CNS: Central nervous system

CR: Crown-rump

cSHMT: Cytoplasmic serine hydroxymethyltransferase

DHFR: Dihydrofolate reductase

DMG: Dimethylglycine

DMGDH: Dimethylglyine dehydrogenase

DLHP: Dorsolateral hingepoint

dTMP: Thymidylate

dUMP: Deoxyuridylate

FDR: False discovery rate

FPGS: Folylpolyglutamate synthetase

GAR: Glycinamide ribonucleotide

GCS-H: Glycine cleavage system H

GLDC: Glycine decarboxylase

H&E: Hematoxylin and eosin

$IF2_{mt}$: Mitochondrial translation initiation factor

m/z: mass to charge ratio

MEFs: Mouse embryonic fibroblasts

MHP: Median hinge point

MSCs: Mesenchymal stem cells

MTHFD1: C_1-THF-synthase

MTHFR: Methylenetetrahydrofolate reductase

MTFMT: Methionyl-tRNA formyltransferase

NTC: Neural tube closure

NTD: Neural tube defect

PABA: Para-aminobenzoic acid

PCFT: Proton-coupled folate transporter

RFC: Reduced folate carrier

SAM: S-adenosyl methionine

SDH: Sarcosine dehydrogenase

SHMT: Serine hydroxymethyltransferase

SFXN1: Sideroflxin 1

SNP: Single nucleotide polymorphism

SUMO: Small ubiquitin-like modifier

TCA: Tricarboxylic acid

THF: Tetrahydrofolate

TS: Thymidylate synthase

Appendix II: A Protocol of Paraffin Embedding of Embryos E7-9.5 for Histological Analysis

1. Dissect embyros in ice cold PBS, then transfer to small glass vial, and incubate in 4% Paraformaldehyde in PBS overnight at 4º C.
2. Wash fixed embryos twice with room temperature PBS.
3. Incubate embryo in 70% EtOH for 5 minutes.
4. Incubate embryo in 95% EtOH for 5 minutes.
5. Incubate embryo in 100% EtOH for 5 minutes, twice.
6. Incubate embryo in Xylene Substitute (Histo-Clear, National Diagnostics) for 5 minutes, twice.
7. Transfer the embryos into Peel-a-way disposable plastic embedding molds (Polysciences, Inc) containing melted paraffin at 60°C.
8. Incubate embryo in paraffin for 5 minutes.
9. Remove and replace the paraffin with fresh paraffin at 60°C.
10. Incubate embryo at 60°C for 15 minutes.
11. Repeat step 9.
12. Incubate embryo at 60°C for 30 minutes.
13. Orient embryo in the correct position within the embedding mold under a dissection microscope (Nikon Eclipse Compound Microscope).
14. Allow paraffin to harden completely overnight, or incubate mold on ice for 1 hour to expedite processing.
15. Peel off embedding mold, maintaining correct alignment and position of embedded embryo, and cut away excess paraffin using razor.

16. Prepare paraffin embedding cassette (Shandon Biopsy Processing/Embedding Casette, Thermo Fisher), alongside melted paraffin wax, a metal lab spatula, and a Bunsen burner.
17. Pipette several drops of molten paraffin onto embedding cassette to create a base onto which the paraffin block will adhere onto the cassette.
18. Heat metal spatula over Bunsen burner, and use to melt bottom of excised embryo-containing paraffin block.
19. Quickly apply the embryo-containing paraffin block onto the cassette where the molten paraffin has been deposited, and mount the paraffin onto the cassette.
20. Repeat step 14.
21. Once completely hardened, section embryo at 7μm using a microtome (Leica Biosystems), and mount on negatively charged glass microscope slides. Proceed with histological analysis (H&E, Alcian blue, etc).

References

Afman, L.A., Blom, H.J., Drittij, M.-J., Brouns, M.R., and van Straaten, H.W.M. (2005). Inhibition of transmethylation disturbs neurulation in chick embryos. Brain Res. Dev. Brain Res. *158*, 59–65.

Agathocleous, M., and Harris, W.A. (2013). Metabolism in physiological cell proliferation and differentiation. Trends Cell Biol. *23*, 484–492.

Anderson, D.D., and Stover, P.J. (2009). SHMT1 and SHMT2 Are Functionally Redundant in Nuclear De novo Thymidylate Biosynthesis. PLOS ONE *4*, e5839.

Anderson, D.D., Woeller, C.F., and Stover, P.J. (2007). Small ubiquitin-like modifier-1 (SUMO-1) modification of thymidylate synthase and dihydrofolate reductase. Clin. Chem. Lab. Med. *45*, 1760–1763.

Anderson, S., Bankier, A.T., Barrell, B.G., de Bruijn, M.H., Coulson, A.R., Drouin, J., Eperon, I.C., Nierlich, D.P., Roe, B.A., Sanger, F., et al. (1981). Sequence and organization of the human mitochondrial genome. Nature *290*, 457–465.

Angelakopoulou, A., Shah, T., Sofat, R., Shah, S., Berry, D.J., Cooper, J., Palmen, J., Tzoulaki, I., Wong, A., Jefferis, B.J., et al. (2012). Comparative analysis of genome-wide association studies signals for lipids, diabetes, and coronary heart disease: Cardiovascular Biomarker Genetics Collaboration. Eur. Heart J. *33*, 393–407.

Anthony, T.E., and Heintz, N. (2007). The folate metabolic enzyme ALDH1L1 is restricted to the midline of the early CNS, suggesting a role in human neural tube defects. J. Comp. Neurol. *500*, 368–383.

Assis-Ribas, T., Forni, M.F., Winnischofer, S.M.B., Sogayar, M.C., and Trombetta-Lima, M. (2018). Extracellular matrix dynamics during mesenchymal stem cells differentiation. Dev. Biol. *437*, 63–74.

Bamforth, S.D., Bragança, J., Eloranta, J.J., Murdoch, J.N., Marques, F.I.R., Kranc, K.R., Farza, H., Henderson, D.J., Hurst, H.C., and Bhattacharya, S. (2001). Cardiac malformations, adrenal agenesis, neural crest defects and exencephaly in mice lacking Cited2, a new Tfap2 co-activator. Nat. Genet. N. Y. *29*, 469–474.

Barlowe, C.K., and Appling, D.R. (1988). In vitro evidence for the involvement of mitochondrial folate metabolism in the supply of cytoplasmic one-carbon units. BioFactors Oxf. Engl. *1*, 171–176.

Benjamini, Y., and Hochberg, Y. (1995). Controlling the False Discovery Rate: A Practical and Powerful Approach to Multiple Testing. J. R. Stat. Soc. Ser. B Methodol. *57*, 289–300.

Berk, M., Desai, S.Y., Heyman, H.C., and Colmenares, C. (1997). Mice lacking the ski proto-oncogene have defects in neurulation, craniofacial, patterning, and skeletal muscle development. Genes Dev. *11*, 2029–2039.

Berry, R.J., Li, Z., Erickson, J.D., Li, S., Moore, C.A., Wang, H., Mulinare, J., Zhao, P., Wong, L.-Y.C., Gindler, J., et al. (1999). Prevention of neural-tube defects with folic acid in China. N. Engl. J. Med. Boston *341*, 1485–1490.

Bestwick, J.P., Huttly, W.J., Morris, J.K., and Wald, N.J. (2014). Prevention of Neural Tube Defects: A Cross-Sectional Study of the Uptake of Folic Acid Supplementation in Nearly Half a Million Women. PLoS One San Franc. *9*, e89354.

Blom, H.J., Shaw, G.M., den Heijer, M., and Finnell, R.H. (2006). Neural tube defects and folate: case far from closed. Nat. Rev. Neurosci. *7*, 724–731.

Bolusani, S., Young, B.A., Cole, N.A., Tibbetts, A.S., Momb, J., Bryant, J.D., Solmonson, A., and Appling, D.R. (2011). Mammalian MTHFD2L Encodes a Mitochondrial Methylenetetrahydrofolate Dehydrogenase Isozyme Expressed in Adult Tissues. J. Biol. Chem. *286*, 5166–5174.

Brosnan, M.E., and Brosnan, J.T. (2016). Formate: The Neglected Member of One-Carbon Metabolism. Annu. Rev. Nutr. *36*, 369–388.

Bryant, J.D., Sweeney, S.R., Sentandreu, E., Shin, M., Ipas, H., Xhemalce, B., Momb, J., Tiziani, S., and Appling, D.R. (2018). Deletion of the neural tube defect-associated gene Mthfd1l disrupts one-carbon and central energy metabolism in mouse embryos. J. Biol. Chem. *293*, 5821–5833.

Cantoni, G.L. (1951). METHYLATION OF NICOTINAMIDE WITH A SOLUBLE ENZYME SYSTEM FROM RAT LIVER. J. Biol. Chem. *189*, 203–216.

Castelhano-Carlos, M.J., and Baumans, V. (2009). The impact of light, noise, cage cleaning and in-house transport on welfare and stress of laboratory rats. Lab. Anim. *43*, 311–327.

Centers for Disease Control and Prevention (1992). Recommendations for the Use of Folic Acid to Reduce the Number of Cases of Spina Bifida and Other Neural Tube Defects. Morb. Mortal. Wkly. Rep. Recomm. Rep. *41*, 1–7.

Centers for Disease Control and Prevention (1999). Knowledge and Use of Folic Acid by Women of Childbearing Age—United States, 1995 and 1998. JAMA *281*, 1883–1884.

Chamoux, E., Narcy, A., Lehoux, J.-G., and Gallo-Payet, N. (2002). Fibronectin, Laminin, and Collagen IV as Modulators of Cell Behavior during Adrenal Gland Development in the Human Fetus. J. Clin. Endocrinol. Metab. *87*, 1819–1828.

Chang, H., Zhang, T., Zhang, Z., Bao, R., Fu, C., Wang, Z., Bao, Y., Li, Y., Wu, L., Zheng, X., et al. (2011). Tissue-specific distribution of aberrant DNA methylation associated with maternal low-folate status in human neural tube defects. J. Nutr. Biochem. *22*, 1172–1177.

Chen, Z.F., and Behringer, R.R. (1995). twist is required in head mesenchyme for cranial neural tube morphogenesis. Genes Dev. *9*, 686–699.

Chen, P.-Y., Huang, L.L.H., and Hsieh, H.-J. (2007). Hyaluronan preserves the proliferation and differentiation potentials of long-term cultured murine adipose-derived stromal cells. Biochem. Biophys. Res. Commun. *360*, 1–6.

Chiang, P.K., Gordon, R.K., Tal, J., Zeng, G.C., Doctor, B.P., Pardhasaradhi, K., and McCann, P.P. (1996). S-Adenosylmethionine and methylation. FASEB J. Off. Publ. Fed. Am. Soc. Exp. Biol. *10*, 471–480.

Christensen, K.E., Patel, H., Kuzmanov, U., Mejia, N.R., and MacKenzie, R.E. (2005). Disruption of the Mthfd1 Gene Reveals a Monofunctional 10-Formyltetrahydrofolate Synthetase in Mammalian Mitochondria. J. Biol. Chem. *280*, 7597–7602.

Coelho, C.N., and Klein, N.W. (1990). Methionine and neural tube closure in cultured rat embryos: morphological and biochemical analyses. Teratology *42*, 437–451.

Colas, J.F., and Schoenwolf, G.C. (2001). Towards a cellular and molecular understanding of neurulation. Dev. Dyn. Off. Publ. Am. Assoc. Anat. *221*, 117–145.

Cook, R.J., and Blair, J.A. (1979). The distribution and chemical nature of radioactive folates in rat liver cells and rat liver mitochondria. Biochem. J. *178*, 651–659.

Cook, R.J., and Wagner, C. (1982). Purification and partial characterization of rat liver folate binding protein: cytosol I. Biochemistry *21*, 4427–4434.

Copp, A.J. (2005). Neurulation in the cranial region--normal and abnormal. J. Anat. *207*, 623–635.

Copp, A.J., and Greene, N.D.E. (2013). Neural tube defects – disorders of neurulation and related embryonic processes. Wiley Interdiscip. Rev. Dev. Biol. *2*, 213–227.

Copp, A.J., Greene, N.D.E., and Murdoch, J.N. (2003). The genetic basis of mammalian neurulation. Nat. Rev. Genet. Lond. *4*, 784–793.

Copp, A.J., Stanier, P., and Greene, N.D.E. (2013). Neural tube defects: recent advances, unsolved questions, and controversies. Lancet Neurol. *12*, 799–810.

Cosgrove, D., Meehan, D.T., Grunkemeyer, J.A., Kornak, J.M., Sayers, R., Hunter, W.J., and Samuelson, G.C. (1996). Collagen COL4A3 knockout: a mouse model for autosomal Alport syndrome. Genes Dev. *10*, 2981–2992.

Dady, A., Havis, E., Escriou, V., Catala, M., and Duband, J.-L. (2014). Junctional Neurulation: A Unique Developmental Program Shaping a Discrete Region of the Spinal Cord Highly Susceptible to Neural Tube Defects. J. Neurosci. *34*, 13208–13221.

Davidson, L.A., Marsden, M., Keller, R., and DeSimone, D.W. (2006). Integrin α5β1 and Fibronectin Regulate Polarized Cell Protrusions Required for Xenopus Convergence and Extension. Curr. Biol. *16*, 833–844.

Di Pietro, E., Sirois, J., Tremblay, M.L., and MacKenzie, R.E. (2002). Mitochondrial NAD-dependent methylenetetrahydrofolate dehydrogenase-methenyltetrahydrofolate cyclohydrolase is essential for embryonic development. Mol. Cell. Biol. *22*, 4158–4166.

Di Pietro, E., Wang, X.-L., and MacKenzie, R.E. (2004). The expression of mitochondrial methylenetetrahydrofolate dehydrogenase-cyclohydrolase supports a role in rapid cell growth. Biochim. Biophys. Acta *1674*, 78–84.

Donato, H., Krupenko, N.I., Tsybovsky, Y., and Krupenko, S.A. (2007). 10-Formyltetrahydrofolate Dehydrogenase Requires a 4′-Phosphopantetheine Prosthetic Group for Catalysis. J. Biol. Chem. *282*, 34159–34166.

Dorokhov, Y.L., Shindyapina, A.V., Sheshukova, E.V., and Komarova, T.V. (2015). Metabolic methanol: molecular pathways and physiological roles. Physiol. Rev. *95*, 603–644.

Ducker, G.S., Chen, L., Morscher, R.J., Ghergurovich, J.M., Esposito, M., Teng, X., Kang, Y., and Rabinowitz, J.D. (2016). Reversal of Cytosolic One-Carbon Flux Compensates for Loss of the Mitochondrial Folate Pathway. Cell Metab. *23*, 1140–1153.

Dunlevy, L.P.E., Burren, K.A., Mills, K., Chitty, L.S., Copp, A.J., and Greene, N.D.E. (2006a). Integrity of the methylation cycle is essential for mammalian neural tube closure. Birt. Defects Res. A. Clin. Mol. Teratol. *76*, 544–552.

Dunlevy, L.P.E., Burren, K.A., Chitty, L.S., Copp, A.J., and Greene, N.D.E. (2006b). Excess methionine suppresses the methylation cycle and inhibits neural tube closure in mouse embryos. FEBS Lett. *580*, 2803–2807.

Eberlin, L.S., Ferreira, C.R., Dill, A.L., Ifa, D.R., Cheng, L., and Cooks, R.G. (2011). Nondestructive, Histologically Compatible Tissue Imaging by Desorption Electrospray Ionization Mass Spectrometry. ChemBioChem *12*, 2129–2132.

Eberlin, L.S., Gabay, M., Fan, A.C., Gouw, A.M., Tibshirani, R.J., Felsher, D.W., and Zare, R.N. (2014). Alteration of the lipid profile in lymphomas induced by MYC overexpression. Proc. Natl. Acad. Sci. *111*, 10450–10455.

Eichholzer, M., Tönz, O., and Zimmermann, R. (2006). Folic acid: a public-health challenge. The Lancet *367*, 1352–1361.

El-Hadidy, M.A., Abdeen, H.M., Abd El-Aziz, S.M., and Al-Harrass, M. (2014). MTHFR Gene Polymorphism and Age of Onset of Schizophrenia and Bipolar Disorder.

Finkelstein, J.D. (1990). Methionine metabolism in mammals. J. Nutr. Biochem. *1*, 228–237.

Fleming, A., Gerrelli, D., Greene, N.D., and Copp, A.J. (1997). Mechanisms of normal and abnormal neurulation: evidence from embryo culture studies. Int. J. Dev. Biol. *41*, 199–212.

Fox, J.T., and Stover, P.J. (2008). Chapter 1 Folate-Mediated One-Carbon Metabolism. In Vitamins & Hormones, (Academic Press), pp. 1–44.

Franceschini, N., Carty, C., Bůžková, P., Reiner, A., Garrett, T., Lin, Y., Vöckler, J.-S., Hindorff, L.A., Cole, S.A., Boerwinkle, E., et al. (2011). Association of Genetic Variants and Incident Coronary Heart Disease in Multi-Ethnic Cohorts. The PAGE Study. Circ. Cardiovasc. Genet. *4*, 661–672.

Franke, W.W., Grund, C., Kuhn, C., Jackson, B.W., and Illmensee, K. (1982). Formation of cytoskeletal elements during mouse embryogenesis. III. Primary mesenchymal cells and the first appearance of vimentin filaments. Differ. Res. Biol. Divers. *23*, 43–59.

Ganguly, P., and Alam, S.F. (2015). Role of homocysteine in the development of cardiovascular disease. Nutr. J. *14*.

García-Martínez, L.F., and Appling, D.R. (1993). Characterization of the folate-dependent mitochondrial oxidation of carbon 3 of serine. Biochemistry *32*, 4671–4676.

Gattazzo, F., Urciuolo, A., and Bonaldo, P. (2014). Extracellular matrix: a dynamic microenvironment for stem cell niche. Biochim. Biophys. Acta *1840*, 2506–2519.

George, E.L., Georges-Labouesse, E.N., Patel-King, R.S., Rayburn, H., and Hynes, R.O. (1993). Defects in mesoderm, neural tube and vascular development in mouse embryos lacking fibronectin. Development *119*, 1079–1091.

Georges-Labouesse, E.N., George, E.L., Rayburn, H., and Hynes, R.O. (1996). Mesodermal development in mouse embryos mutant for fibronectin. Dev. Dyn. *207*, 145–156.

Guillon, J.M., Mechulam, Y., Schmitter, J.M., Blanquet, S., and Fayat, G. (1992). Disruption of the gene for Met-tRNA(fMet) formyltransferase severely impairs growth of Escherichia coli. J. Bacteriol. *174*, 4294–4301.

Haeckel, E. (1874). Jenaische Zeitschrift für Naturwissenschaft. (Jena,: Gustav Fischer [etc.].).

Halbreich, A., and Rabinowitz, M. (1971). Isolation of Saccharomyces cerevisiae mitochondrial formyltetrahydrofolic acid:methionyl-tRNA transformylase and the hybridization of mitochondrial fMet-tRNA with mitochondrial DNA. Proc. Natl. Acad. Sci. U. S. A. *68*, 294–298.

Hall, P.A., and Watt, F.M. (1989). Stem cells: the generation and maintenance of cellular diversity. Development *106*, 619–633.

Hansler, A., Chen, Q., Gray, J.D., Ross, M.E., Finnell, R.H., and Gross, S.S. (2014). Untargeted metabolite profiling of murine embryos to reveal metabolic perturbations associated with neural tube closure defects. Birt. Defects Res. A. Clin. Mol. Teratol. *100*, 623–632.

Hasegawa, T., Mikoda, N., Kitazawa, M., and LaFerla, F.M. (2010). Treatment of Alzheimer's disease with anti-homocysteic acid antibody in 3xTg-AD male mice. PloS One *5*, e8593.

Herbig, K., Chiang, E.-P., Lee, L.-R., Hills, J., Shane, B., and Stover, P.J. (2002). Cytoplasmic serine hydroxymethyltransferase mediates competition between folate-dependent deoxyribonucleotide and S-adenosylmethionine biosyntheses. J. Biol. Chem. *277*, 38381–38389.

Hertwig, O., and Hertwig, R. (1881). Die Coelomtheorie; Versuch einer Erklärung des mittleren Keimblattes (Fischer).

Hibbard, B.M. (1964). The Role of Folic Acid in Pregnancy*. BJOG Int. J. Obstet. Gynaecol. *71*, 529–542.

Hibbard, ElizabethD., and Smithells, R.W. (1965). FOLIC ACID METABOLISM AND HUMAN EMBRYOPATHY. The Lancet *285*, 1254.

Horne, D.W., Patterson, D., and Cook, R.J. (1989). Effect of nitrous oxide inactivation of vitamin B12-dependent methionine synthetase on the subcellular distribution of folate coenzymes in rat liver. Arch. Biochem. Biophys. *270*, 729–733.

Horswill, M.A., Narayan, M., Warejcka, D.J., Cirillo, L.A., and Twining, S.S. (2008). Epigenetic silencing of maspin expression occurs early in the conversion of keratocytes to fibroblasts. Exp. Eye Res. *86*, 586–600.

Hubacek, J., Stanek, V., Poledne, R., Adamkova, V., and Pitha, J. (2016). Rs6922269 marker at the MTHFD1L gene predict cardiovascular mortality in males after acute coronary syndrome. Atherosclerosis *252*, e77–e78.

Hughes, E.R., Winter, M.G., Duerkop, B.A., Spiga, L., Furtado de Carvalho, T., Zhu, W., Gillis, C.C., Büttner, L., Smoot, M.P., Behrendt, C.L., et al. (2017). Microbial Respiration and Formate Oxidation as Metabolic Signatures of Inflammation-Associated Dysbiosis. Cell Host Microbe *21*, 208–219.

Hunter, E.S., and Tugman, J.A. (1995). Inhibitors of glycolytic metabolism affect neurulation-staged mouse conceptuses in vitro. Teratology *52*, 317–323.

Jain, M., Nilsson, R., Sharma, S., Madhusudhan, N., Kitami, T., Souza, A.L., Kafri, R., Kirschner, M.W., Clish, C.B., and Mootha, V.K. (2012). Metabolite Profiling Identifies a Key Role for Glycine in Rapid Cancer Cell Proliferation. Science *336*, 1040–1044.

Jiang, X., Iseki, S., Maxson, R.E., Sucov, H.M., and Morriss-Kay, G.M. (2002). Tissue origins and interactions in the mammalian skull vault. Dev. Biol. *241*, 106–116.

Juriloff, D.M., and Harris, M.J. (2018). Insights into the Etiology of Mammalian Neural Tube Closure Defects from Developmental, Genetic and Evolutionary Studies. J. Dev. Biol. *6*.

Kim, D.W., Huang, T., Schirch, D., and Schirch, V. (1996). Properties of Tetrahydropteroylpentaglutamate Bound to 10-Formyltetrahydrofolate Dehydrogenase. Biochemistry *35*, 15772–15783.

Kim, J., Lei, Y., Guo, J., Kim, S.-E., Wlodarczyk, B.J., Cabrera, R.M., Lin, Y.L., Nilsson, T.K., Zhang, T., Ren, A., et al. (2018). Formate rescues neural tube defects caused by mutations in Slc25a32. Proc. Natl. Acad. Sci. *115*, 4690–4695.

Knudson, C.B. (2003). Hyaluronan and CD44: Strategic players for cell–matrix interactions during chondrogenesis and matrix assembly. Birth Defects Res. Part C Embryo Today Rev. *69*, 174–196.

Kobayakawa, S., Miike, K., Nakao, M., and Abe, K. (2007). Dynamic changes in the epigenomic state and nuclear organization of differentiating mouse embryonic stem cells. Genes Cells *12*, 447–460.

Kory, N., Wyant, G.A., Prakash, G., Uit de Bos, J., Bottanelli, F., Pacold, M.E., Chan, S.H., Lewis, C.A., Wang, T., Keys, H.R., et al. (2018). SFXN1 is a mitochondrial serine transporter required for one-carbon metabolism. Science *362*.

Kozak, M. (1983). Comparison of initiation of protein synthesis in procaryotes, eucaryotes, and organelles. Microbiol. Mol. Biol. Rev. *47*, 1–45.

Krupenko, S.A. (2009). FDH: an Aldehyde Dehydrogenase Fusion Enzyme in Folate Metabolism. Chem. Biol. Interact. *178*, 84–93.

Krupenko, S.A., and Oleinik, N.V. (2002). 10-formyltetrahydrofolate dehydrogenase, one of the major folate enzymes, is down-regulated in tumor tissues and possesses suppressor effects on cancer cells. Cell Growth Differ. Mol. Biol. J. Am. Assoc. Cancer Res. *13*, 227–236.

Krupenko, N.I., Dubard, M.E., Strickland, K.C., Moxley, K.M., Oleinik, N.V., and Krupenko, S.A. (2010). ALDH1L2 Is the Mitochondrial Homolog of 10-Formyltetrahydrofolate Dehydrogenase. J. Biol. Chem. *285*, 23056–23063.

Krupenko, S.A., Wagner, C., and Cook, R.J. (1995). Recombinant 10-formyltetrahydrofolate dehydrogenase catalyses both dehydrogenase and hydrolase reactions utilizing the synthetic substrate 10-formyl-5,8-dideazafolate. Biochem. J. *306*, 651–655.

Lakhwani, S., García-Sanz, P., and Vallejo, M. (2010). Alx3-deficient mice exhibit folic acid-resistant craniofacial midline and neural tube closure defects. Dev. Biol. *344*, 869–880.

Le A. Trinh, and Stainier, D.Y.R. (2004). Fibronectin Regulates Epithelial Organization during Myocardial Migration in Zebrafish. Dev. Cell *6*, 371–382.

Lee, D., Xu, I.M.-J., Chiu, D.K.-C., Lai, R.K.-H., Tse, A.P.-W., Lan Li, L., Law, C.-T., Tsang, F.H.-C., Wei, L.L., Chan, C.Y.-K., et al. (2017). Folate cycle enzyme MTHFD1L confers metabolic advantages in hepatocellular carcinoma. J. Clin. Invest. *127*, 1856–1872.

Lee, G.Y., Haverty, P.M., Li, L., Kljavin, N.M., Bourgon, R., Lee, J., Stern, H., Modrusan, Z., Seshagiri, S., Zhang, Z., et al. (2014). Comparative Oncogenomics Identifies PSMB4 and SHMT2 as Potential Cancer Driver Genes. Cancer Res.

Li, Y., Holmes, W.B., Appling, D.R., and RajBhandary, U.L. (2000). Initiation of Protein Synthesis in Saccharomyces cerevisiae Mitochondria without Formylation of the Initiator tRNA. J. Bacteriol. *182*, 2886–2892.

Liew, S.-C., and Gupta, E.D. (2015). Methylenetetrahydrofolate reductase (MTHFR) C677T polymorphism: epidemiology, metabolism and the associated diseases. Eur. J. Med. Genet. *58*, 1–10.

Lin, B.F., Huang, R.F., and Shane, B. (1993). Regulation of folate and one-carbon metabolism in mammalian cells. III. Role of mitochondrial folylpoly-gamma-glutamate synthetase. J. Biol. Chem. *268*, 21674–21679.

Lin, S., Ren, A., Wang, L., Santos, C., Huang, Y., Jin, L., Li, Z., and Greene, N.D.E. (2019). Aberrant methylation of Pax3 gene and neural tube defects in association with exposure to polycyclic aromatic hydrocarbons. Clin. Epigenetics Lond. *11*.

Linask, K.K., and Lash, J.W. (1988a). A role for fibronectin in the migration of avian precardiac cells: I. Dose-dependent effects of fibronectin antibody. Dev. Biol. *129*, 315–323.

Linask, K.K., and Lash, J.W. (1988b). A role for fibronectin in the migration of avian precardiac cells: II. Rotation of the heart-forming region during different stages and its effects. Dev. Biol. *129*, 324–329.

Lisi, A., Briganti, E., Ledda, M., Losi, P., Grimaldi, S., Marchese, R., and Soldani, G. (2012). A Combined Synthetic-Fibrin Scaffold Supports Growth and Cardiomyogenic Commitment of Human Placental Derived Stem Cells. PLOS ONE *7*, e34284.

Liu, X., Wu, H., Byrne, M., Jeffrey, J., Krane, S., and Jaenisch, R. (1995). A targeted mutation at the known collagenase cleavage site in mouse type I collagen impairs tissue remodeling. J. Cell Biol. *130*, 227–237.

Löhler, J., Timpl, R., and Jaenisch, R. (1984). Embryonic lethal mutation in mouse collagen I gene causes rupture of blood vessels and is associated with erythropoietic and mesenchymal cell death. Cell *38*, 597–607.

Ma, X.-Y., Yu, J.-T., Wu, Z.-C., Zhang, Q., Liu, Q.-Y., Wang, H.-F., Wang, W., and Tan, L. (2012). Replication of the MTHFD1L gene association with late-onset Alzheimer's disease in a Northern Han Chinese population. J. Alzheimers Dis. JAD *29*, 521–525.

MacFarlane, A.J., Liu, X., Perry, C.A., Flodby, P., Allen, R.H., Stabler, S.P., and Stover, P.J. (2008). Cytoplasmic serine hydroxymethyltransferase regulates the metabolic partitioning of methylenetetrahydrofolate but is not essential in mice. J. Biol. Chem. *283*, 25846–25853.

MacFarlane, A.J., Perry, C.A., Girnary, H.H., Gao, D., Allen, R.H., Stabler, S.P., Shane, B., and Stover, P.J. (2009). Mthfd1 Is an Essential Gene in Mice and Alters Biomarkers of Impaired One-carbon Metabolism. J. Biol. Chem. *284*, 1533–1539.

MacFarlane, A.J., Anderson, D.D., Flodby, P., Perry, C.A., Allen, R.H., Stabler, S.P., and Stover, P.J. (2011). Nuclear localization of de novo thymidylate biosynthesis pathway is required to prevent uracil accumulation in DNA. J. Biol. Chem. *286*, 44015–44022.

McBurney, M.W., and Whitmore, G.F. (1974). Isolation and biochemical characterization of folate deficient mutants of chinese hamster cells. Cell *2*, 173–182.

McShane, S.G., Molè, M.A., Savery, D., Greene, N.D.E., Tam, P.P.L., and Copp, A.J. (2015). Cellular basis of neuroepithelial bending during mouse spinal neural tube closure. Dev. Biol. *404*, 113–124.

Meinnel, T., Guillon, J.M., Mechulam, Y., and Blanquet, S. (1993). The Escherichia coli fmt gene, encoding methionyl-tRNA(fMet) formyltransferase, escapes metabolic control. J. Bacteriol. *175*, 993–1000.

Meiser, J., Tumanov, S., Maddocks, O., Labuschagne, C.F., Athineos, D., Broek, N.V.D., Mackay, G.M., Gottlieb, E., Blyth, K., Vousden, K., et al. (2016). Serine one-carbon catabolism with formate overflow. Sci. Adv. *2*, e1601273.

Mejia, N.R., and MacKenzie, R.E. (1985). NAD-dependent methylenetetrahydrofolate dehydrogenase is expressed by immortal cells. J. Biol. Chem. *260*, 14616–14620.

Min, H., Shane, B., and Stokstad, E.L. (1988). Identification of 10-formyltetrahydrofolate dehydrogenase-hydrolase as a major folate binding protein in liver cytosol. Biochim. Biophys. Acta *967*, 348–353.

Miner, J.H., and Sanes, J.R. (1996). Molecular and functional defects in kidneys of mice lacking collagen alpha 3(IV): implications for Alport syndrome. J. Cell Biol. *135*, 1403–1413.

Miner, J.H., Cunningham, J., and Sanes, J.R. (1998). Roles for Laminin in Embryogenesis: Exencephaly, Syndactyly, and Placentopathy in Mice Lacking the Laminin α5 Chain. J. Cell Biol. *143*, 1713–1723.

Minguzzi, S., Selcuklu, S.D., Spillane, C., and Parle-McDermott, A. (2014). An NTD-associated polymorphism in the 3' UTR of MTHFD1L can affect disease risk by altering miRNA binding. Hum. Mutat. *35*, 96–104.

Mitchell, H.K., Snell, E.E., and Williams, R.J. (1941). The concentration of "folic acid." J. Am. Chem. Soc. *63*, 324–325.

Miyazawa, H., Yamaguchi, Y., Sugiura, Y., Honda, K., Kondo, K., Matsuda, F., Yamamoto, T., Suematsu, M., and Miura, M. (2017). Rewiring of embryonic glucose metabolism via suppression of PFK-1 and aldolase during mouse chorioallantoic branching. Dev. Camb. Engl. *144*, 63–73.

Moephuli, S.R., Klein, N.W., Baldwin, M.T., and Krider, H.M. (1997). Effects of methionine on the cytoplasmic distribution of actin and tubulin during neural tube closure in rat embryos. Proc. Natl. Acad. Sci. U. S. A. *94*, 543–548.

Momb, J., Lewandowski, J.P., Bryant, J.D., Fitch, R., Surman, D.R., Vokes, S.A., and Appling, D.R. (2013). Deletion of Mthfd1l causes embryonic lethality and neural tube and craniofacial defects in mice. Proc. Natl. Acad. Sci. U. S. A. *110*, 549–554.

Morgan, T.M., House, J.A., Cresci, S., Jones, P., Allayee, H., Hazen, S.L., Patel, Y., Patel, R.S., Eapen, D.J., Waddy, S.P., et al. (2011). Investigation of 95 variants identified in a genome-wide study for association with mortality after acute coronary syndrome. BMC Med. Genet. *12*, 127.

Morriss, G.M., and Solursh, M. (1978). Regional differences in mesenchymal cell morphology and glycosaminoglycans in early neural-fold stage rat embryos. J. Embryol. Exp. Morphol. *46*, 37–52.

Morriss-Kay, G.M. (1981). Growth and development of pattern in the cranial neural epithelium of rat embryos during neurulation. J. Embryol. Exp. Morphol. *65 Suppl*, 225–241.

Morriss-Kay, G.M., Tuckett, F., and Solursh, M. (1986). The effects of Streptomyces hyaluronidase on tissue organization and cell cycle time in rat embryos. J. Embryol. Exp. Morphol. *98*, 59–70.

Morris-Wiman, J., and Brinkley, L.L. (1990a). Changes in mesenchymal cell and hyaluronate distribution correlate with in vivo elevation of the mouse mesencephalic neural folds. Anat. Rec. *226*, 383–395.

Morris-Wiman, J., and Brinkley, L.L. (1990b). The role of the mesenchyme in mouse neural fold elevation. I. Patterns of mesenchymal cell distribution and proliferation in embryos developing in vitro. Am. J. Anat. *188*, 121–132.

Morrow, G.P., MacMillan, L., Lamarre, S.G., Young, S.K., MacFarlane, A.J., Brosnan, M.E., and Brosnan, J.T. (2015). In Vivo Kinetics of Formate Metabolism in Folate-deficient and Folate-replete Rats. J. Biol. Chem. *290*, 2244–2250.

Mosley, B.S., Cleves, M.A., Siega-Riz, A.M., Shaw, G.M., Canfield, M.A., Waller, D.K., Werler, M.M., and Hobbs, C.A. (2009). Neural Tube Defects and Maternal Folate Intake Among Pregnancies Conceived After Folic Acid Fortification in the United States. Am. J. Epidemiol. *169*, 9–17.

Motokawa, Y., and Kikuchi, G. (1971). Glycine metabolism in rat liver mitochondria. V. Intramitochondrial localization of the reversible glycine cleavage system and serine hydroxymethyltransferase. Arch. Biochem. Biophys. *146*, 461–464.

Mudd, S.H., Finkelstein, J.D., Irreverre, F., and Laster, L. (1965). Transsulfuration in mammals. Microassays and tissue distributions of three enzymes of the pathway. J. Biol. Chem. *240*, 4382–4392.

Mudd, S.H., Brosnan, J.T., Brosnan, M.E., Jacobs, R.L., Stabler, S.P., Allen, R.H., Vance, D.E., and Wagner, C. (2007). Methyl balance and transmethylation fluxes in humans. Am. J. Clin. Nutr. *85*, 19–25.

Naj, A.C., Beecham, G.W., Martin, E.R., Gallins, P.J., Powell, E.H., Konidari, I., Whitehead, P.L., Cai, G., Haroutunian, V., Scott, W.K., et al. (2010). Dementia Revealed: Novel Chromosome 6 Locus for Late-Onset Alzheimer Disease Provides Genetic Evidence for Folate-Pathway Abnormalities. PLoS Genet. *6*.

Narisawa, A., Komatsuzaki, S., Kikuchi, A., Niihori, T., Aoki, Y., Fujiwara, K., Tanemura, M., Hata, A., Suzuki, Y., Relton, C.L., et al. (2012). Mutations in genes encoding the glycine cleavage system predispose to neural tube defects in mice and humans. Hum. Mol. Genet. *21*, 1496–1503.

Nehra, D., Le, H.D., Fallon, E.M., Carlson, S.J., Woods, D., White, Y.A., Pan, A.H., Guo, L., Rodig, S.J., Tilly, J.L., et al. (2012). Prolonging the female reproductive lifespan and improving egg quality with dietary omega-3 fatty acids. Aging Cell *11*, 1046–1054.

Newton, D.T., Creuzenet, C., and Mangroo, D. (1999). Formylation is not essential for initiation of protein synthesis in all eubacteria. J. Biol. Chem. *274*, 22143–22146.

Neymeyer, V.R., and Tephly, T.R. (1994). Detection and quantification of 10-formyltetrahydrofolate dehydrogenase (10-FTHFDH) in rat retina, optic nerve, and brain. Life Sci. *54*, PL395–PL399.

Nilsson, R., Jain, M., Madhusudhan, N., Sheppard, N.G., Strittmatter, L., Kampf, C., Huang, J., Asplund, A., and Mootha, V.K. (2014). Metabolic enzyme expression highlights a key role for MTHFD2 and the mitochondrial folate pathway in cancer. Nat. Commun. *5*, 3128.

Nilsson, S.K., Haylock, D.N., Johnston, H.M., Occhiodoro, T., Brown, T.J., and Simmons, P.J. (2003). Hyaluronan is synthesized by primitive hemopoietic cells, participates in their lodgment at the endosteum following transplantation, and is involved in the regulation of their proliferation and differentiation in vitro. Blood *101*, 856–862.

Noden, D.M., and Trainor, P.A. (2005). Relations and interactions between cranial mesoderm and neural crest populations. J. Anat. *207*, 575–601.

Osborn, M.J., Hatefi, Y., Kay, L.D., and Huennekens, F.M. (1957). Evidence for the enzymic deacylation of N10-formyl tetrahydro-folic acid. Biochim. Biophys. Acta *26*, 208–210.

Pai, Y.J., Leung, K.-Y., Savery, D., Hutchin, T., Prunty, H., Heales, S., Brosnan, M.E., Brosnan, J.T., Copp, A.J., and Greene, N.D.E. (2015). Glycine decarboxylase deficiency causes neural tube defects and features of non-ketotic hyperglycinemia in mice. Nat. Commun. *6*, 6388.

Palmer, B.R., Slow, S., Ellis, K.L., Pilbrow, A.P., Skelton, L., Frampton, C.M., Palmer, S.C., Troughton, R.W., Yandle, T.G., Doughty, R.N., et al. (2014). Genetic Polymorphism rs6922269 in the MTHFD1L Gene Is Associated with Survival and Baseline Active Vitamin B12 Levels in Post-Acute Coronary Syndromes Patients. PLoS ONE *9*.

Parle-McDermott, A., Pangilinan, F., O'Brien, K.K., Mills, J.L., Magee, A.M., Troendle, J., Sutton, M., Scott, J.M., Kirke, P.N., Molloy, A.M., et al. (2009). A common variant in MTHFD1L is associated with neural tube defects and mRNA splicing efficiency. Hum. Mutat. *30*, 1650–1656.

Pasternack, L.B., Laude, D.A., and Appling, D.R. (1994). Whole-cell detection by 13C NMR of metabolic flux through the C1-tetrahydrofolate synthase/serine hydroxymethyltransferase enzyme system and effect of antifolate exposure in Saccharomyces cerevisiae. Biochemistry *33*, 7166–7173.

Peck, D., and Isacke, C.M. (1996). CD44 phosphorylation regulates melanoma cell and fibroblast migration on, but not attachment to, a hyaluronan substratum. Curr. Biol. *6*, 884–890.

Peters, G.J., Backus, H.H.J., Freemantle, S., van Triest, B., Codacci-Pisanelli, G., van der Wilt, C.L., Smid, K., Lunec, J., Calvert, A.H., Marsh, S., et al. (2002). Induction of thymidylate synthase as a 5-fluorouracil resistance mechanism. Biochim. Biophys. Acta *1587*, 194–205.

Pike, S.T., Rajendra, R., Artzt, K., and Appling, D.R. (2010). Mitochondrial C1-tetrahydrofolate synthase (MTHFD1L) supports the flow of mitochondrial one-carbon units into the methyl cycle in embryos. J. Biol. Chem. *285*, 4612–4620.

Poddar, R., and Paul, S. (2009). Homocysteine-NMDA receptor-mediated activation of extracellular signal-regulated kinase leads to neuronal cell death. J. Neurochem. *110*, 1095–1106.

Pöschl, E., Schlötzer-Schrehardt, U., Brachvogel, B., Saito, K., Ninomiya, Y., and Mayer, U. (2004). Collagen IV is essential for basement membrane stability but

dispensable for initiation of its assembly during early development. Development *131*, 1619–1628.

Prasannan, P., and Appling, D.R. (2009). Human mitochondrial C1-tetrahydrofolate synthase: submitochondrial localization of the full-length enzyme and characterization of a short isoform. Arch. Biochem. Biophys. *481*, 86–93.

Prasannan, P., Pike, S., Peng, K., Shane, B., and Appling, D.R. (2003). Human mitochondrial C1-tetrahydrofolate synthase: gene structure, tissue distribution of the mRNA, and immunolocalization in Chinese hamster ovary calls. J. Biol. Chem. *278*, 43178–43187.

Radziejewska, A., and Chmurzynska, A. (2019). Folate and choline absorption and uptake: Their role in fetal development. Biochimie *158*, 10–19.

Rai, V. (2016). Association of methylenetetrahydrofolate reductase (MTHFR) gene C677T polymorphism with autism: evidence of genetic susceptibility. Metab. Brain Dis. *31*, 727–735.

Reid, B.S., Sargent, T.D., and Williams, T. (2010). Generation and characterization of a novel neural crest marker allele, Inka1-LacZ, reveals a role for Inka1 in mouse neural tube closure. Dev. Dyn. Off. Publ. Am. Assoc. Anat. *239*, 1188–1196.

Ren, R.-J., Wang, L.-L., Fang, R., Liu, L.-H., Wang, Y., Tang, H.-D., Deng, Y.-L., Xu, W., Wang, G., and Chen, S.-D. (2011). The MTHFD1L gene rs11754661 marker is associated with susceptibility to Alzheimer's disease in the Chinese Han population. J. Neurol. Sci. *308*, 32–34.

Rheault, M.N., Kren, S.M., Thielen, B.K., Mesa, H.A., Crosson, J.T., Thomas, W., Sado, Y., Kashtan, C.E., and Segal, Y. (2004). Mouse Model of X-Linked Alport Syndrome. J. Am. Soc. Nephrol. *15*, 1466–1474.

Rios-Orlandi, E.M., Zarkadas, C.G., and MacKenzie, R.E. (1986). Formyltetrahydrofolate dehydrogenase-hydrolase from pig liver: simultaneous assay of the activities. Biochim. Biophys. Acta *871*, 24–35.

Román, G.C. (2015). MTHFR Gene Mutations: A Potential Marker of Late-Onset Alzheimer's Disease? J. Alzheimers Dis. JAD *47*, 323–327.

Rozario, T., and DeSimone, D.W. (2010). The Extracellular Matrix In Development and Morphogenesis: A Dynamic View. Dev. Biol. *341*, 126–140.

Saade, S., Cazier, J.-B., Ghassibe-Sabbagh, M., Youhanna, S., Badro, D.A., Kamatani, Y., Hager, J., Yeretzian, J.S., El-Khazen, G., Haber, M., et al. (2011). Large scale

association analysis identifies three susceptibility loci for coronary artery disease. PloS One *6*, e29427.

Samani, N.J., Erdmann, J., Hall, A.S., Hengstenberg, C., Mangino, M., Mayer, B., Dixon, R.J., Meitinger, T., Braund, P., Wichmann, H.-E., et al. (2007). Genomewide Association Analysis of Coronary Artery Disease. N. Engl. J. Med. *357*, 443–453.

Santi, D.V., and Hardy, L.W. (1987). Catalytic mechanism and inhibition of tRNA (uracil-5-)methyltransferase: evidence for covalent catalysis. Biochemistry *26*, 8599–8606.

Schnieke, A., Harbers, K., and Jaenisch, R. (1983). Embryonic lethal mutation in mice induced by retrovirus insertion into the α 1(I) collagen gene. Nature *304*, 315.

Scrutton, M.C., and Beis, I. (1979). Inhibitory effects of histidine and their reversal. The roles of pyruvate carboxylase and N10-formyltetrahydrofolate dehydrogenase. Biochem. J. *177*, 833–846.

Selcuklu, S.D., Donoghue, M.T.A., Rehmet, K., Gomes, M. de S., Fort, A., Kovvuru, P., Muniyappa, M.K., Kerin, M.J., Enright, A.J., and Spillane, C. (2012). MicroRNA-9 Inhibition of Cell Proliferation and Identification of Novel miR-9 Targets by Transcriptome Profiling in Breast Cancer Cells. J. Biol. Chem. *287*, 29516–29528.

Sener, E.F., Oztop, D.B., and Ozkul, Y. (2014). MTHFR Gene C677T Polymorphism in Autism Spectrum Disorders. Genet. Res. Int. *2014*, 698574.

Shane, B. (1989). Folylpolyglutamate synthesis and role in the regulation of one-carbon metabolism. Vitam. Horm. *45*, 263–335.

Shen, D., Dalton, T.P., Nebert, D.W., and Shertzer, H.G. (2005). Glutathione redox state regulates mitochondrial reactive oxygen production. J. Biol. Chem. *280*, 25305–25312.

Shin, M. (2016). Characterization of the role of the mitochondrial one-carbon metabolism during embryonic development. Thesis.

Shin, M., Bryant, J.D., Momb, J., and Appling, D.R. (2014). Mitochondrial MTHFD2L Is a Dual Redox Cofactor-specific Methylenetetrahydrofolate Dehydrogenase/Methenyltetrahydrofolate Cyclohydrolase Expressed in Both Adult and Embryonic Tissues. J. Biol. Chem. *289*, 15507–15517.

Shin, M., Momb, J., and Appling, D.R. (2017). Human mitochondrial MTHFD2 is a dual redox cofactor-specific methylenetetrahydrofolate dehydrogenase/methenyltetrahydrofolate cyclohydrolase. Cancer Metab. *5*.

Smith, J.L., and Schoenwolf, G.C. (1997). Neurulation: coming to closure. Trends Neurosci. *20*, 510–517.

Spencer, A.C., and Spremulli, L.L. (2004). Interaction of mitochondrial initiation factor 2 with mitochondrial fMet-tRNA. Nucleic Acids Res. *32*, 5464–5470.

Stead, L.M., Brosnan, J.T., Brosnan, M.E., Vance, D.E., and Jacobs, R.L. (2006). Is it time to reevaluate methyl balance in humans? Am. J. Clin. Nutr. *83*, 5–10.

van Straaten, H.W., Hekking, J.W., Consten, C., and Copp, A.J. (1993). Intrinsic and extrinsic factors in the mechanism of neurulation: effect of curvature of the body axis on closure of the posterior neuropore. Dev. Camb. Engl. *117*, 1163–1172.

Stratman, J.L., Barnes, W.M., and Simon, T.C. (2003). Universal PCR genotyping assay that achieves single copy sensitivity with any primer pair. Transgenic Res. *12*, 521–522.

Strickland, K.C., Krupenko, N.I., Dubard, M.E., Hu, C.J., Tsybovsky, Y., and Krupenko, S.A. (2011a). Enzymatic properties of ALDH1L2, a mitochondrial 10-formyltetrahydrofolate dehydrogenase. Chem. Biol. Interact. *191*, 129–136.

Strickland, K.C., Holmes, R.S., Oleinik, N.V., Krupenko, N.I., and Krupenko, S.A. (2011b). Phylogeny and evolution of aldehyde dehydrogenase-homologous folate enzymes. Chem. Biol. Interact. *191*, 122–128.

Strong, W.B., and Schirch, V. (1989). In vitro conversion of formate to serine: effect of tetrahydropteroylpolyglutamates and serine hydroxymethyltransferase on the rate of 10-formyltetrahydrofolate synthetase. Biochemistry *28*, 9430–9439.

Su, X., Wellen, K.E., and Rabinowitz, J.D. (2016). Metabolic control of methylation and acetylation. Curr. Opin. Chem. Biol. *30*, 52–60.

Sudiwala, S., De Castro, S.C.P., Leung, K.-Y., Brosnan, J.T., Brosnan, M.E., Mills, K., Copp, A.J., and Greene, N.D.E. (2016). Formate supplementation enhances folate-dependent nucleotide biosynthesis and prevents spina bifida in a mouse model of folic acid-resistant neural tube defects. Biochimie *126*, 63–70.

Sugiura, T., Nagano, Y., Inoue, T., and Hirotani, K. (2004). A novel mitochondrial C1-tetrahydrofolate synthetase is upregulated in human colon adenocarcinoma. Biochem. Biophys. Res. Commun. *315*, 204–211.

Sundberg, J.P., Woolcott, B.L., Cunlifee-Beamer, T., Brown, K.S., and Bronson, R. Spontaneous Hydrocephalus in Inbred Strains of Mice.

Tada, M., and Heisenberg, C.-P. (2012). Convergent extension: using collective cell migration and cell intercalation to shape embryos. Development *139*, 3897–3904.

Tanaka, Y., Naruse, I., Hongo, T., Xu, M.-J., Nakahata, T., Maekawa, T., and Ishii, S. (2000). Extensive brain hemorrhage and embryonic lethality in a mouse null mutant of CREB-binding protein. Mech. Dev. *95*, 133–145.

Tang, L.S., Santillano, D.R., Wlodarczyk, B.J., Miranda, R.C., and Finnell, R.H. (2005). Role of Folbp1 in the regional regulation of apoptosis and cell proliferation in the developing neural tube and craniofacies. Am. J. Med. Genet. C Semin. Med. Genet. *135C*, 48–58.

Tedeschi, P.M., Markert, E.K., Gounder, M., Lin, H., Dvorzhinski, D., Dolfi, S.C., Chan, L.L.-Y., Qiu, J., DiPaola, R.S., Hirshfield, K.M., et al. (2013). Contribution of serine, folate and glycine metabolism to the ATP, NADPH and purine requirements of cancer cells. Cell Death Dis. *4*, e877.

Tennessen, J.M., Baker, K.D., Lam, G., Evans, J., and Thummel, C.S. (2011). The Drosophila estrogen-related receptor directs a metabolic switch that supports developmental growth. Cell Metab. *13*, 139–148.

Tibbetts, A.S., and Appling, D.R. (2010). Compartmentalization of Mammalian folate-mediated one-carbon metabolism. Annu. Rev. Nutr. *30*, 57–81.

Tibbetts, A.S., Oesterlin, L., Chan, S.Y., Kramer, G., Hardesty, B., and Appling, D.R. (2003). Mammalian mitochondrial initiation factor 2 supports yeast mitochondrial translation without formylated initiator tRNA. J. Biol. Chem. *278*, 31774–31780.

Titus, S.A., and Moran, R.G. (2000). Retrovirally Mediated Complementation of the glyBPhenotype CLONING OF A HUMAN GENE ENCODING THE CARRIER FOR ENTRY OF FOLATES INTO MITOCHONDRIA. J. Biol. Chem. *275*, 36811–36817.

Toole, B.P. (1997). Hyaluronan in morphogenesis. J. Intern. Med. *242*, 35–40.

Touboul, D., and Brunelle, A. (2016). What more can TOF-SIMS bring than other MS imaging methods? Bioanalysis *8*, 367–369.

Tucker, E.J., Hershman, S.G., Köhrer, C., Belcher-Timme, C.A., Patel, J., Goldberger, O.A., Christodoulou, J., Silberstein, J.M., McKenzie, M., Ryan, M.T., et al. (2011). Mutations in MTFMT Underlie a Human Disorder of Formylation Causing Impaired Mitochondrial Translation. Cell Metab. *14*, 428–434.

Turner, M.A., Yang, X., Yin, D., Kuczera, K., Borchardt, R.T., and Howell, P.L. (2000). Structure and function of S-adenosylhomocysteine hydrolase. Cell Biochem. Biophys. *33*, 101–125.

Varshney, U., and RajBhandary, U.L. (1992). Role of methionine and formylation of initiator tRNA in initiation of protein synthesis in Escherichia coli. J. Bacteriol. *174*, 7819–7826.

Walkup, A.S., and Appling, D.R. (2005). Enzymatic characterization of human mitochondrial C1-tetrahydrofolate synthase. Arch. Biochem. Biophys. *442*, 196–205.

Wallingford, J.B., Niswander, L.A., Shaw, G.M., and Finnell, R.H. (2013). The continuing challenge of understanding, preventing, and treating neural tube defects. Science *339*, 1222002.

Wang, Y.-K., and Chen, C.S. (2013). Cell adhesion and mechanical stimulation in the regulation of mesenchymal stem cell differentiation. J. Cell. Mol. Med. *17*, 823–832.

Wang, X., Guan, Z., Chen, Y., Dong, Y., Niu, Y., Wang, J., Zhang, T., and Niu, B. (2015). Genomic DNA Hypomethylation Is Associated with Neural Tube Defects Induced by Methotrexate Inhibition of Folate Metabolism. PLoS One San Franc. *10*, e0121869.

Ward, M. (2001). Homocysteine, folate, and cardiovascular disease. Int. J. Vitam. Nutr. Res. Int. Z. Vitam.- Ernahrungsforschung J. Int. Vitaminol. Nutr. *71*, 173–178.

Warren, M.S., Mattia, K.M., Marolewski, A.E., and Benkovic, S.J. (1996). The transformylase enzymes of de novo purine biosynthesis. Pure Appl. Chem. *68*, 2029–2036.

Watt, F.M., and Huck, W.T.S. (2013). Role of the extracellular matrix in regulating stem cell fate. Nat. Rev. Mol. Cell Biol. Lond. *14*, 467–473.

Webb, A.E., Sanderford, J., Frank, D., Talbot, W.S., Driever, W., and Kimelman, D. (2007). Laminin α5 is essential for the formation of the zebrafish fins. Dev. Biol. *311*, 369–382.

Wittwer, A.J., and Wagner, C. (1980). Identification of folate binding protein of mitochondria as dimethylglycine dehydrogenase. Proc. Natl. Acad. Sci. U. S. A. *77*, 4484–4488.

Woeller, C.F., Anderson, D.D., Szebenyi, D.M.E., and Stover, P.J. (2007). Evidence for Small Ubiquitin-like Modifier-dependent Nuclear Import of the Thymidylate Biosynthesis Pathway. J. Biol. Chem. *282*, 17623–17631.

Wu, G., Bazer, F.W., Datta, S., Johnson, G.A., Li, P., Satterfield, M.C., and Spencer, T.E. (2008). Proline metabolism in the conceptus: implications for fetal growth and development. Amino Acids *35*, 691–702.

Wyngaarden, J.B., and Kelley, W.N. (1983). The Metabolic Basis of Inherited Disease. In The Metabolic Basis of Inherited Disease, (New York: McGraw-Hill), pp. 1043–1114.

Yamaguchi, Y., and Miura, M. (2013). How to form and close the brain: insight into the mechanism of cranial neural tube closure in mammals. Cell. Mol. Life Sci. CMLS *70*, 3171–3186.

Yang, Y., Chen, J., Wang, B., Ding, C., and Liu, H. (2015). Association between MTHFR C677T polymorphism and neural tube defect risks: A comprehensive evaluation in three groups of NTD patients, mothers, and fathers. Birt. Defects Res. A. Clin. Mol. Teratol. *103*, 488–500.

Yoon Soon Shin, Chan, C., Vidal, A.J., Brody, T., and Stokstad, E.L.R. (1976). Subcellular localization of γ-glutamyl carboxypeptidase and of folates. Biochim. Biophys. Acta BBA - Gen. Subj. *444*, 794–801.

Yoshida, T., and Kikuchi, G. (1971). Significance of the glycine cleavage system in glycine and serine catabolism in avian liver. Arch. Biochem. Biophys. *145*, 658–668.

Yoshida, T., Vivatbutsiri, P., Morriss-Kay, G., Saga, Y., and Iseki, S. (2008). Cell lineage in mammalian craniofacial mesenchyme. Mech. Dev. *125*, 797–808.

Zaganjor, I., Sekkarie, A., Tsang, B.L., Williams, J., Razzaghi, H., Mulinare, J., Sniezek, J.E., Cannon, M.J., and Rosenthal, J. (2016). Describing the Prevalence of Neural Tube Defects Worldwide: A Systematic Literature Review. PLOS ONE *11*, e0151586.

Zamierowski, M.M., and Wagner, C. (1977). Identification of folate binding proteins in rat liver. J. Biol. Chem. *252*, 933–938.

Zeisel, S.H., and da Costa, K.-A. (2009). Choline: An Essential Nutrient for Public Health. Nutr. Rev. *67*, 615–623.

Zhao, Q., Behringer, R.R., and de Crombrugghe, B. (1996). Prenatal folic acid treatment suppresses acrania and meroanencephaly in mice mutant for the Cart1 homeobox gene. Nat. Genet. *13*, 275–283.

Zohn, I.E., and Sarkar, A.A. (2012). Does the cranial mesenchyme contribute to neural fold elevation during neurulation? Birt. Defects Res. A. Clin. Mol. Teratol. *94*, 841–848.

(1991). Prevention of neural tube defects: Results of the Medical Research Council Vitamin Study. The Lancet *338*, 131–137.

Vita

Amanda Kristin Vaughn was born in the Washington D.C. area, where she grew up exploring nature and selling her drawings out of a small stand by her childhood home. She and her family moved to Florida in 1996, where she cultivated her love for writing, and attended several conferences for young authors at the University of South Florida while still studying in grade school. She was admitted into the International Baccalaureate (IB) program in Palm Harbor University High School, where she specialized in the fields of Spanish, Biology, and Psychology. During the summers she worked as a veterinary assistant at a nearby beachside animal hospital and a lifeguard at the local YMCA. She went on to study Chemistry at the University of Florida with a minor in German, and spent one semester studying Agricultural Engineering at the Polychemical University of Madrid in Spain. After completing her B.S. in Chemistry, she worked as an art auctioneer for Norwegian Cruise lines, living part time in Bermuda. This job gave her the opportunity to interact with people from all over the world, and this experience compelled her to then move to Taiwan to perfect her Chinese language skills. In Taipei she went to the Center for Mandarin Studies at ShiDa University, and worked part time as an English teacher. Her desire to return to the sciences brought her back to the US, where she studied mouse lung histology at Shands Cancer Center at the University of Florida. These years spent as a lab technican and manager inspired her to pursue her PhD in Biochemistry, which is how she came to live in Austin and work in the Appling lab.

Permanent email: amanda.vaughn@gmail.com

This dissertation was typed by Amanda Vaughn.